A SYSTEMATIC STUDY OF ION-INDUCED NANOPATTERNING ON PHOTONIC CRYSTAL-BASED LABEL-FREE OPTICAL BIOSENSOR

BY

MING KIT CHENG

THESIS

Submitted in partial fulfillment of the requirements
for the degree of Master of Science in Nuclear, Plasma, and Radiological Engineering
in the Graduate College of the
University of Illinois at Urbana-Champaign, 2017

Urbana, Illinois

Master's Committee:

Professor Jean Paul Allain, Advisor
Professor Brian T. Cunningham

ABSTRACT

Photonic crystal (PC)-based biosensors are promising candidates for label-based fluorescence and label-free optical biosensors. This is due to the presence of PC, a periodically-structured dielectric material with diffraction gratings engineered on the surface that can control light propagation through its depth. PC enables resonance of a certain wavelength of light, leading to a significant increase in the intensity of light reflected off the surface, and hence the optical and fluorescent signal output from target analytes. In addition to the use of PC, sensor surfaces can be modified to become more biocompatible and sensitive to changes in target analyte concentrations. It is known that surface topography and chemistry are two main factors affecting protein affinity and conformation on biointerfaces, and the topography and chemistry can be tailored to improve their affinity and adhesion to the surface. It is also known that the presence of nanostructures can increase sensor sensitivity by providing a larger surface area for target adsorption. For example, a sensor surface coated with nanorods has been shown to increase the amount of proteins adsorbed by up to 4x. The tailoring of topography and chemistry can be achieved by the use of ion-beam nanopatterning, in which a beam of energetic ions is incident onto the surface with a tunable energy, incident angle and fluence, in order to disturb the equilibrium of the surface and induce redistribution of surface atoms, and hence changes in surface topography and chemistry. There has already been extensive research in ion-beam nanopatterning in numerous applications, implying its potential in surface modification. However, in these research either a bulk crystal or a thin film with a flat surface is used. When nanopatterning involves thin film with a non-flat surface due to the presence of larger pre-existing structures, such as the diffraction gratings on a PC surface, these pre-existing structures may have a shadowing effect, causing non-uniform sputtering of the surface, and resulting in variations of surface topography on different areas of the pre-existing structures,

as well as affecting the PC's ability to resonate and reflect light due to possible changes in the shape of these structures. Moreover, nanostructures on biosensors are often grown using conventional self-assembled deposition processes such as glancing angle deposition (GLAD), which has a low controllability on the size and shape of structures. To increase the variety of the size, shape and spacing of nanostructures, it is necessary to overcome the thermodynamic constraints by inducing a self-organization process on the surface, which can be initiated by ion-beam nanopatterning. Therefore, to address these two concerns, a systematic study on ion-beam nanopatterning on non-flat surfaces is needed.

A systematic study of ion-beam irradiation on titanium dioxide (TiO_2) thin film of ~ 100 nm thick coated on a non-flat polymer-based photonic crystal biosensor with one-dimensional rectangular diffraction gratings was carried out. Five parameters, i.e. ion species, ion energy, incident angle, beam orientation relative to the diffraction grating wave vector, and ion fluence, was varied in order to study their effect on the surface topography, chemistry and optical transmission property. It was found that ion-beam irradiation was able to induce topographical changes and growth of nanostructured ripples while keeping the surface chemistry unchanged. The topographical changes depended on the irradiation conditions as well as the position on the surface. Despite the topographical changes, either the surface chemistry remained unchanged, as in the case of O_2^+ irradiation, or the oxidation state of TiO_2 was temporarily reduced, and then reverted back to the original state upon exposure to the atmosphere for a sufficient amount of time, as in the case of Ar^+ irradiation. In addition, it was found that irradiation caused a blue-shift in optical resonant peak wavelength, probably due to a decrease in film thickness by sputtering. Nevertheless, the peaks remained sharp and intense enough to be distinguishable from the background signal in most cases, implying the sensor's ability to detect peak wavelength changes, and thus act as a label-free

biosensor to detect changes in target molecule adsorption based on the peak wavelength changes, is not affected. It was further found that an additional resonant peak was present when irradiation was carried out at an oblique angle of 30^{o} relative to the edges of the diffraction gratings. This result is surprising, and the reason for this phenomenon was unclear. It might be related to the surface of the gratings being slanted towards one direction after irradiation. Further experiments in varying the beam orientation at a finer scale will be needed to examine the relationship between the topography and the appearance of extra resonant peaks.

The goal of this study was to induce nanostructures of varying shapes and sizes, and hence increase the surface area which in turn improve the biosensor sensitivity up to the magnitude achieved by GLAD deposition of nanorods observed in a previous research conducted by Cunningham et al. (~4x increase in the amount of proteins adsorbed onto the sensor). However, it was found that the changes in topography due to irradiation were able to increase the surface area by only a few percent, much less than that achieved by GLAD (~4x). In addition, the study to relate the presence of nanostructures to sensitivity of the biosensor, i.e. to relate the increase in surface area due to nanostructures to the amount of proteins adsorbed onto the surface, was inconclusive. Proteins of different sizes and different adsorption mechanisms were used, but there was no clear trends of the amount of proteins adsorbed on surfaces as functions of separation of nanostructures and increase in surface area due to these structures. Moreover, the trends shown from XPS and optical transmission results, two techniques to determine the amount of target proteins present on the surface, did not match with each other. These experiments need to be repeated in the future to average out the data and hopefully observe more insightful trends. More samples with different ripple periodicity and surface area will also be needed.

TABLE OF CONTENTS

CHAPTER 1: BACKGROUND ON TITANIUM DIOXIDE-COATED PHOTONIC-CRYSTAL-BASED BIOSENSORS

1.1 Introduction to biosensors

Biosensors, sometimes called "lab-on-a-chip," are able to perform both detection and analysis of biological signals. The International Union of Pure and Applied Chemistry (IUPAC) has defined the term "biosensors" as a device that is able to detect and analyze biological information quantitatively or semi-quantitatively using a biological receptor incorporated to a physiochemical transducer. [1] A biosensor is composed of three parts: a biological receptor, a transducer for converting biological signals to electrical signals, which can then be displayed in an output system. A schematic is shown in **Figure 1.1**. Among these three components, the transducer, as well as the interface between the receptor and transducer, determines the efficiency of biosensors. The transducer surface must enable strong and long-lasting binding of receptors onto it, while maintaining high receptor specificity and activity. [2] In addition, it has to be sensitive to changes in target concentrations. Especially when the detection involves very low concentration target analytes, for example cancer biomarkers during early stages of cancer having a concentration of 1 – 100 pg/mL only, the transducer surface has to be sensitive enough to detect the extremely small concentration of target analytes. [3]

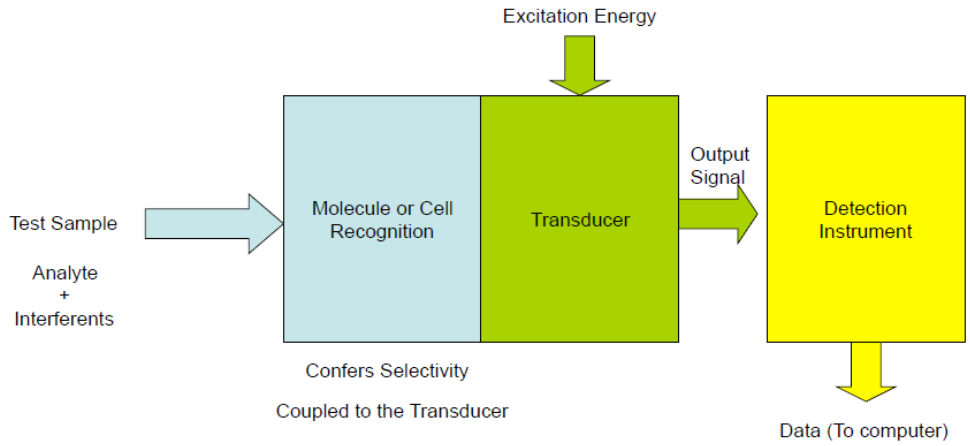

Figure 1.1 A schematic of a biosensor, consisting of a biological receptor, a transducer and an output system. [4]

Compared to other analytical devices, biosensors are small, simple, and able to perform measurements as well as analysis real-time. These advantages are exploited in the popular usage of small portable glucose biosensors, which are capable of recording real-time glucose levels of patients with diabetes, so adjustments of the amount of insulin injected to patients can be made more precisely and effectively. [1] In addition, the advantages of biosensors over other analytical tools have led to an extensive amount of research in recent years. For example, in 2015 alone, there were 2898 journal articles related to biosensors being published. [5] Despite these advantages, the performance of biosensors are still far from being perfect. For example, optical surface plasmon resonance (SPR) biosensors have started to become commercially used in the detection of protein biomarkers, DNA and bacteria in food and environment. However, researchers pointed out that major challenges still remain in ensuring the sensor surface binds specifically to target analytes only while maintaining a high sensitivity and low limit of detection (LOD). [6] Therefore, a lot of research opportunities in both improving the sensor functionality and tailoring it to commercial applications remain in the field of biosensors.

There are several types of transducers, the most common ones being electrical, optical, piezoelectric, and thermal. [1] Among them, theories, applications and potential improvements of label-based (fluorescent) and label-free optical biosensors will be the focus of this work. In particular, the focus will be on optical biosensors that utilizes photonic crystals, a piece of periodically-structured dielectric material that can amplify light output by orders of magnitude. This will be further presented below.

This thesis will be divided into the following sections: First, the working principle of photonic crystals and its role in biosensors will be addressed in **Chapter 1.2 – 1.4**. Next, a background of surface modification technique to address the need for an improved biointerface for a more sensitive transducer surface will be presented in **Chapter 2**. Then, the scope of this research to address the current knowledge gaps based on the work presented in the first two chapters will be presented in **Chapter 3**. After that, methodology of experiments being carried out to address the scope of research will be presented in **Chapter 4**. This is followed by results and discussion presented in **Chapter 5 – 8**. Finally, a conclusion and directions for future work will be presented in **Chapter 9**.

1.2 Theory of photonic crystals

Photonic crystal (PC), in its simplest description, is a piece of periodically-structured dielectric material that can control light propagation through that material. The propagation of light through a medium is governed by Maxwell's equations in matter, with the source-free and linear, isotropic, dispersionless and transparent material assumptions:

$$\nabla \cdot \boldsymbol{H}(\boldsymbol{r},t) = 0 \qquad \nabla \times \boldsymbol{E}(\mathbf{r},\mathrm{t}) + \mu_0 \frac{\partial \boldsymbol{H}(\mathbf{r},\mathrm{t})}{\partial t} = 0$$
$$\nabla \cdot [\epsilon(\boldsymbol{r})\boldsymbol{E}(\boldsymbol{r},t)] = 0 \qquad \nabla \times \boldsymbol{H}(\mathbf{r},\mathrm{t}) - \epsilon_0 \epsilon(\boldsymbol{r}) \frac{\partial \boldsymbol{E}(\mathbf{r},\mathrm{t})}{\partial t} = 0 \tag{1.1}$$

where $\boldsymbol{E}(\mathbf{r},\mathrm{t})$ and $\boldsymbol{H}(\boldsymbol{r},t)$ are the time and space varying electric and magnetic fields of the propagating light inside the medium respectively, $\epsilon(\boldsymbol{r})$ is the relative permittivity of the medium, and ϵ_0 and μ_0 are the vacuum permittivity and permeability. Generally, **E** and **H** are sinusoidally varying quantities, and are expressed as complex exponential functions:

$$\boldsymbol{E}(\boldsymbol{r},t) = \boldsymbol{E}(\boldsymbol{r})e^{-i\omega t}$$
$$\boldsymbol{H}(\boldsymbol{r},t) = \boldsymbol{H}(\boldsymbol{r})e^{-i\omega t} \tag{1.2}$$

The divergence equations in (1) merely tell us that the fields are source-free. We are more interested in the curl equations that can give us physical interpretation of the fields. Combining the curl equations, we obtain an eigenvalue problem: [7]

$$\nabla \times \left(\frac{1}{\epsilon(\boldsymbol{r})} \nabla \times \boldsymbol{H}(\boldsymbol{r}) \right) = \left(\frac{\omega}{c} \right)^2 \boldsymbol{H}(\boldsymbol{r}) \tag{1.3}$$

When the eigen-operator is periodic, for example in a PC with a periodic geometry in one dimension where $\epsilon(\boldsymbol{r})$ is periodic, an example shown in **Figure 1.2**, $\mathbf{H_k}(\mathrm{r})$, the $\mathrm{k^{th}}$ eigenmode of **H**(r), can be expressed as a periodic wave function known as a Bloch state according to Bloch's theorem: [7]

$$\boldsymbol{H}(\boldsymbol{r}) = e^{i\boldsymbol{k}\cdot\boldsymbol{r}}\boldsymbol{u}_{\boldsymbol{k}}(\boldsymbol{r}) \tag{1.4}$$

where **k** is called a Bloch wave vector, with the form $\boldsymbol{k} = k_1\boldsymbol{b}_1 + k_2\boldsymbol{b}_2 + k_3\boldsymbol{b}_3$, where ($\mathbf{b}_1$,$\mathbf{b}_2$,$\mathbf{b}_3$) is called the primitive reciprocal lattice vector. Putting (4) into (3), together with the equation $\nabla \cdot \boldsymbol{H}(\boldsymbol{r}, t) = 0$ and the periodicity condition $\boldsymbol{u}_{\boldsymbol{k}}(\boldsymbol{r}) = \boldsymbol{u}_{\boldsymbol{k}}(\boldsymbol{r} + \boldsymbol{R})$, the periodic function $\boldsymbol{u}_{\boldsymbol{k}}(\boldsymbol{r})$ as well as its eigenvalues $\omega(\boldsymbol{k})$, which is also the frequency of the light, can be solved. In a medium with a uniform $\epsilon(\boldsymbol{r})$ lights with all frequencies can pass through. However, in a multilayer PC structure, for example the one shown in **Figure 1.2**, there exists a photonic band gap, analogous to the electronic band gap in semiconductors, in which light with certain frequencies within the photonic band gap cannot pass through the PC. The width of this photonic band gap is proportional to the difference in dielectric constants between the two media. [7]

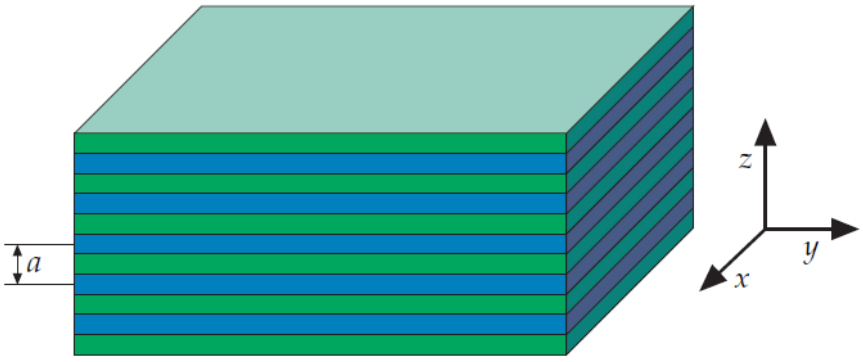

Figure 1.2 A PC with one dimensional periodic symmetry in z direction and uniformity in x and y directions. The structure consists of multilayers made of two materials with different dielectric constants stacking between each other, so that $\epsilon(\boldsymbol{r})$ is periodic in z. a represents the length of a repeated unit. [7]

A PC structure can be further engineered to include diffraction gratings on its surface. Here, we will only consider one-dimensional diffraction grating. Such structures are sometimes called resonant grating waveguide structures (GWS). The simplest GWS can be formed with a thin

waveguide layer with one-dimensional rectangular gratings on top of a substrate layer with a refractive index different from that of the waveguide layer. [8] A schematic is shown in **Figure 1.3**. When a light beam is incident onto the GWS into the waveguide layer, it undergoes both refraction and then transmission out of it (beam t), and diffraction within it (beam b). Most of the diffracted beam is confined inside the waveguide layer by total internal reflection (beam c), but a part of it may be diffracted again by the grating and then transmitted out of the layer (beam s). [8] Beam t and beam s are collinear, and they differ only by their relative phases. The phase shift between beam t and beam s is composed of four contributions: path length difference, total internal reflection, and phase difference due to diffraction, and phase difference due to a change in refractive index due to the presence of the gratings. The phase shift is found to be: [8]

$$\Phi = \Phi_p + \Phi_r + \Phi_d = 2k_3 v + 2\Phi_1 + 2\Phi_4 - \pi \tag{1.5}$$

where Φ is the total phase shift, $\Phi_p = 2k_3 v$ is the phase difference due to path length difference, $\Phi_r = 2\Phi_4$ is the phase difference due to reflection at the waveguide-substrate interface, $\Phi_d = \Phi_1 - \frac{\pi}{2}$ is the phase difference due to diffraction and refractive index change, k_3 is the wavevector in layer 3 (waveguide layer), v is the thickness of layer 3, Φ_1 is the phase difference due to the presence of the gratings, and Φ_4 is the phase difference due to total internal reflection. Resonance occurs when the confined waves inside the waveguide layer are able to propagate. Mathematically, it requires $2k_3 v + 2\Phi_1 + 2\Phi_4 = m2\pi$, where m is any integer. This indicates at resonance the total phase difference becomes a multiple of π, which implies beam t and beam s undergo complete destructive interference. All the waves are either reflected away from the grating surface or

propagate inside the waveguide at resonance. This is achieved when the incident light has a certain wavelength and angle relative to the grating dimensions and the refractive index of each layer. [8]

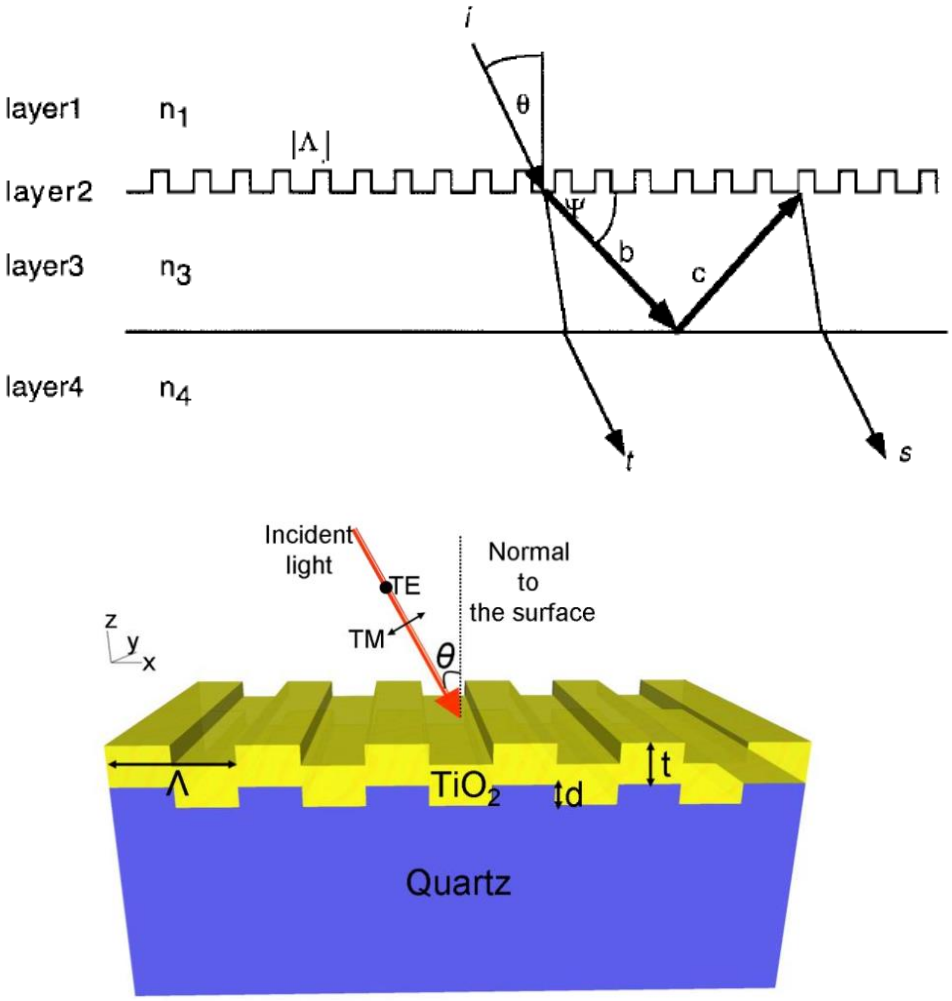

Figure 1.3 Top: A schematic of a GWS and the propagation of light through the medium. n_1, n_3, n_4 are the refractive indices of layer 1, 3 and 4 respectively. [8] Bottom: An example of PC with one-dimensional GWS. [9]

The resonant behavior when incident light is able to couple to the specific resonant mode of the GWS allows extremely strong reflection of light at the surface. At resonance, some waves inside the waveguide layer slowly but continuously "leak out" and couple with the reflected wave on the surface. This causes the presence of a strong evanescent electric field, which enhances the reflection field intensity near the surface. Such enhancement can achieve over two orders of

magnitude relative to the intensity of the incident light. [9,10,11] In addition to intensity enhancement, the light reflected off the surface is almost unidirectional, the direction controlled by the properties of the GWS structure. [8,12] Since little scattering of light occurs, most of the reflected light can be collected by a detector if placed at the correct direction. This minimizes any losses of the reflected signal from the PC surface, making it a very promising candidate for many engineering applications, a few being as filters, sensors, and beam splitters.

Another requirement for the "leaky mode" resonance to occur, in addition to a specific incident wavelength and angle, is that the refractive index of the grating and waveguide layer has to be higher than that of the substrate layer and the surroundings lower than that value, and they satisfy the inequality relative to the incident light and grating parameters:

$$\max\{n^c, n^s\} \leq \left| n^c \sin\theta - \frac{p}{\nu\Lambda} \right| < \max\{n^{gr}, n^{wg}\} \tag{1.6}$$

where n^c, n^s, n^{gr}, n^{wg} are refractive indices of the surroundings, substrate, gratings, and waveguide respectively, θ is the angle of incidence of the incident light, p is the p^{th} propagation mode of the incident light, ν is the wavenumber of the incident light, and Λ is the grating wavelength. [10] Therefore, it is convenient to fabricate the waveguide and substrate layer using a high and low refractive index dielectric material respectively.

1.3 Role of photonic crystal in optical and fluorescence biosensors

As already mentioned in **Chapter 1.1**, researchers have been investigating in utilizing the unique properties of PC described above to incorporate into optical and fluorescence biosensors. For

fluorescence sensors, PC is able to significantly enhance the fluorescent output signal through two processes: “Enhanced excitation” and “enhanced extraction.” Enhanced excitation describes the process in which fluorescence signal from fluorescent labeled target analytes adsorbed onto the sensor surface is significantly enhanced at a PC resonance due to coupling to the strong evanescent field originated from the PC surface. On the other hand, enhanced extraction describes the process in which the emitted light from the fluorophores, being coupled to the strong field near the PC surface similar to the case in enhanced excitation, are able to be captured by the detector with little losses when placed at a proper direction, since the reflected light from the PC surface propagates with little scattering. [9,12] Cunningham et al. has demonstrated the incorporation of PC into fluorescence biosensors can lead to a significant enhancement of fluorescent signal output due to the unique properties of PC, as described above. The PC biosensor used by the researchers was composed of a high refractive index titanium dioxide (TiO_2) thin film deposited on a low refractive index dielectric substrate with a one-dimensional GWS structure patterned onto its surface. Using PC incorporated fluorescence biosensors, the researchers have demonstrated an enhancement in both the fluorescence signal and signal-to-noise ratio (SNR) by up to approximately 60 × and 10 × respectively in gene detection. This implies the usefulness of PC in detecting low expression genes, which are often essential housekeeping genes that have a low abundance in cells. [9,13,14] The researchers have also demonstrated the use of PC in breast cancer biomarker protein detection for early cancer diagnosis when the biomarkers only exist in a tiny amount at the early stage of cancer. Their results showed an enhancement in signal intensity, SNR and limit of detection (LOD) by 11-20 ×, 3.8-6.6 ×, and 6-89% respectively. This enables detection of the cancer biomarkers with a concentration <2 pg/mL in a mixed sample of different biomarkers. [3] Frascella et al. have also demonstrated the use of 1D photonic crystal with multiple layers of high and low refractive

index films periodically stacked between each other as a label-free fluorescence biosensor that utilizes the coupling of BSW with the fluorescence radiation of fluorescent dyes on the surface to monitor the binding of a target protein onto the surface in real-time with low SNR. [15] Higher dimensions PC structures have also been investigated in enhancing fluorescence output from colloidal quantum dots (QDs), metallic and semiconductor nanoparticles that are very popular as fluorescent labels instead of organic dyes for fluorescent biosensing due to their interesting optical properties as a result of the quantum confinement effect. [16,17]

In addition to the application in fluorescence spectroscopy, PC incorporated biosensors are also very promising in label-free optical biosensing. The principle of optical biosensing using PC sensors is by measuring a Peak Wavelength Value (PWV) shift induced by a change in the relative permittivity, and hence refractive index, of the sensor surface when biomolecules in the liquid media surrounding the surface adsorb onto it. A PWV results when a specific resonant wavelength of light in a white light incident onto the surface, the resonant wavelength dependent on the configuration of the PC structure, is reflected off the surface while the rest is transmitted. [18] Kaja et al. have demonstrated that label-free optical biosensors incorporated with a PC structure is a promising method in fast, accurate and sensitive diagnosis of different stages of ovarian cancer. Enzyme-linked immunosorbant assay (ELISA), the most frequently used traditional biological assays for protein biomarkers, cannot be used with ovarian cancer diagnosis due to the absence of standards for ELISA tests for ovarian cancer biomarkers. Compared to other traditional assays such as quantitative immunoblotting, label-free optical biosensors are able to perform detection of several of the biomarkers for ovarian cancer with a 40-fold LOD enhancement with fewer experimental steps, while maintaining the desired level of accuracy. [19] Shafiee et al. have shown the potential of PC optical biosensors in early detection of HIV-1 virus, the most common type of

HIV virus, in a biological sample with enhanced sensitivity and repeatability. The detection limit can be as low as 10^5 copies/mL, the concentration present in a person during the beginning of HIV-infection. [20] Zecca et al. have demonstrated the use of two-dimensional PC with periodic cavity patterned on a silicon nitride membrane in detection of very low concentration of interleukin-6 (IL-6) protein, a cytokine . The researchers were able to achieve a detection limit of 1.5 pg/mL of IL-6 protein, which was comparable to the typical IL-6 concentration in a patient which is higher than 1 pg/mL. They also pointed out that detection using label-free PC enhanced sensor is more efficient and enables real-time measurements compared to typical assays such as ELISA. This is because ELISA typical involves multiple time-consuming steps, while in label-free optical sensing, the PWV signal output whenever a protein is adsorbed onto the sensor surface can be measured and interpreted quickly and directly. [21] All these examples described above indicate the potential of PC-based biosensors in fast, accurate and sensitive sensing of different protein biomarkers, and hence opportunities in further research in optimizing the performance of PC incorporated biosensors, such as maximizing their sensitivity, minimizing their LOD and improving selectivity.

1.4 Titanium dioxide (TiO_2) as a waveguide layer and a biomaterial

As described above, the use of PC sensor involves a thin waveguide layer. This waveguide layer has to have good optical properties and biocompatibility for the sensor to function well. Titanium dioxide (TiO_2) is considered a good candidate as the waveguide layer for several reasons. First, for a long period of time, TiO_2 and nanostructured TiO_2 have been a versatile material in numerous applications, including pigment, solar cells, photolysis of water for hydrogen production, and so on. [22,23,24] TiO_2 has a very high refractive index, making it a desirable material for the high refractive index film layer in the PC structure described in **Figure 1.3**. At a light wavelength of

550 nm, the refractive index of TiO_2 can range from 1.9 to 2.56, depending on the film deposition technique and condition. [25] It also has excellent electro-optical properties, such as the aforementioned high refractive index, a wide optical band gap of 3.2 eV [25], high transparency in visible and near-infrared regions, and low extinction coefficient (~ 10^4 at a wavelength of 550 nm [25]), making it a good candidate for optical and electronic applications such as a dielectric layer in semiconductors, a waveguide layer on PC crystals, a coating on optical sensors, and an antireflection optical coating on solar cells. [25,26,27,28,29] Alasaarela et al. have demonstrated the use of TiO_2 as a waveguide layer on a PC substrate, and have observed a nearly 100% reflectance at the resonant wavelength, which implies the loss in light propagation is very low. [26] Mondal et al. have faricated a TiO_2 thin film as a dielectric layer on a metal-oxide-semiconductor (MOS) capacitor device. The TiO_2 dielectric was found to have a low leakage current of 9.5×10^{-5} A/cm^2 when an electric field of 1 MV/cm was applied across the device. It also had a very low number of trapped charges (~8.2×10^{-12} C). [27] Tiwari et al. have used TiO_2 as an optical coating on tapered optical fibers as fast sensitive sensors for the detection of ammonia, and the researchers have been able to detect ammonia in water that has a concentration of 0.1 ppm only in less than 30 s. [28] Haider et al. have shown that TiO_2 doped with a few wt% of Ni can be used as an antireflective coating on solar cells. A very low reflective of ~25% at a light wavelength of 550 nm and a wide band gap of 3.82 eV has been reached. [29] Based on these examples, it is clear that TiO_2 can a good material as a waveguide layer on PC biosensors as well.

Aside from being a good waveguide layer, TiO_2 has excellent biological properties that make it a desirable biomaterial. It is well known that titanium metals are excellent materials used in biomedical applications, such as fabrication of artificial joints, due to its high resistance against corrosion, chemical inertness, and ability to repassivate the surface. These properties are all due to

the presence of a thin naturally grown oxide film on the titanium surface. [30] Therefore, when titanium is considered biocompatible, it is the thin oxide film that contributes to its biocompatibility. Besides, there are numerous research demonstrating TiO_2 to be a safe and biocompatible material for many biological applications including being an additive in toothpaste and cosmetics, and also chemically stable and safe to human and the environment. [31,32,33,34,35] In fact, while numerous research has been done on titanium and titanium alloys in biomedical applications, there is also emerging research on the biomedical use of nanostructured TiO_2. TiO_2 nanotubes are engineered as a stable interface for label-free optical biosensors over a wide range of pH values. In particular, it shows good specificity and biocompatibility for protein detection. [36,37] For example, Mun et al. have engineered TiO_2 nanotubes on Ti-based label-free optical biosensor for sensing of rabbit immunoglobulin G (IgG). The researchers were able to operate the sensor within a pH range of 2 – 12, a range much greater than sensors made of other common materials such as porous SiO_2, which cannot work in basic environment, and porous Al_2O_3, which cannot work in acidic environment. They have also shown that TiO_2 surface, when functionalized with protein A via noncovalent binding, a protein that acts as a capture probe for rabbit IgG, can specifically adsorb rabbit IgG while inhibiting adsorption of another protein used in the experiment (chicken IgG). The structure of the surface and adsorption results are shown in **Figure 1.4** [36] Porous TiO_2 have been shown to be a promising candidate for future enzymatic biosensors due to increased surface area and the presence of nanostructures appeared on the porous TiO_2 surface, which lead to enhanced sensitivity, specificity and effectiveness of the sensor. [35] TiO_2 nanoparticles have been shown to potentially become a novel material as intracellular diagnostic tools such as cancer cell detection, gene sequencing and therapy, when combined with DNA oligonucleotides. [38,39,40] For example, Thurn et al. have demonstrated the use of TiO_2

nanoparticles in linking to single-stranded NDA oligonucleotides, which has the potential for detection of specific genes and tumors. The fluorescent-labeled TiO_2 nanoparticles were able to enter cells and show a strong fluorescent signal, as shown in **Figure 1.5**. During the process only a few percent of cells were dead, implying good biocompatibility of these TiO_2 nanoparticles. [39] All these have shown the immense potential of TiO_2 and nanostructured TiO_2 as biointerfaces for sensor applications.

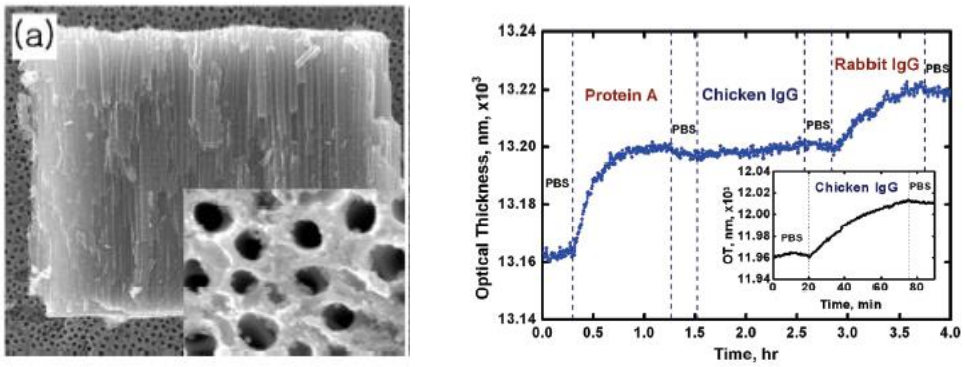

Figure 1.4 Left: SEM image of sensor surface with TiO_2 nanotubes. Right: Adsorption of protein A, rabbit IgG and chicken IgG, indicated by the increase in thickness of adsorbed layer measured optically. Inset is protein adsorption without protein A. [34]

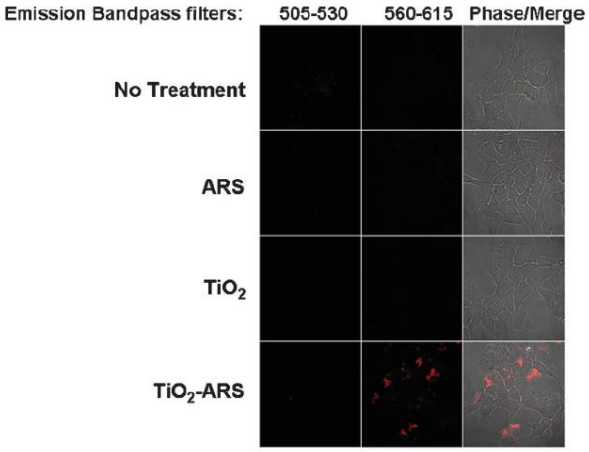

Figure 1.5 Fluorescent signal from prostate cancer PC-3M cells without any label, with Alizarin Red S (ARS, a label that can enhance fluorescent signal from nanoparticles), with TiO_2 nanoparticles only, and with ARS-tagged TiO_2. Different excitation wavelengths were used. [37]

CHAPTER 2: NANOPATTERNING BY ION-BEAM IRRADIATION

2.1 Theory and application of nanopatterning

The study of nanopatterning originates from the understanding of how energetic ions, electrons, free radicals and neutral atoms interact with the target surface upon impact. There are several mechanisms responsible of the evolution of surface changes due to ion impact, e.g. collision cascade, thermal spike, sputtering, ion implantation, deposition, phase transformation, and so on. [41] When ions above a threshold energy enters a target surface, these ions collide and exchange energy and momentum with lattice atoms, causing these atoms to displace from its original lattice site if the energy transferred to the atoms is larger than its displacement energy. These lattice atoms can further displace other lattice atoms nearby, thus creating a disordered region with vacancies and interstitials around the paths of incident ions. This region is called a collision cascade. [41] A simplified schematic of the collision cascade is shown in **Figure 2.1**. Eventually the incident ions slow down and reach an energy equilibrium with the surrounding lattice atoms and are implanted inside the target. [42] At the end of the traveling of ions, when they slow down to a point at which their mean free paths are comparable to the interatomic distance of the lattice atoms, the disordered regions become a highly damaged region which consists of an empty void formed by vacancies and surrounded by interstitials. This region is called a displacement spike. [41] At the end of the displacement process, when most of energy of the displaced atoms is already dissipated and the remaining energy is below the displacement threshold, this amount of energy is further dissipated as heat within the region instead. This is called a thermal spike. Thermal spike can cause a local phase transformation from the lowest-energy equilibrium phase to a metastable phase which has a higher free energy. Examples of phase transformation includes amorphous to crystalline phase and

vice versa, amorphous to quasi-crystalline phase, alloy to solid solution, and so on. In addition to thermal spike, defects induced by irradiation such as vacancies, interstitials and dislocations also contributes to the energy needed for the transformation to occur. [41] A collision cascade can also result in some lattice atoms close to the surface to scatter backward and leave the surface, known as sputtering. [43] If the surface is composed of more than one species, preferential sputtering of one species over the other will happen, the ratio depending on the difference in masses between each species and the incident ions, causing a change in surface composition. [41]

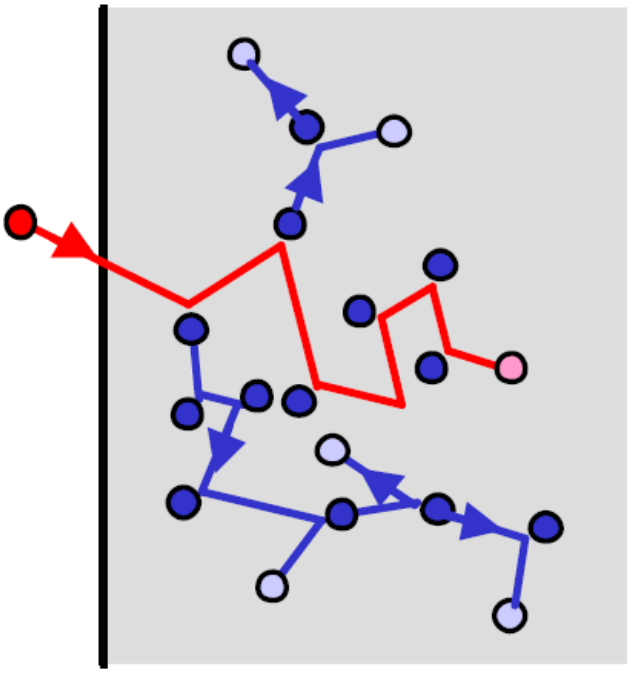

Figure 2.1 A simplified schematic of a collision cascade. Red line indicates the trajectory of the incident ion after impact with substrate atoms. Blue lines indicate the recoil trajectory of substrate atoms due to impact by incident ion and other adjacent atoms. [44]

Over the years, ion-beam interaction with surfaces have been utilized in a wide variety of applications that require precise surface modification techniques. Sputtering, etching, thin film deposition and ion implantation by ion-beams and plasmas are crucial processes in modern

semiconductor chip fabrication. [45, 46] Modification of surfaces can also lead to more biocompatible surfaces by tuning the surface morphology and chemistry. This is described in detail in section 2.2. Several material characterization techniques, such as secondary ion mass spectroscopy (SIMS) and secondary neutral mass spectroscopy (SNMS), are based on analysis of sputtered ions and neutral atoms. [47,48] One important advantage of using ion-beam irradiation is that it only modifies the very thin surface layer, leaving the bulk substrate unaltered. [49] Irradiation also offers precise controllability of surface modification in the nanoscale, which ordinary surface modification techniques cannot offer. Compared to some well-established patterning techniques such as electron beam lithography, ion-beam patterning has unique advantages in a few aspects including minimization of the number of steps and thus processing time, complex pattern designs, and adaptability in vast majority of surface modification applications. [45] Such precise controllability can be achieved by controlling the ion beam parameters, i.e. ion species, energy, angle of incidence and fluence. Another advantage is that ion irradiation is capable of simultaneously physically and chemically modifying the surface. For example, it is believed that performing chemical and physical modification together influences protein uptake to a greater extent than either way alone. [50] Therefore, ion irradiation has the capability of precisely modifying surfaces to adapt to different biological analytes for optimum detection and analysis using different irradiation parameters.

The formation of ripples and various nanostructures on surfaces is a result of a self-organization process. Self-organization is an energy-driven non-linear process in which interactions between microscopic components, for example particles from an external ion beam source and the atoms on a surface, bring the system to a final state with differing properties from its initial state. [51] Several theoretical and simulation models have been developed to predict structure formation by

ion bombardment, with two of the earliest and most significant models being the one proposed by Sigmund, and the one by Bradley and Harper. Sigmund has developed a theoretical model to explain the occurrence of surface nanostructures due to surface micro-roughening. When an incident ion approaches a surface, which is generally smooth with only very small surface features due to defects, at an angle with respect to the surface normal, preferential sputtering happens on these small features, with a sputtering yield higher at the lower part of the features than at the higher part. This causes a growth of these features into larger structures, illustrated in **Figure 2.2**. [52] Based on Sigmund's model, Bradley and Harper has proposed that such micro-roughening causes sinusoidal instabilities along the surface. This perturbation causes the growth of periodic ripples on the material surface, with a wavelength that is dependent on the incident flux, temperature and the activation energy for surface self-diffusion, given that the temperature is sufficiently high and the flux is low. The orientation of the ripples is also dependent on the angle of incident ion beam. The wave vector of the ripples is parallel to the beam direction if the incident angle relative to the surface normal is smaller than a critical angle, which is usually close to 70^{o}, and is perpendicular to the beam direction instead if otherwise. In addition, their model proposes the sputtering rate is dependent on the surface curvature. Sputtering at troughs is at a higher rate than at crests because the average energy deposited on the slopes within the troughs is higher. [53] Many other researchers have later proposed various theoretical and computer simulation models to explain the phenomena that the Bradley-Harper model is insufficient to explain. For example, the mass redistribution effect induced by ion impact on the surface is shown to have a dominant effect over sputtering on topographical changes and is able to explain the ultra-smoothening effect at small angle incidence from the normal and surface instability at large angle. [54,55,56] The nonlinear effect is also introduced into the linear Bradley-Harper model by the formation of a

nonlinear stochastic model by Cuerno and Barabási to account for the saturation of the ripple amplitude at extended sputtering time. [57] Various other nonlinear models have also been proposed to further explain the nonlinear behaviors occurring in the structure formation. [58,59,60] Models based on kinetic Monte Carlo method have also been developed to predict topographical changes based on interaction of individual ions with the surface. [61,62,63] A review of the development of these theoretical models and experiments to compare with the theoretical predictions can be found in a review paper by Keller and Facsko. [64]

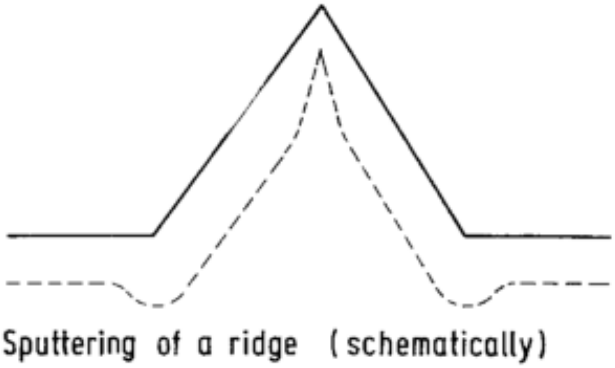

Figure 2.2 An illustration of sputtering at a small feature on a surface. Sputter yield at the lower part of the feature is higher than at the top. [52]

The induced surface changes by energetic ions as a result of the self-organization process has led to the study of surface nanopatterning. Compared to its counterpart self-assembled process, a non-energy driven spontaneous process in which the microscopic components assemble in a thermodynamically favorable way to minimize the energy in their final state, [51] the addition of external energy and the non-linearity inherent in self-organization can possibly induce a wide variety of nanopatterning and nanoparticle growth that may not be thermodynamically favorable in a self-assembly process. One of the earliest and most extensively studied area is ripple formation on silicon (Si) due to its extensive applications in microelectronics. [64] Several papers have

shown that ripples ranging from a few tens of nms to several hundreds of nms in periodicity and a few nms in amplitude can be induced on crystalline and amorphous Si surface by the appropriate control of ion species, energy, angle of incidence, fluence and surface temperature. [65,66,67] Nanodots on Si have also been observed by rotating the sample during ion-beam irradiation, [66] and their sizes can be controlled by varying the surface temperature. [68] The formation of nanostructures have been shown to be significantly influenced by co-deposition of a small amount of metal impurities, resulting in entirely different surface morphologies compared to the absence of these impurities. [69,70] All these examples indicate numerous possibilities in engineering different nanostructured surfaces as needed by ion-beam irradiation.

Besides nanopatterning on bulk substrates, Studies on thin film nanopatterning have also become increasingly popular. Ion-beam irradiation of thin films can also induce ripples and other nanopatterns similar to irradiation of bulk substrates. [71,72] However, there are a lot of other aspects of ion-material interactions that need to be considered, for example ion-beam-induced modification of film crystallinity, influence of thin film crystal structure on nanopattern formation, mixing of elements at the film-substrate interface (also known as ion-beam mixing), as well as modification of intrinsic stresses in thin film. [73] Elliman et al. have shown that 80 keV Sb^+ ion implantation into Si(100) substrate at ~ 77K can create an amorphous Si layer of ~80 nm thick on top of the substrate. This amorphous layer can be recrystallized by irradiation of He^+ ion irradiation with energies in the range of tens of keV. [74] Ghose has studied the formation of ripples on various polycrystalline and amorphous metal films, and observed that for polycrystalline films, high density of grain boundaries may influence ripple formation in a different way from amorphous films. Especially for thicker polycrystalline films of the order of 1 μm thick, these grain boundaries and the crystallographic orientation may affect which grains the ripples prefer to

grow on, due to the presence of Ehrlich-Schwoebel (ES) barrier, a diffusion barrier at the step edges of a crystal surface that affects the diffusion of surface adatoms. [71] This effect is also demonstrated by Qian et al, who studied the dependence of ripple orientation on the direction of the grain boundaries of tin (Sn) surface. The researchers observed that under 30 keV Ga^+ focused ion beam irradiation, with the presence of grain boundaries, the orientation of ripples depend on the direction of the boundaries rather than the direction of the ion beam. [75] Ion irradiation can also induce mixing of elements from both the film and substrate at their interface to improve adhesion of the film. This phenomenon is used as a basis for ion beam assisted deposition (IBAD), [41] and has been utilized in many applications. For example, Ohtsuka et al. demonstrated the use of IBAD in the deposition of hydroxyapatite (HA) coating on Ti substrate for application in bone implants. With the use of IBAD, the researchers were able to deposit the HA film on the Ti substrate with a significantly higher adhesive strength (>59.0 MPa) than the film deposited by conventional methods such as plasma spraying (31.9 MPa) and physical sputter deposition (8.02-45.82 MPa). [76] However, careful attention should be paid to the stresses induced by ion irradiation, although it can be controlled by controlling the irradiation conditions. For example, Khan et al. have studied thin film nanopatterning by 800 keV carbon ion irradiation on ZrN films, which are great candidates for corrosion-resistant coatings on mechanical tools and other tools that require coatings of high stiffness, high corrosion resistance and low electrical resistivity, and were able to control the irradiation-induced compressive stress in the film. The researchers have found that the compressive stress after irradiation increased from 1 GPa to 2.75 GPa initially when the ion fluence was low (1×10^{13} cm^{-2}), but the stress gradually decreased down to 1.37 GPa when the fluence was increased to 1×10^{15} cm^{-2}. [77] Goudeau et al. have also demonstrated the use of ion irradiation to reduce the residual stresses in thin films to improve the mechanical stability of the

film and substrate. The researchers irradiated a polycrystalline Mo thin film on a Si susbtrate with 400 keV Ar^+ ions and were able to reduce the residual stress of the film from -2.0 ± 0.2 to – 0.9 ± 0.1 GPa, although the energetic ions also induced defects at the film-substrate interface and even film delamination. [78] Furthermore, there is an emerging research on nanopatterning on high-temperature superconducting (HTS) thin films for the next generation electronic devices. For example, Bodea et al demonstrated the use of 75 keV He^+ ions to create nanopatterns on a HTS film with the composition of $YBa_2Cu_3O_7$ (Y-123) with the use of a mask. The topography is shown in **Figure 2.3**. Since it is observed that the electrical resistivity of the film increases significantly after irradiation (at a low fluence of 7 x 10^{14} cm^{-2} it is observed the resistance is increased by 3 times), the researchers believe nanopatterning with the use of a mask can be utilized to induce superconductivity in certain regions only and non-superconductivity in other regions. [79] In addition to the aspects described above, unlike bulk substrates, sputtering rate has to be put into consideration in thin film irradiation so that the film will not be removed entirely. This indicates that the film thickness pose a limitation to the irradiation parameters, which directly influences the sputtering rate. However, in some cases the thin film can be intentionally removed to engineer interesting nanostructures on the substrate that is difficult to be achieved on a bulk substrate alone. For example, Stepanova et al. discovered the ability to create Cu islands by ~ 1 keV Ar^+ sputtering of ~ 50 nm Cu thin film on a Si or glass substrate until the film/substrate interface is exposed. [80] This may imply the possibility of using ion-beam irradiation as a fast and simple way to create metal nanodots, provided that the irradiation parameters are precisely controlled. This is also shown by El-Atwani et al., who utilized a 10 nm gold ultra-thin film as a catalyst for formation of Si nanodots on the underneath Si substrate via low energy (200 eV) Ar^+ ion-beam irradiation until the gold film has been removed. [81]

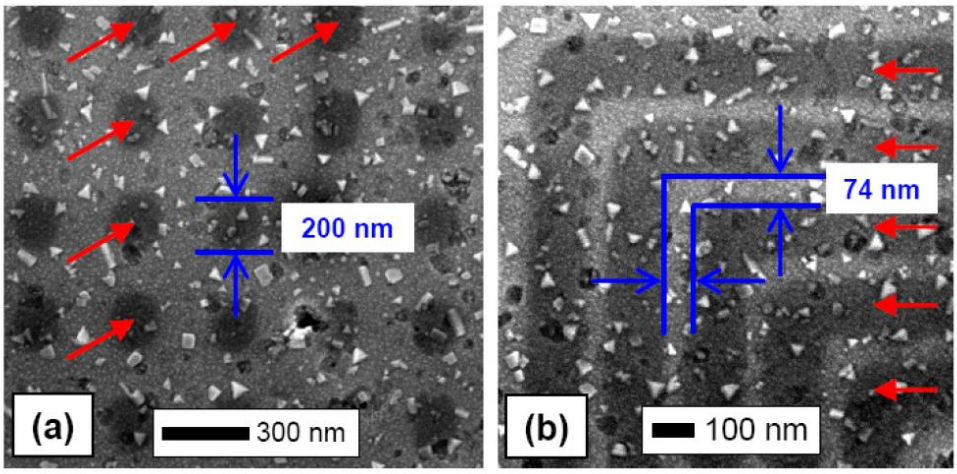

Figure 2.3 SEM images of nanopatterned $YBa_2Cu_3O_7$ HTS film by 75 keV He^+ ions with the use of a mask. Red arrow indicates regions exposed to ions. Left and right figures show nanopatterns formed with the use of different masks. [79]

Besides Si, nanopatterning on TiO_2 is also an emerging area of research, aiming to improve its performance both in solar cell and biomedical applications. It is shown that the photoelectric performance of porous TiO_2 film-based dye-sensitized solar cells (DSSCs) can be improved by treating the surface with O_2 plasma. O_2 plasma can reduce the inherent oxygen vacancies appeared during fabrication of the film, increase surface wettability and reduce surface hydrocarbon contaminants. This enhances dye adsorption and reduce electron trapping inside the vacancies during electron transfer from excited dye molecules to the TiO_2 surface, which is important to the performance of DSSCs. [82] On the other hand, Solanki et al. have shown that increasing in oxygen vacancies, when coupled with the growth of nanostructures on the surface to increase the surface area, can enhance absorption of photons for photovoltaic applications. The researchers have shown that 60 keV Ar^+ irradiation of TiO_2 single crystal at 60^o incident angle with fluences between 5×10^{15} to 5×10^{17} cm^{-2} resulted in formation of two-dimensional nanostructures and an increase in oxygen vacancies, indicated by a reduction of Ti^{4+} state to lower oxidation states Ti^{3+} and Ti^{2+}, and these modifications to topography and chemistry resulted in enhanced light absorption. These results are shown in **Figure 2.4**. The researchers stated that the presence of

nanostructures increased the surface area, which in turn increased the amount of active sites on the surface for adsorption of photons. The effect was further amplified by an increase in oxygen vacancies. This is because these vacancies act as active sites for capturing photo-excited electrons, inhibiting their recombination with the holes, and thus enabling an increase in light absorption. [83] Nanorods and nanopores on the surface of both bulk TiO_2 crystal and thin TiO_2 film have been grown by high energy N_2^+ and C^+ irradiation for enhanced performance in photolysis of water for hydrogen production. [84,85] Also, the size of nanopores in porous TiO_2 thin film can be increased using O_2^+ irradiation, resulting in an increase in the total surface area, the volume and size of the pores by around 19%, 50%, and 18% respectively after irradiation at an ion energy of 500 eV and fluence of 2.79 x 10^{17} cm^{-2}. [86] In addition to growing nanostructures, many researchers also aim at changing the surface wettability for specific applications. For example, the TiO_2 surface can be modified from naturally hydrophobic to super-hydrophilic temporarily when exposed to UV irradiation. Zheng et al. observed that upon exposure to UV light with a power of 300 W and wavelength of 250 – 400 nm for 30 mins, the water contact angle on a flat TiO_2 film was decreased from 110 ± 1.5^o to ~ 0^o. Such a reduction was reverted when the film was blocked from any light source for a week. This is shown in **Figure 2.5**. [87] O_2^+ irradiation is also capable of converting hydrophobic TiO_2 surface to temporarily hydrophilic. After irradiation at ion energies of 500 eV and 1000 eV and fluence of 2.79 x 10^{17} cm^{-2} and 3.19 x 10^{17} cm^{-2}, it is found that the contact angle decreases from 21.6^o to 7.5^o and 8.8^o respectively, and such decrease has sustained for at least 72 hours. [86] The super-hydrophilic TiO_2 surface can be utilized for coating on anti-fogging and self-cleaning glasses. [87,88,89] Furthermore, ion-beam irradiation on TiO_2 can cause surface chemical changes depending on the irradiation parameters. Sputtering using low energy Ar^+ ions can cause a reduction of TiO_2 from Ti^{4+} state to the lower Ti^{3+} and Ti^{2+} states, and

the ratio of the states depend on the sputtering energy and time. [90] Similar effects can also be seen when plasma treatment with different species, e.g. O_2, N_2 and CF_4 plasmas, are performed. [82] In particular, when non-oxygen reactive ions, for example N_2^+ ions, are involved, the composition of the surface can change from pure TiO_2 to TiO_2 plus some TiN or even TiN_xO_y. [91,92] The changes in the Ti2p state, and thus the stoichiometry of the surface, is due to the preferential sputtering of oxygen atoms when light ions are used, causing a non-stoichiometric ratio of Ti to O on the surface and forming non-stoichiometric compounds of Ti_xO_y, or TiN_xO_y if nitrogen ions are involved. [91,92,93]

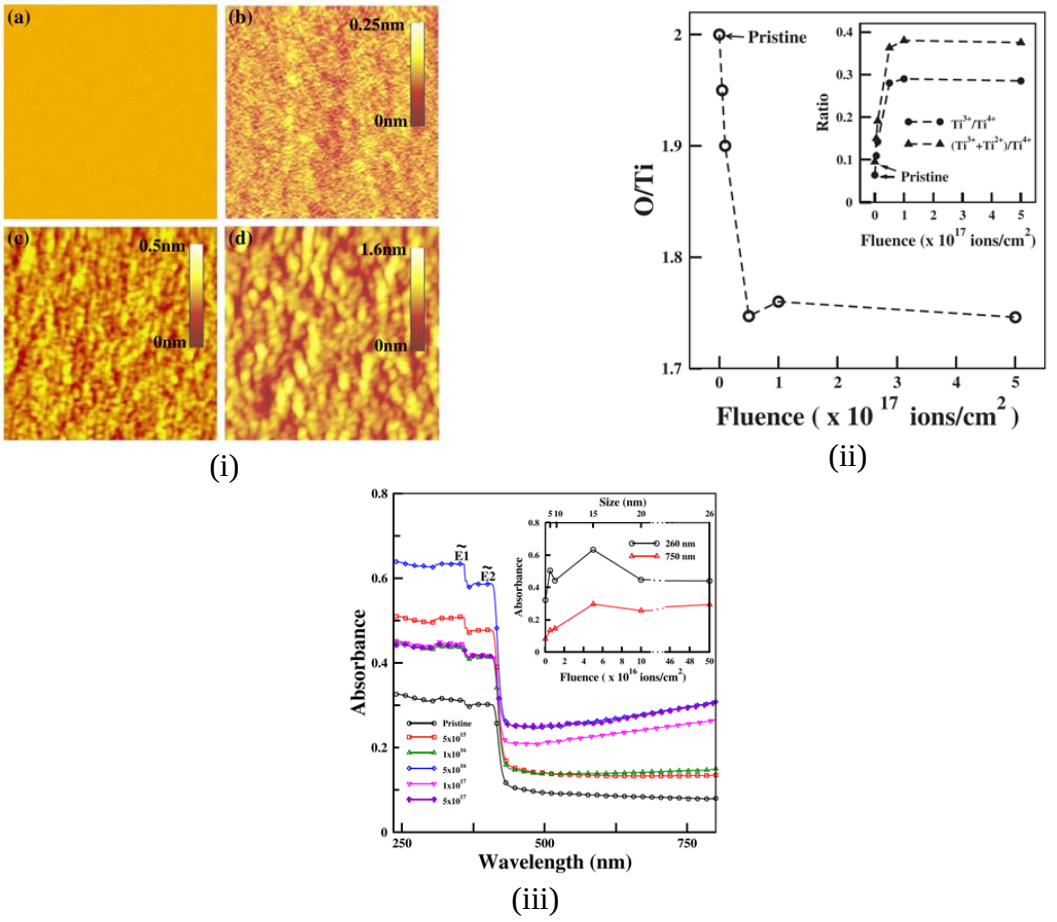

Figure 2.4 (i) SPM images of TiO_2 surface after irradiations, showing the presence of nanostructures of different sizes. (a) pristine, (b) irradiated with fluence of 5 x 10^{15} cm^{-2}, (c) 1 x 10^{16} cm^{-2}, and (d) 1 x 10^{17} cm^{-2}. (ii) UV-Vis absorption spectra of TiO_2 surfaces irradiated with different fluences. (iii) Ratio of O/Ti, Ti^{3+}/Ti^{4+} and $(Ti^{2+}+Ti^{3+})/Ti^{4+}$ on TiO_2 surfaces irradiated with different fluences. [83]

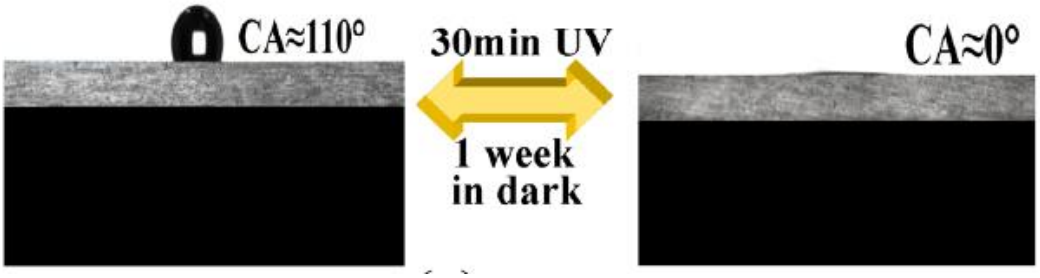

Figure 2.5 Water contact angle before and after UV irradiation. [87]

2.2 Enhancement of functionalized biointerfaces by nanopatterning

Having the appropriate surface properties of biointerfaces, mainly surface topography and chemistry, are important in regulating the protein affinity and conformation during its immobilization on the surface. In terms of topography, different types of protein are influenced by surface topography to different extents, such as feature sizes and surface roughness. [94,95] For example, both bovine serum albumin (BSA), a globular protein, and bovine fibrinogen (Fg), a rod-like protein, prefer to adsorb to a more curved surface or a smaller substrate size. However, in terms of protein conformation, BSA becomes more disordered when adsorbing onto a larger surface, while Fg shows the opposite trend. BSA is found to retain its globular shape when bounded to a more curved surface, but deforms when bounded to a flat surface. On the other hand, Fg retains its rod-like shape when bounded to a flat surface, but possibly bends around the surface and deforms on a curved surface. [96] A schematic of such dependence of BSA and Fg on surface topography is shown in **Figure 2.6**. Therefore, by controlling the surface topography it is possible to control protein conformation on the surface. It has also been shown that a roughened tantalum oxide surface with feature dimensions of 12 – 44 nm enhances adsorption of fibronectin by up to 14 ± 5%, but at the same time its conformation on the surface has also been changed. [97] Another example of the influence of topography on protein conformation and adsorption is the increased

unfolding of vitronectin on a roughened alumina surface. It was found that when the average surface roughness was increased from 16 nm to 32 nm, the concentration of vitronectin adsorbed was increased by 30%. Moreover, the degree of unfolding of vitronectin was found to increase when the surface roughness was increased, indicated by an increase in the ratio of the number of functional groups of vitronectin being exposed to the surrounding medium to the number of groups packed inside the protein itself from 0.86 to 1.15, measured by Raman spectroscopy. [98] Protein adsorption can also be inhibited if nanostructures are engineered on a hydrophobic surface, because the nanostructures limit the surface wetting by protein solution to occur only on top of the structures, thus decreasing the surface area available, due to the Wenzel-Cassie wetting effect. Combined with surface chemistry modification, a protein-resistant surface can be engineered for antifouling applications. [99] On the other hand, if the surface is initially hydrophilic instead, the presence of nanostructures further enhances wetting of the surface, and thus provides a larger surface area for protein adsorption. [99] This is advantageous for biosensor applications, in which a large surface area is desired to increase the quantities of adsorbed target molecules to increase sensitivity. [99,100] In addition, it is shown that proteins tend to accumulate within the troughs of the nanostructures so they can become supersaturated and stack onto each other and form multiple protein layers on the surface. The uptake amount can be increased by as much as 600% by just increasing the surface roughness by 100%. [101]

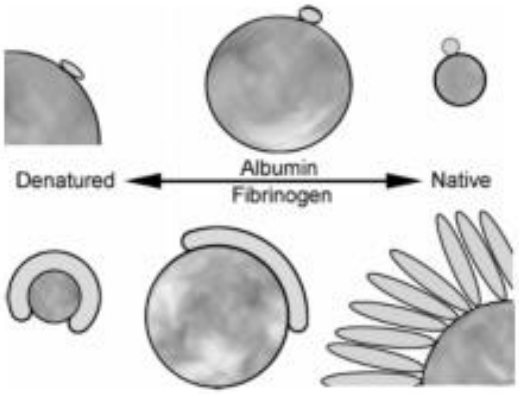

Figure 2.6 Influence of surface curvature to albumin and fibrinogen conformation on surfaces. [96]

In terms of chemistry, the surface chemistry can be tailored by adding certain functional groups, such as hydroxyl (OH), carboxyl (COOH) and amine (NH_2) groups, to enable adhesion of certain types of proteins while resisting others. [102] For example, Martins et al. has shown that by controlling the amount of hydroxyl groups (OH^-) on the biomaterial surface they were able to increase the adsorption of albumin while minimizing the adsorption of fibrinogen. They were able to control the chemistry by controlling the ratio of the two precursor solutions that form the interface for protein adsorption, one containing OH^- functional groups and one containing hydrocarbon groups only. The researchers explained that [103] In addition, Liu et al. have found that activation of a surface with OH^- groups enables preferential adsorption of immunoglobulin G (IgG) over serum. [104] Moreover, Majumder et al. demonstrated that creating oxygen vacancies on TiO_2 surface improves its biocompatibility with plasmid DNA. The researchers believed these oxygen vacancies promotes electron transfer from the DNA phosphate backbone to the surface. Together with the induced nanostructures and surface roughness, DNA immobilization onto the surface is improved. [93] It is also shown that addition of an OH^- group on a TiO_2 surface using O_2 plasma for a sufficiently long duration increases the amount of the antibody of prostate-specific antigen (anti-PSA) immobilized onto the surface significantly. The effect is shown in **Figure 2.7**. [105]

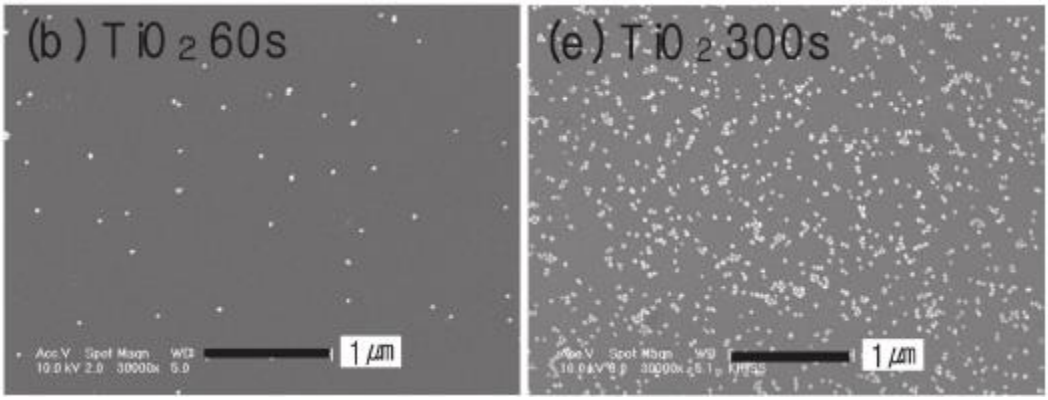

Figure 2.7 Amount of anti-PSA adsorbed on TiO_2 surface after surface exposure to O_2 plasma for 60 and 300s. White dots represent the presence of anti-PSA. [105]

The tailoring of surface topography and chemistry presented above can be realized effectively by low-temperature plasma and ion beam processing. [50,106,107,108] Plasma and ion beam processing enables tunable surface modification and patterning of biointerfaces with a wide variety of geometries and compositions. It also enables binding functional groups chemically onto a non-reactive surface. [109] For example, Chu has reported the use of silver (Ag) plasma to implant silver into the surface of titanium (Ti) implants to improve its antimicrobial properties, by immersing the Ti substrate into the plasma, a technique known as plasma immersion ion implantation and deposition (PIII&D). Ag atoms implanted into the Ti substrate nucleate and forms Ag nanoparticles, and these Ag nanoparticles are able to inhibit the growth of *S. aureus* bacteria on the surface significantly, as shown in **Figure 2.8**. [106] Plasma is also used to create different functional groups on biointerfaces for immobilization of various biomolecules. For example, NH_2, COOH and OH groups can be created with the use of ammonia plasma, CO_2 plasma and plasma polymerization utilizing ethanol or methanol monomers respectively. NH_2, COOH and OH groups are found to be useful for immobilization of various biomolecules, for example DNA, collagen and glucose isomerase respectively. [109] In addition, in **Chapter 2.1** it is already presented the versatility of ion-beam nanopatterning in inducing various nanostructures,

modifying surface roughness, chemistry as well as wettability. Therefore, low-temperature plasma processing and ion-beam nanopatterning have the potential as efficient techniques for improving the surface properties of biointerfaces.

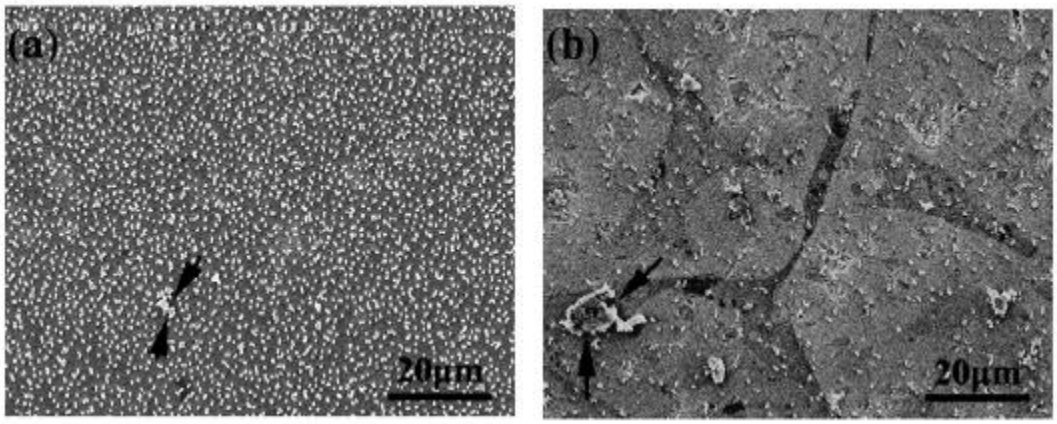

Figure 2.8 SEM images of S. aureus cultivated on Ti surfaces (a) without and (b) with 30 min Ag-PIII treatment. White dots represent the bacteria. [106]

CHAPTER 3: SCOPE OF RESEARCH

3.1 Research aim

This research aims at examining several aspects of TiO_2 ion irradiation previous research discussed in the first two chapters that have not investigated yet. First, there lacks a systematic study of how different irradiation parameters can influence PC biosensors surface differently. One immediate advantage of having a systematic study is that different interesting nanostructures, such as ripples, nanorods, nanoislands and so on, that can be grown on a TiO_2 surface may be discovered, as well as potential surface chemistry changes due to different ions. A long term advantage is that the irradiation processes can be tailored to different biosensing application so that nanostructured surfaces can be tailored to specific target analytes. For example, PC biosensors for different sensing applications can be first manufactured with the same recipe. Post-processing using irradiation can then be done with the conditions being tailored to specific applications.

In addition, most irradiation work deals with bulk TiO_2 crystal or thin film with a flat uniform surface only. In many cases, irradiation parameters used for bulk crystals cannot be applied to thin films with only around 100 nm thickness, the reason being parameters for bulk crystals usually do not consider the amount of materials removed from the surface, but for thin films that could cause the entire film to be removed. Moreover, the rate of sputtering is dependent on the surface curvature, and any large structures on the surface can have a shadowing effect causing the sputtering rate of the lower surface to be slower than that of the upper surface of the PC. The non-uniform sputtering may result in variations of surface topography among the upper, lower surfaces and the grating edges, as well as the PC's ability to resonate and reflect light.

The major purpose of TiO_2 irradiation in this research is to increase the surface area available for adsorption of target analytes, and hence increase the biosensor sensitivity. Cunningham et al. have demonstrated that by growing nanorods via glancing angle deposition (GLAD) on the PC sensor surface, the surface area, and hence sensor sensitivity, has increased by up to 4 times, depending on the size of the target analytes. [100] A SEM micrograph of the modified surface by Prof. Cunningham is shown in **Figure 3.1**. Using GLAD, the researchers have engineered TiO_2 nanorods with a diameter of ~ 30 nm, a height of ~85 nm, a tilt angle of ~ 35^o towards the deposition flux, and a spacing of ~ 15 between nanorods on the PC sensor surface with an as-deposited TiO_2 film, resulting an increase in surface area of ~ 4x. The researchers have used the nanorod-coated sensor in a protein adhesion assay involving proteins of different sizes. In their assay, a layer of amine polymer was first adsorbed onto the sensor surface to provide amine groups for subsequent protein adsorption. Glutaraldehyde (GA), streptavidin (SA) and biotin were then attached to the surface consecutively in that order. They have observed a ~ 4.30x, ~2.11x and ~2.07x increase in the amount of GA, SA and biotin adsorbed on the surface respectively. They have attributed the difference in such an increase to the difference in protein sizes, with SA being larger than GA. Biotin, while being the smallest, showed an increase of around the same magnitude as SA, simply because the amount of SA on the surface limits that of biotin that can link to the surface. This indicates while an increase in surface area due to nanostructures is beneficial in promoting a higher amount of target adsorption onto the sensor surface, the size and spacing of these structures have a differing impact to proteins of different sizes. Therefore, there is a need of a technique that can control the size and spacing of nanostructures. However, GLAD has the disadvantage of a low controllability of such self-assembled deposition process. To increase the variety of the size, shape and spacing of nanostructures, it is necessary to overcome the

thermodynamic constraints by inducing a self-organization process on the surface, as explained in the previous section. Ion-beam irradiation has already been shown to have the potential to achieve such goal while keeping the experimental procedures fast and simple. Therefore, this research aims at inducing nanostructures which can increase the surface area to the same magnitude as that achieved by Cunningham et al.

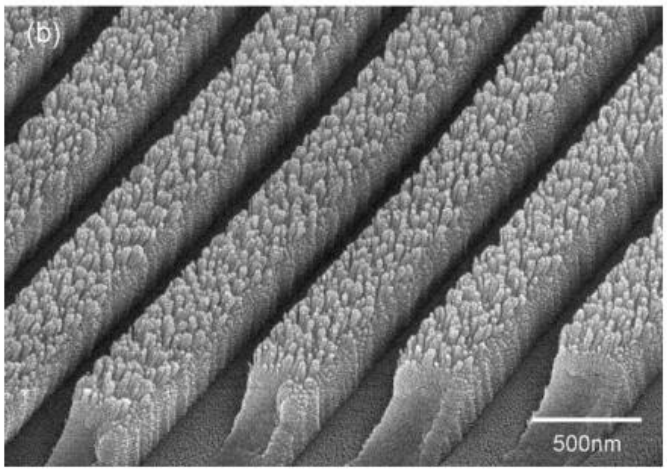

Figure 3.1 SEM micrograph of PC sensor modified by GLAD. [100]

3.2 Research hypothesis

Based on these research goals, five hypotheses have been formulated:

1. Ion irradiation will induce different topography variations independent of surface chemistry as a function of: ion species, energy, angle of incidence, orientation with respect to the diffraction gratings, and fluence.
2. Ion-beam-induced topography changes on thin films will be affected by the non-uniformity of the pre-existing surface structures of the substrate.

3. Ion irradiation will induce surface chemistry changes depending on the ion beam parameters and the reactivity of ion species. For example, it is hypothesized that Ar^+ ions will not cause chemistry changes but O_2^+ ions will due to Ar^+ being inert and O_2^+ being reactive in nature.
4. Ion irradiation will induce changes in the optical response of the photonic crystal, due to potential modification of the surface topography and film properties.
5. Ion-induced nanotopography will increase surface area and improve biosensor sensitivity up to the magnitude achieved by GLAD (4 times as stated in **Chapter 3.1**) or better.

CHAPTER 4: EXPERIMENTAL METHODS

4.1 Sample preparation

In this experiment, a prefabricated PC sensor provided by Prof. Cunningham's group was used. Its structure with the dimensions is shown in **Figure 4.1**. The parameters describing the dimensions are grating wavelength λ, width of the ridges w, and thickness of the TiO_2 film on the ridges t_1, sidewalls t_2, and trenches t_3. The sensor was fabricated using a nanoreplica molding method. The details of such method were described in [110], although the material of the film was different. In brief, the grating structures with the desired dimensions were patterned onto a silicon wafer using deep-UV lithography and reactive ion etching. Then the pattern was transferred to a large sheet made of polymer by pressing against the silicon mold with a thin layer of liquid epoxy in between. Afterwards, the liquid epoxy was solidified by UV-curing, and since it preferentially attached to the polymer, it was peeled away from the silicon mold. Lastly, a thin layer of TiO_2 was sputter-coated onto the epoxy surface. The epoxy substrate has a low refractive index of n=1.475, while the TiO_2 thin film has a high refractive index of n = 2.25. [100] A small area of about 2 cm x 2 cm containing 1-4 sensor wells was cut away from the sensor sheet and cleaned with 2 cycles of acetone → isopropanol → ethanol → deionized water before each irradiation.

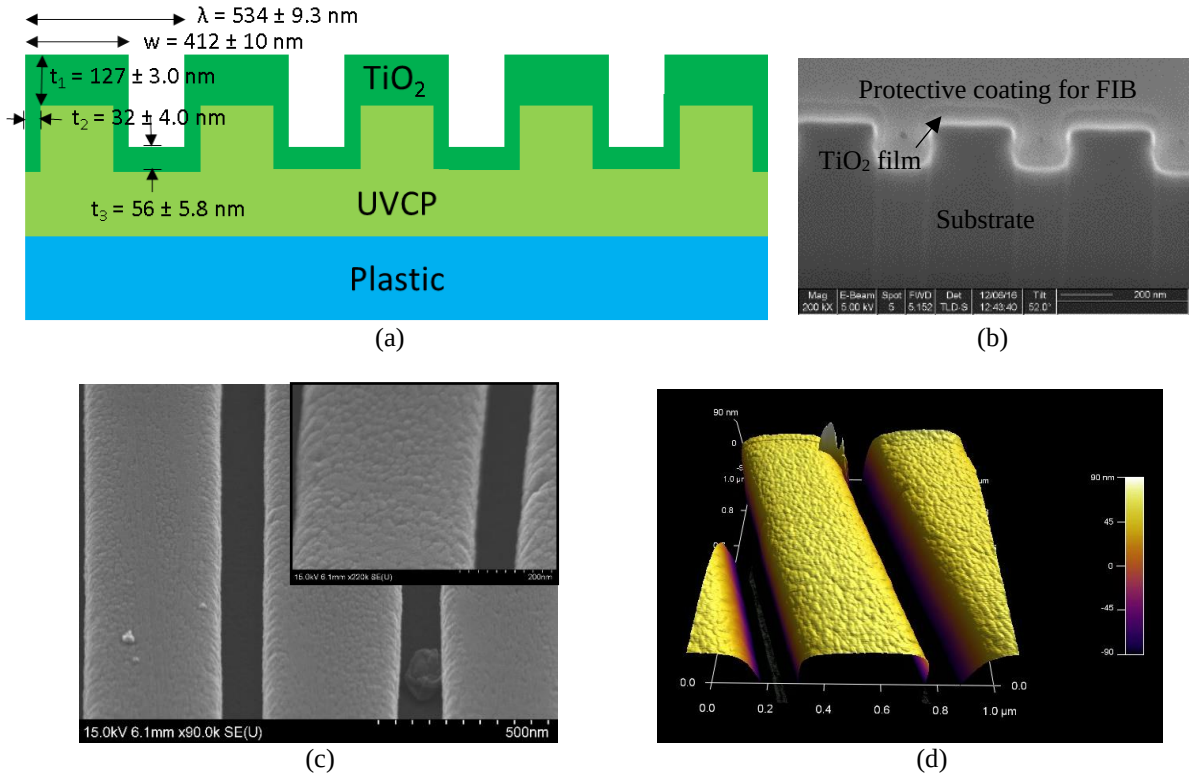

(a) (b)

(c) (d)

Figure 4.1 (a): Schematic of PC biosensor. The grating dimensions and film thickness were measured using cross-section scanning electron microscopy (SEM). (b): cross-section SEM micrograph of the sensor. (c)-(f): SEM micrographs and an AFM scans of the sensor surface at various magnifications.

4.2 Irradiation setup and parameters

Ion irradiation was carried out in Ion-Gas-Neutral Interactions with Surfaces (IGNIS) facility, an *in-situ* facility able to simultaneously carry out irradiation on surfaces under extreme conditions using a variety of particles such as ions, neutral atoms, electrons and photons, and surface characterizations such as x-ray photoelectron spectroscopy (XPS). A single ion beam from a microwave plasma source was used to irradiate the surface. The experimental setup is shown in **Figure 4.3**. The varying parameters were ion species, ion energy (E), angle of incidence (θ), beam orientation relative to sample grating structures (φ), and fluence (Φ). A range of these parameters conducted was shown in **Table 4.1**.

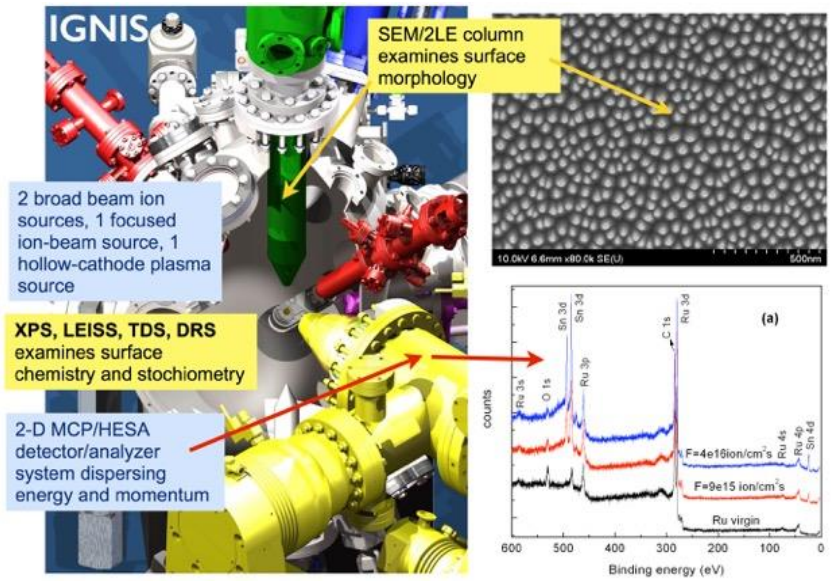

Figure 4.2 Left: A picture of the IGNIS facility. Right: Some results from experiments conducted in IGNIS.

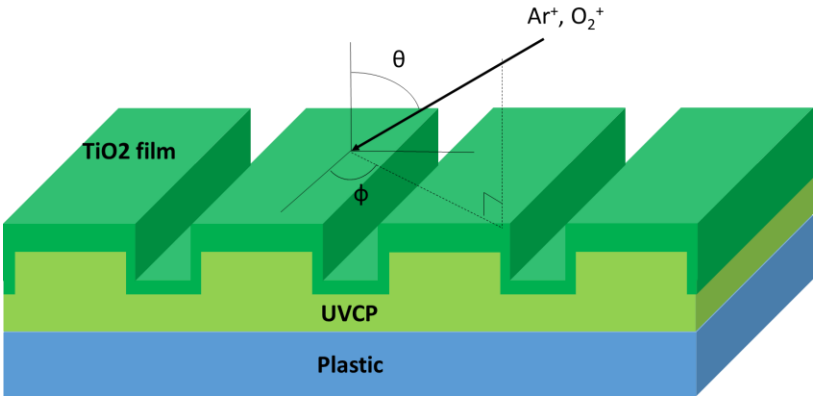

Figure 4.3 Experimental Setup. In the figure, θ is the angle of incidence relative to the surface normal, and is 0° when the beam is normally incident onto the surface. ϕ is the angle of beam orientation relative to the surface grating structures, and is 0° when the beam is perpendicular to the grating vector.

Table 4.1 Experimental parameters.

Parameters	Values
Ion species	Ar^+, O_2^+
Energy (E) [eV]	250 – 1000
Angle of incidence (θ) [°]	0° – 60°
Beam orientation (φ) [°]	0° – 90°
Fluence (Φ) [cm^{-2}]	5 x 10^{16}– 1 x 10^{18}

4.3 Sample characterization techniques

Several characterization techniques were used to characterize the surface topographical and chemical changes, and the electro-optical responses of the samples after ion irradiation. The surface topography was imaged by both scanning electron microscopy (SEM) and atomic force miscroscopy (AFM). Both were performed at the Frederick Seitz Materials Research Laboratory (MRL) at the University of Illinois Urbana-Champaign (UIUC). AFM images were processed and analyzed using the Asylum Research SPM software. SEM was performed using the Hitachi S-4800 High Resolution SEM instrument. It is utilized as a fast and straightforward technique to image the surface topography qualitatively, and to make sure the images obtained by AFM is accurate since images by AFM can contain false features due to errors and uncertainties, e.g. non-optimal tip geometry, surface contamination, external environmental changes causing image drift, and so on. [111] Samples were imaged at a 45^{o} angle relative to the normal so that the features on the surface could appear clearer. Moreover, the film thickness was quantitatively determined by creating a cross-section using a focused ion beam (FIB) and then imaged the cross-section by SEM. FIB and cross-section SEM were performed using FEI Dual Beam 235 FIB available in MRL. AFM was performed in tapping mode using the Asylum Research Cypher instrument. It is utilized as a very high resolution technique that can quantitatively determine feature size, height and surface roughness. Because of this purpose, only samples that show well-defined nanostructures under SEM were further characterized by AFM. The AFM tips used were purchased from BudgetSensors (Model Tap300AI-G). The tips were made of silicon with < 10 nm tip radius.

The surface chemistry was characterized using both *ex-situ* and *in-situ* XPS. *Ex-situ* XPS measurements were performed on all samples using either Kratos Axis ULTRA (Kratos) or

Physical Electronics PHI 5400 (PHI) in MRL in UIUC. In both instruments a monochromated Al Kα (1486.61 eV) x-ray source was used. The instrument was also equipped with a charge neutralizer to neutralize any surface charges induced by x-ray. *In-situ* XPS was performed on several chosen samples in IGNIS. A Mg Kα (1253.6 eV) x-ray source was used, but a charge neutralizer was not equipped. Instead, the sample stage was grounded. For *in-situ* XPS in IGNIS, first an XPS measurement was performed before any irradiation. Then the sample was cleaned using 1 keV Ar^+ at normal incidence for ~20 s, followed by another XPS measurement. A final *in-situ* XPS measurement was performed right after irradiation was complete, when the sample was still in vacuum. Afterwards, the sample was taken out and exposed to atmosphere for several days before an *ex-situ* XPS was performed in MRL. A survey spectrum, a Ti 2p, O 1s and C 1s core spectra, the core spectra corresponding to the most abundant and relevant elements on the surface, were obtained for each sample. 2 sweeps of survey and 10 sweeps of core spectra were taken and averaged. A survey spectrum gives information of the elements and possible contamination present in the first few nms of the sample surface. A core spectrum gives information of the chemical state of each element present in the survey spectrum. A deconvolution of each core spectrum is performed to determine the number of chemical states present in each element. Several constraints were employed during deconvolution to make sure the resultant deconvoluted peaks are physically significant. First, all peaks corresponding to the same elements should have approximately equal full-width at half-maximum (FWHM). An exception is the Ti $2p_{1/2}$ peak, which is found to be broader than the Ti $2p_{3/2}$ peak. [112] The other constraint is the area ratio between $2p_{1/2}$ and $2p_{3/2}$ peaks should always be 1:2. In addition, from the area under each core peak the relative atomic concentration of each chemical state of each major element can be calculated. XPS data were

analyzed using CasaXPS software. The binding energy scale was calibrated by calibrating the C1s peak to the reference value of adventitious carbon at 285 eV.

The optical property was studied by illuminating the samples with a TM polarized white light and measuring the transmission spectra. The instrument was built "in-house" by Prof. Cunningham's group. It consisted of a wide band LED light source, a linear polarizer, fibers, and a spectrometer. The sample was placed with the TiO_2 surface facing the light source and the grating vector perpendicular to the magnetic field of the TM polarized light. The setup is illustrated in **Figure 4.4 (a)**. When a sample was covered in water and inserted into the optical instrument, a sharp peak would be seen at a resonance wavelength which depends on the thickness of TiO_2 film and the number of biomolecules adsorbed onto the surface in biological tests. For the untreated sample the peak was located at 861 nm. Its transmission spectrum is shown in **Figure 4.4 (b)**.

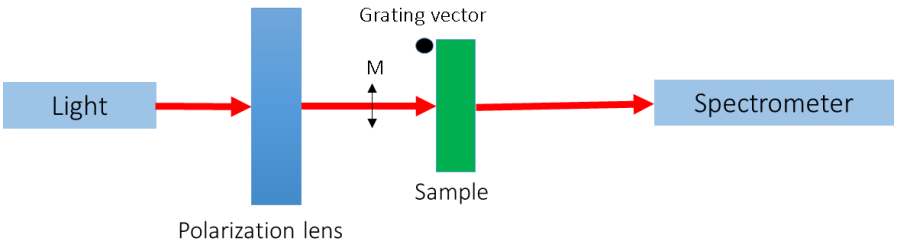

(a)

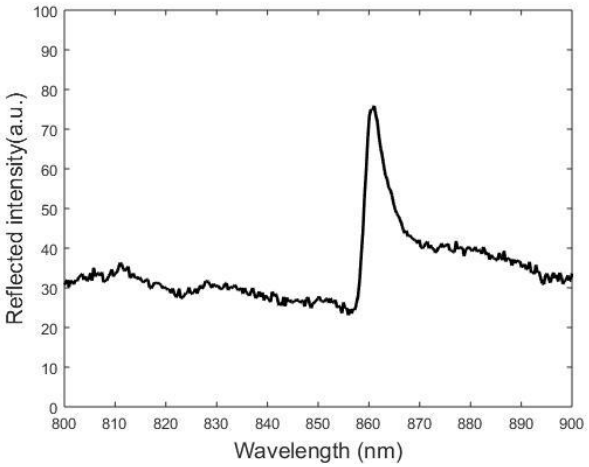

(b)

Figure 4.4 (a) Schematic of instrument setup for measuring transmission spectra. M denotes the direction of magnetic field of the TM polarized light. (b) Transmission spectrum of untreated sample. The resonant wavelength was located at 861 nm.

4.4 Protein adhesion study

A study of sensor sensitivity change due to nanopatterning was performed to demonstrate the application of the induced surface changes to label-free optical biosensing. The study consisted of attaching test proteins and linkers of different sizes both chemically and physically and compare the amount adsorbed onto several chosen sensor surfaces before and after irradiation. Two chemisorption and one physisorption procedures were used. The two chemisorption procedures to functionalize the surface with linkers and attach test proteins were adopted from [113] and [114] with modifications based on [105]. In the first chemisorption procedure, the linkers used were polyvinyl amine (PVA) and glutaraldehyde (GA), both large molecules for "amine functionalizing"

the surface and linking the proteins to the surface respectively. The test protein used was bovine serum albumin (BSA), a large globular protein. The sample surface was covered with 10% PVA solution in 1X phosphate buffer saline solution (PBS) at 25^{o}C for at least 4 hours. The surface was then washed three times with 1X PBS, followed by immersing in 25% GA solution in 1X PBS at 25^{o}C for at least 4 hours. The surface was then washed three times with 1X PBS again, followed by immersing in 40μL of 1 mg/mL BSA, diluted in 1X PBS, for at least overnight.

In the second chemisorption procedure, the linkers used were (3-aminopropyl)triethoxysilane (APTES) and poly(ethylene glycol)-succinimidyl valerate (PEG-SVA), both having similar functions as PVA and GA but with APTES being smaller than PVA. The test protein used was biotin, a small protein. The sample was fist cleaned with low power O_2 plasma for 15 mins to remove contaminants and activate the surface with OH^- groups for better adsorption of APTES. It was then immersed into 3% APTES solution in acetone for 1 hr, followed by curing at 110 C for 1 hr. Afterwards a drop of a mixture of 0.5% biotin-PEG-SVA and mPEG-SVA solution was placed onto the surface for 30 mins. The drop was made to be large enough to cover the entire surface. In the physisorption procedure, the samples were immersed in a 1% protein solution in 1x PBS for 30 mins. The protein used were BSA, a large protein, and Vitamin B12, which is a small one.

The amount of proteins immobilized on the surface was determined by comparing the PWV shift of the transmission spectrum before and after the experiment. An illustration of the PWV shift is shown in **Figure 4.5**. XPS was also performed on protein immobilized samples to verify the presence of proteins and linkers by observing the presence of N 1s and Si 2p and calculating their atomic percentages respectively.

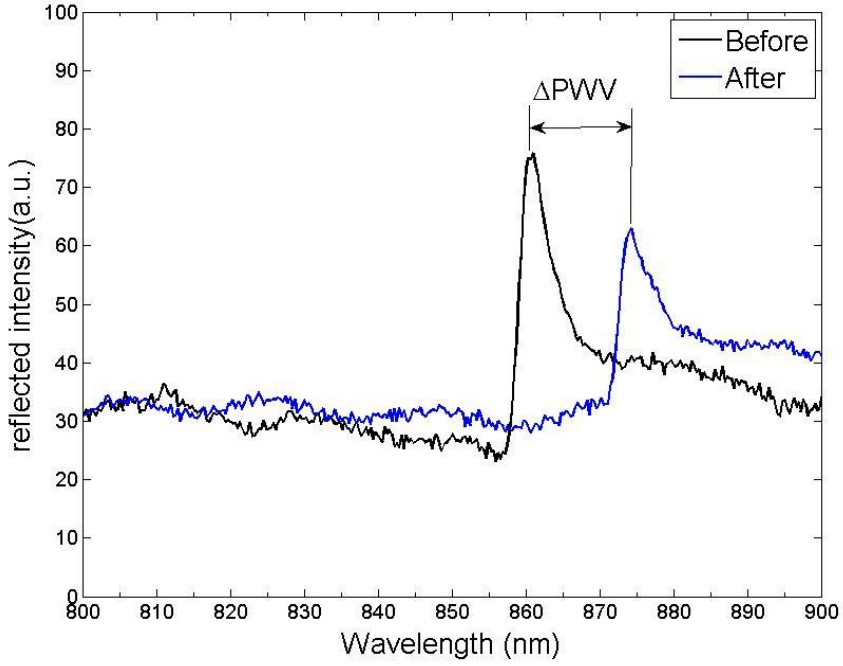

Figure 4.5 Example of PWV shift after biological test

4.5 Error Analysis

This section addresses errors encountered during ion irradiation and measurements with characterization techniques addressed above, and their propagation into the results shown in the following chapters. First of all, regarding the irradiation parameters, errors for E, θ, φ are mostly due to errors in reading from the angle measurements on the sample stage and the ion energy from the control of the plasma source. The error for Φ was the main contribution to the errors in irradiation conditions. During irradiation, it was observed that the ion current was usually changed by as much as around ± 8 μA at the end of irradiation, the magnitude depending on the duration of irradiation, with the longest duration being 140 mins (using an ion current of 19 μA, incident angle $\theta = 60^{o}$, and $\Phi = 5 \times 10^{17}$ cm^{-2} in O_2^+ irradiation). The measured ion current and Φ is related by:

$$\Phi = \Gamma t = \frac{It}{e}\cos\theta$$

where Γ is the ion flux [cm^{-2} s^{-1}], t is irradiation duration [sec], e is the electron charge assuming most ions were singly ionized, I is the ion current [A], and θ is the incident angle [°]. Assuming fluctuation of ion current was the major source of error, the error in Φ was therefore as much as $\Delta\Phi = \frac{(I_{inital,t_{max}} - I_{end,t_{max}})t_{max}}{e}\cos\theta = 2.1 \text{ x } 10^{17} \text{ cm}^{-2}$, where $I_{inital,t_{max}} = 19\ \mu A, I_{end,t_{max}} = 19 - 8 = 11\ \mu A$ are measured ion currents before (which was used to calculate the theoretical ion fluence the sample was exposed to) and after irradiation in the experiment with the longest duration (t_{max}=140 mins, initial ion current of 19 μA, incident angle θ = 60°, and Φ = 5 x 10^{17} cm^{-2} in O_2^+ irradiation.)

Next, there was measurement errors when measuring λ, w and film thicknesses from SEM images, and nanostructured ripple periodicity and amplitudes from AFM images. Three SEM and AFM images were recorded for each sample, and 4-5 measurements of each quantity were taken from each image. The measured values of each quantity reported in its respective plot were then the average of all the measurements, and the errors, indicated by the error bars in the plot, were then the standard deviation of all measured values. In addition, when calculating the increase in surface area due to the presence of nanostructured ripples, there were also errors propagated from the errors of periodicity and amplitudes measurements. The calculation of such error propagation will be presented in **Chapter 5.4** when the method of estimating the surface area is presented.

Regarding XPS results, there was errors arise from comparing photoelectron peak positions and measuring atomic percentages of elements present on the target surface. XPS has excellent

precision in measuring the binding energies of chemical bonding present on the target surface, presented by photoelectron peaks in a spectrum. However, the position of photoelectron peaks is affected not only by the nature of the bonding, but also slightly by the instruments used. In fact, for Ti 2p and O 1s peaks, different researchers have reported slightly varied peak positions, usually differed by about 0.3 eV, for each respective photoelectron peak. [115,116,117,118,119] Therefore, when comparing spectra obtained in Kratos and IGNIS, an error of about 0.3 eV has to be accounted into the difference in peak positions for Ti 2p and O 1s. In addition, when calculating the atomic percentage of elements present on the surface using CasaXPS, there was an error of about 10% according to the software manual.

Regarding transmission measurements, the major source of error in measuring the resonant peak position is due to the error in Φ during irradiation, which directly affects the film thickness remaining and hence the position of the resonant peak. The relationship between film thickness and resonant peak position is explained qualitatively in **Chapter 7**. However, it is difficult to estimate quantitatively the error of peak positions, because the quantitative relationship is unknown. However, it is known that the resolution of the light source used is 0.3 nm. Therefore, it is not able to distinguish the difference between samples if the samples reflect the light at wavelengths that differ by less than 0.3 nm.

Lastly, regarding the measurement of the amount of proteins adsorbed onto the surface, the major sources of errors were random error between adhesion tests and calculation error from the atomic percentage of nitrogen calculated using XPS. However, since only one sample from each condition was used for a specific protein adhesion assay due to limited number of samples, it is difficult to quantify the magnitude of the random error.

CHAPTER 5: SURFACE TOPOGRAPHY CHANGES DUE TO ION IRRADIATION

This chapter covers the surface topographical changes due to ion-beam irradiation under different parameters. The goal of this chapter is to address the first two and part of the last hypotheses made in **Chapter 3**: Ion irradiation will induce different topography variations independent of surface chemistry as a function of: ion species, energy, angle of incidence, orientation with respect to the diffraction gratings, and fluence; such topographical changes will be influenced by the non-uniformity of the pre-existing surface structures, and these nanostructures will increase the surface area up to the magnitude achieved by GLAD or better. Surface topographical changes are examined under SEM. AFM is also used for chosen samples that show nanostructures. Cross-section SEM is also performed on selected samples to measure the film thickness and observe the grating shape and size more carefully via a cross-section view. In this chapter, changes due to Ar^+ and O_2^+ irradiation will be discussed separately in their respective subsection. A comparison between them will be made in the end.

5.1 Ar^+ irradiation

Effects of varying energies, incident angle θ and fluence Φ are examined in the case of Ar^+ irradiation. First, effect of varying energies will be presented. The irradiation parameters were E = 250 – 1000 eV, $\theta = 0^o$, $\varphi = 0^o$, and $\Phi = 5 \times 10^{16}$ (LF) and 1×10^{18} (HF) cm^{-2}. Their respective SEM micrographs are presented in **Figure 5.1**. In general, no well-defined nanostructures can be seen on the surface. At LF at 500 eV, there was no observable changes to the surface. At 1000 eV, however, the surface seems to be smoothened when compared to the pre-irradiated surface. On the other hand, at HF, at both energies two entirely different topography can be seen on the grating

surface. Roughening, erosion, and defined nanostructures can be seen along the edges of the ridges, while the surface closer to the center of the ridges remained smooth and flat. The transition from the flat center to the nanostructured sides is abrupt. The effect is more significant at high energy. The periodic gratings maintained its 1D rectangular shape mostly as before, but towards the edges the surface seems slanted. This is shown in an AFM scan of the E = 1000 eV sample in **Figure 5.2**. The grating wavelengths (λ) and width of the ridges (w) are shown in **Figure 5.3**. At LF, these were not changed noticeably. At HF, λ also remained statistically unchanged. w has increased by ~30 nm compared to pre-irradiation, but the variation between energies is insignificant.

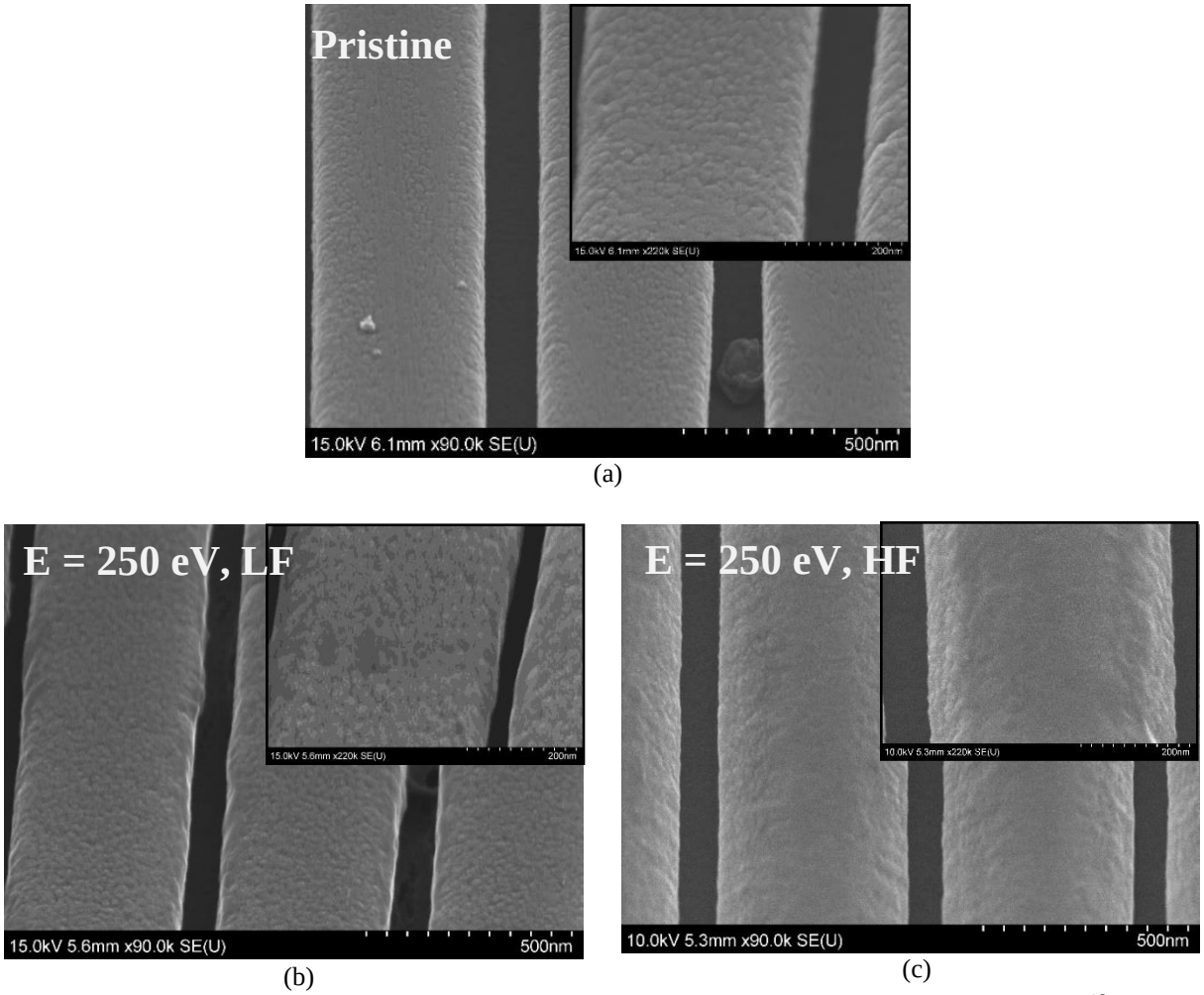

Figure 5.1 SEM micrographs after Ar^+ irradiation at E = 250 – 1000 eV, θ = 0°, φ = 0°, and Φ = 5 x 10^{16} (LF) and 1 x 10^{18} (HF) cm^{-2}. Insets are magnified images of the corresponding samples.

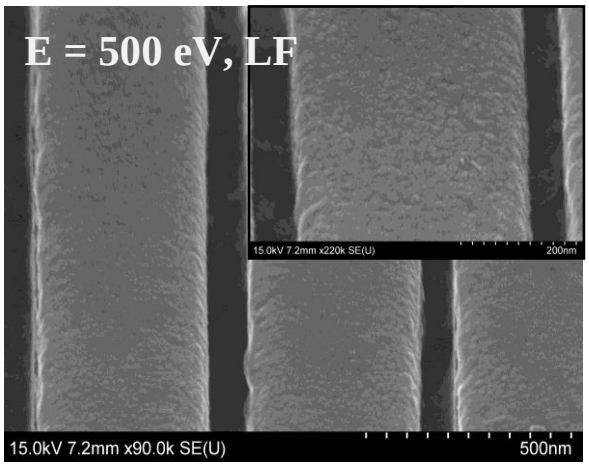

(d)

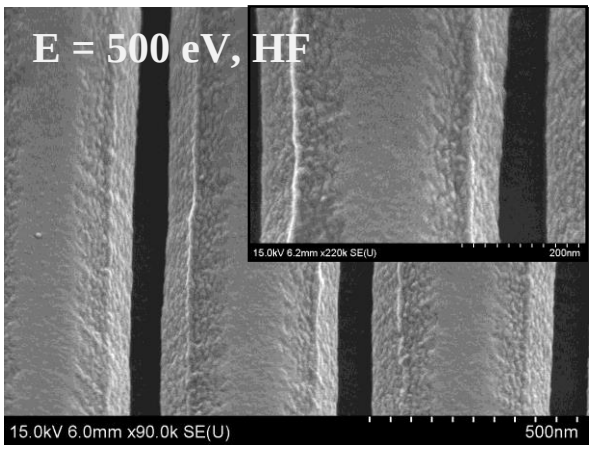

(e)

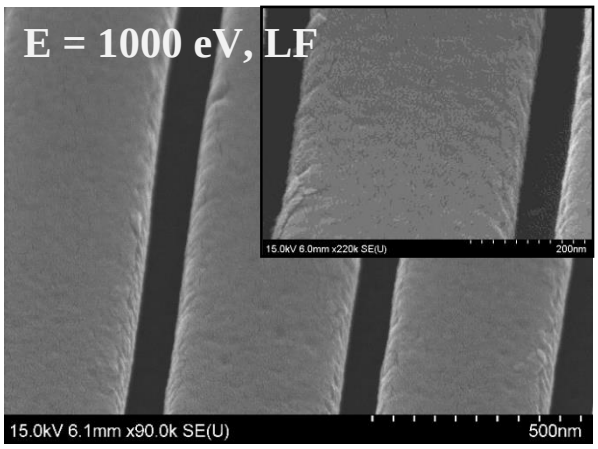

(f)

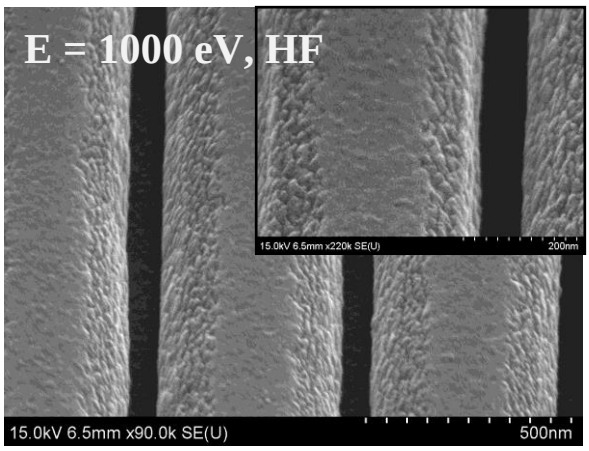

(g)

Figure 5.1 (cont.)

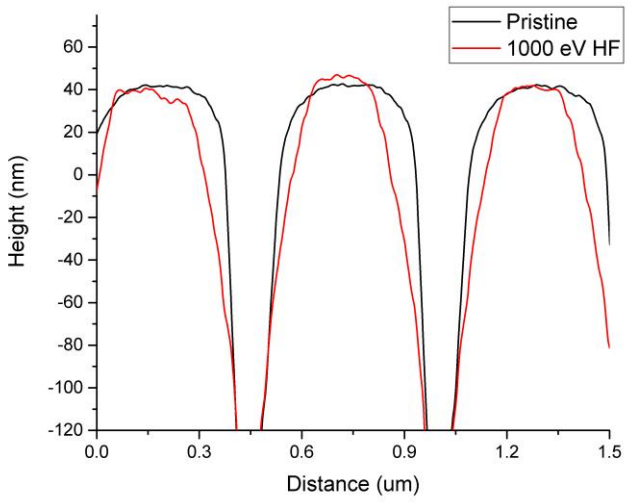

Figure 5.2 AFM line profiles of pristine and sample irradiated by Ar^{+} at E = 1000 eV, $\theta = 0^{o}$, $\varphi = 0^{o}$, and $\Phi = 1 \times 10^{18}$ (HF) cm^{-2}. It can be clearly seen that the almost right-angled edges are eroded and become a slanted surface after irradiation.

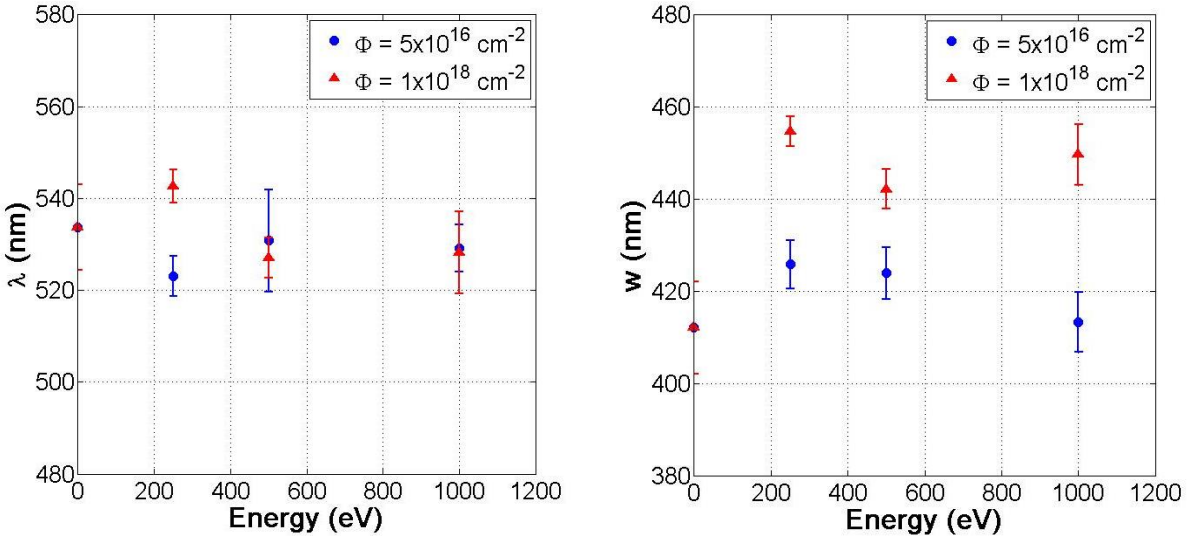

Figure 5.3 (a) λ and (b) w as a function of ion energy after Ar^+ irradiation at E = 250 – 1000 eV, θ = 0°, φ = 0°, and Φ = 5 x 10^{16} (LF) and 1 x 10^{18} (HF) cm^{-2}.

Next, the effect of varying incident angle θ is examined. The irradiation parameters were E = 500 eV, θ = 20° – 60°, φ = 0°, and Φ = 2.5 x 10^{17} cm^{-2}. Their respective SEM micrographs are shown in **Figure 5.4**. A transition from a flat surface to a nanostructured surface with well-defined nanostructures can be clearly seen when θ is increased from 20° to 60°. The grating wavelengths (λ) and width of the ridges (w) are shown in **Figure 5.5**. Same as before, no observable variations in λ exist. This is the same for w except there is a slight increase at θ = 60°. This could be caused by re-deposition again, but since the increase was very close to the error margin of the original value, it is more likely due to measurement error instead.

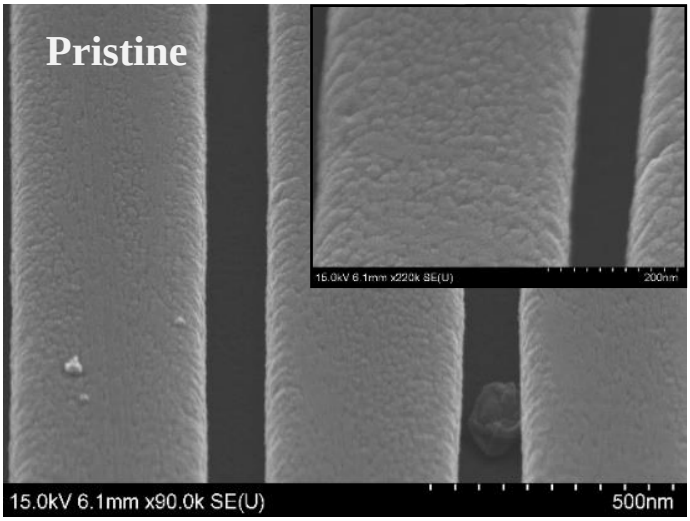

(a)

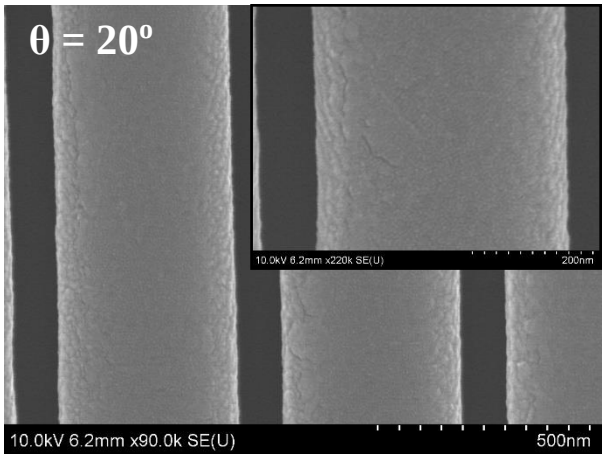

(b)

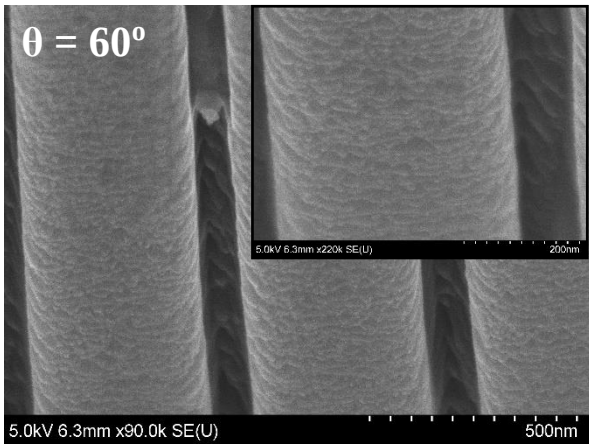

(c)

Figure 5.4 SEM micrographs of samples after Ar^+ irradiation at E = 500 eV, $\theta = 20^o - 60^o$, $\varphi = 0^o$, and $\Phi = 2.5 \times 10^{17}$ cm^{-2}. Insets are magnified images of the corresponding samples.

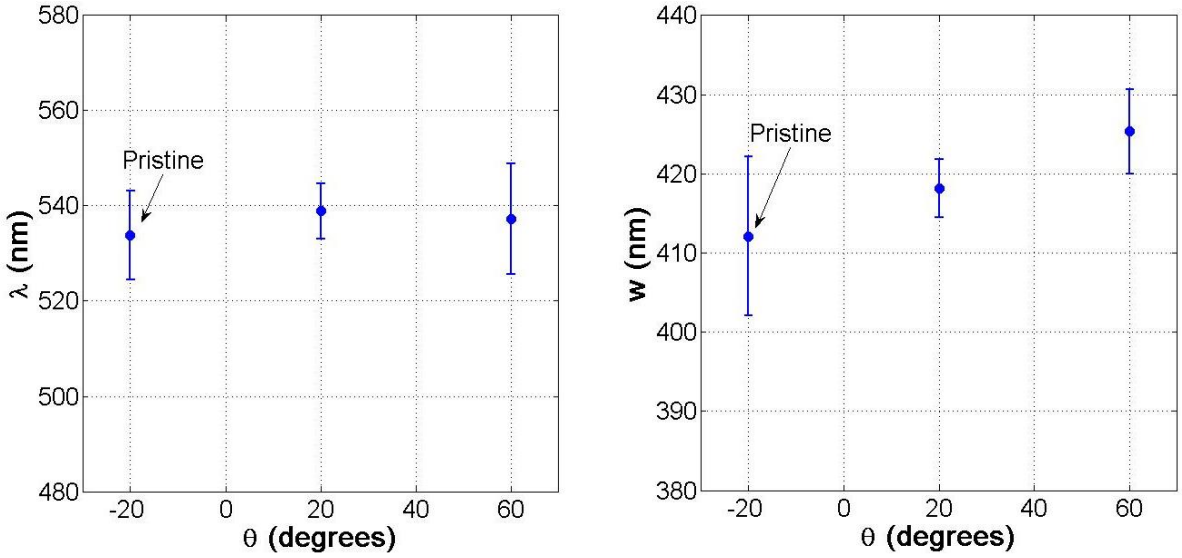

Figure 5.5 (a) λ and (b) w as a function of incident angle relative to the surface normal after Ar^+ irradiation at E = 500 eV, θ = 20° – 60°, φ = 0°, and Φ = 2.5 x 10^{17} cm^{-2}. The data points at θ = -20° refers to the pristine sample before irradiation.

Last, the effect of varying fluence is examined. Their respective SEM and AFM micrographs are shown in **Figure 5.6**. The irradiation parameters were E = 500 eV, θ = 60°, φ = 0°, and Φ = 0.5 x 10^{17} – 5.0 x 10^{17} cm^{-2}. At the lowest fluence of Φ = 5 x 10^{16} cm^{-2}, surface roughening can already be seen. When the fluence is increased to 1 x 10^{17} cm^{-2}, small ripple-like nanostructures appeared on the surface. At Φ = 2.5 x 10^{17} cm^{-2} fluence with Ar it has already been shown before that random but well-defined nano-islands appeared. At Φ = 3.0 x 10^{17} cm^{-2} the nano-islands appeared to coalesce in the direction perpendicular to the beam direction to form well-defined periodic ripples with a slightly varying periodicity and amplitude under different fluences. Some of these are estimated using AFM line profiles and plotted against fluence in **Figure 5.7 (a) - (b)**. From the plots there was clearly an increase in periodicity with increasing fluence, but the amplitude remained more or less unchanged. There were no significant topographical changes anymore at fluences higher than that, until Φ = 5.0 x 10^{17} cm^{-2}. At Φ = 5.0 x 10^{17} cm^{-2} a very different topography was seen. Large nano-platelet-like structures evolved on the grating surfaces. However,

XPS results, which will be discussed in **Chapter 6**, indicated a complete removal of TiO_2 film. This implies such topographical change was due to patterning of the polymer substrate instead, and thus an entirely different topography was resulted. The grating wavelengths (λ) and widths of the ridges (w) are plotted in **Figure 5.7 (c) – (d).** Same as before, although there were slight changes in λ and w at certain fluences, there was no noticeable trends of how such changes correlated to the fluence. There is a significant drop in λ in the case of Ar^+ irradiation at $\Phi = 5.0 \times 10^{17}$ cm^{-2}, but since a different material (polymer substrate) was sputtered instead, it is not very useful to compare its results to the rest of the samples. The 1D rectangular grating shapes also remained unchanged. Several samples are chosen for measurement of film thicknesses on both the ridges and trenches (t_1 and t_3). Results of t_1 results are shown in **Figure 5.7 (e).** Results of t_3 are not shown in a graph because apparently the film in the trenches have disappeared in all cases. Their cross-section SEM pictures are shown in **Figure 5.8**. The film thickness decreases linearly with fluence, and becomes zero at $\Phi = 5.0 \times 10^{17}$ cm^{-2}. Cross-section SEM pictures show the film and gratings has maintained their shapes, but the thickness of the sides towards the bottom starts to become thicker. The film in the trenches appear to have been removed as well.

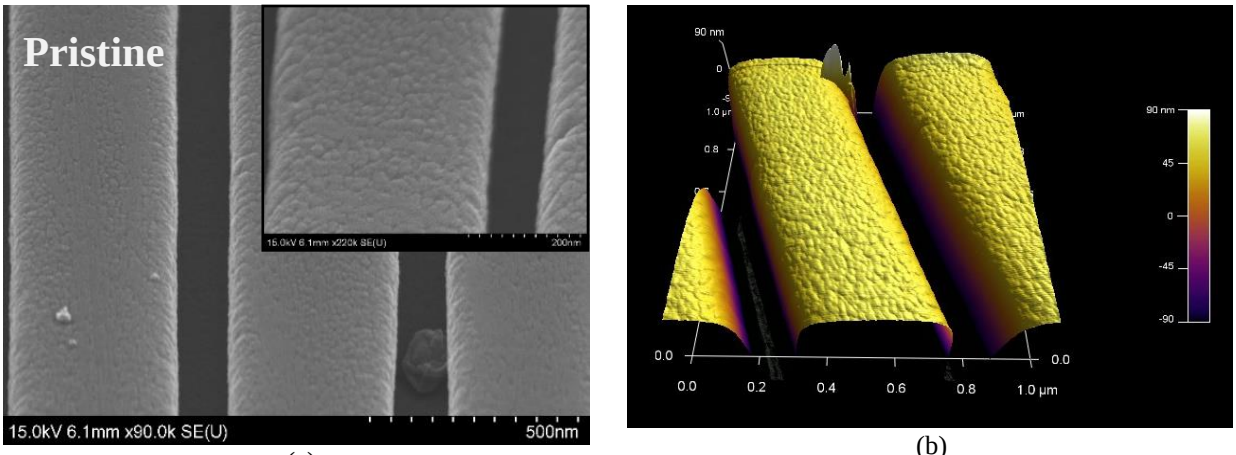

(a) (b)

Figure 5.6 SEM (left) and AFM (right) scans of samples after Ar^+ irradiation at E = 500 eV, θ = 60°, φ = 0°, and $\Phi = 5 \times 10^{16} – 5 \times 10^{17}$ cm^{-2}. Insets are magnified images of the corresponding samples.

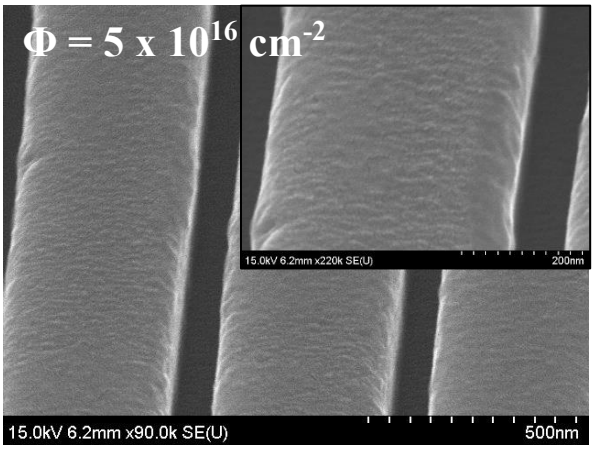

(c)

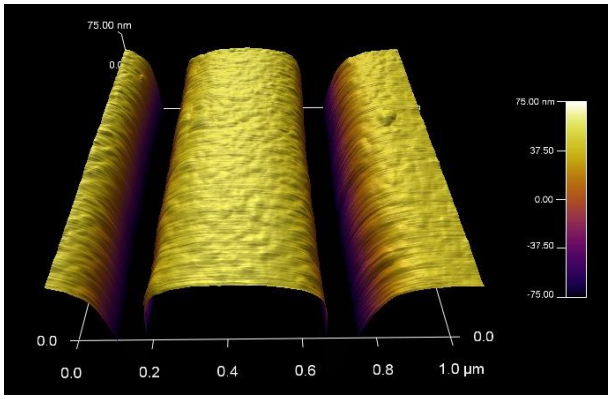

(d)

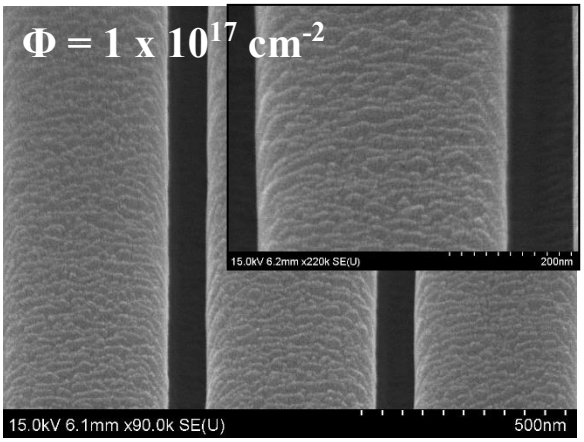

(e)

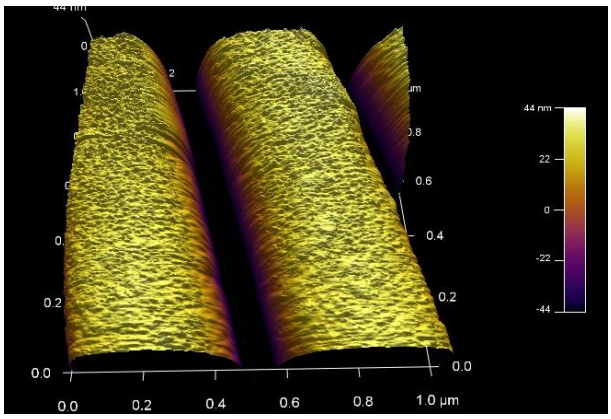

(f)

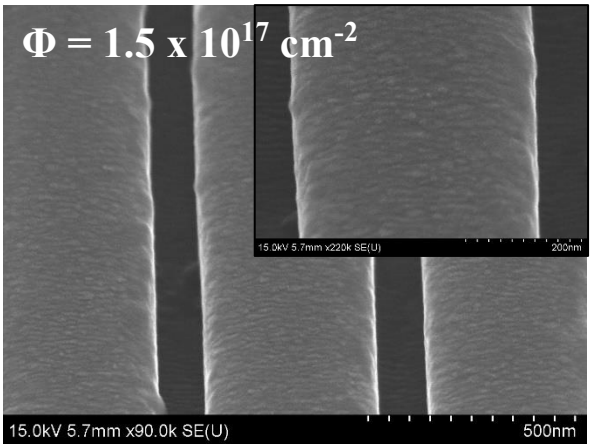

(g)

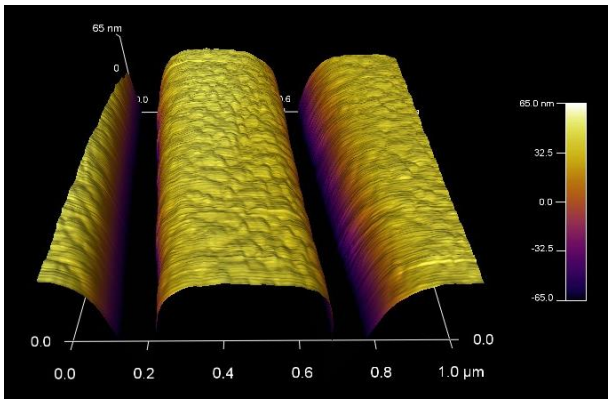

(h)

Figure 5.6 (cont.)

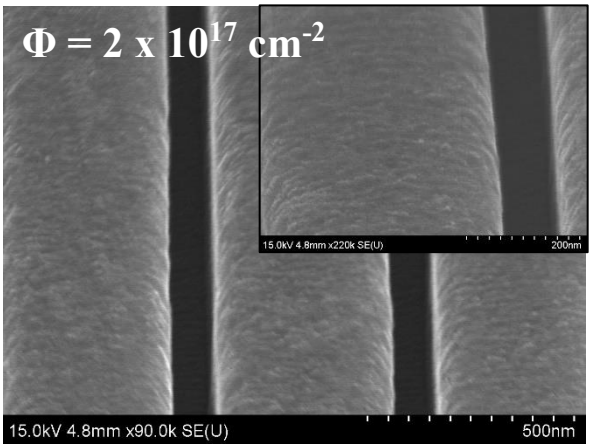

(i)

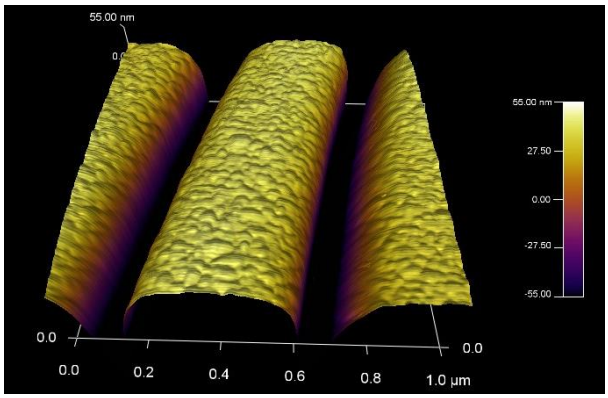

(j)

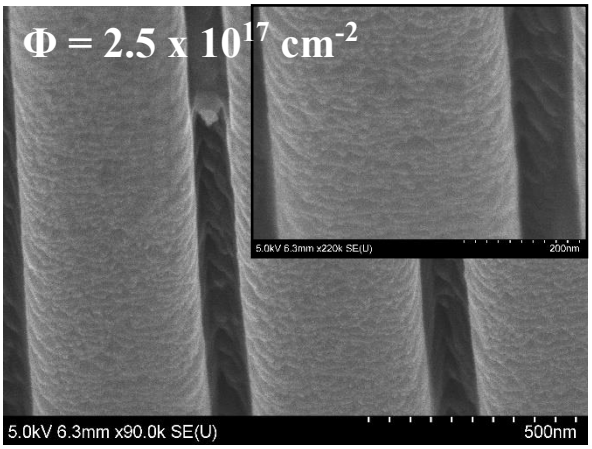

(k)

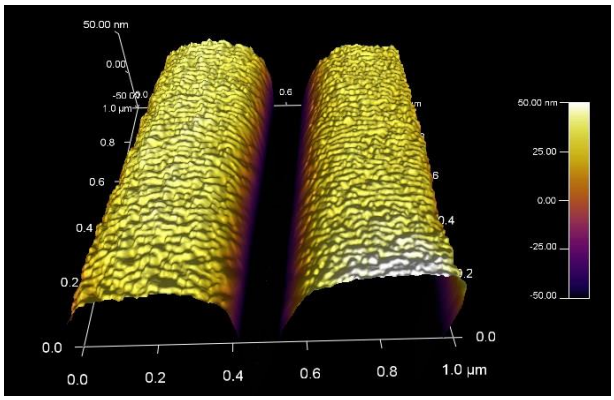

(l)

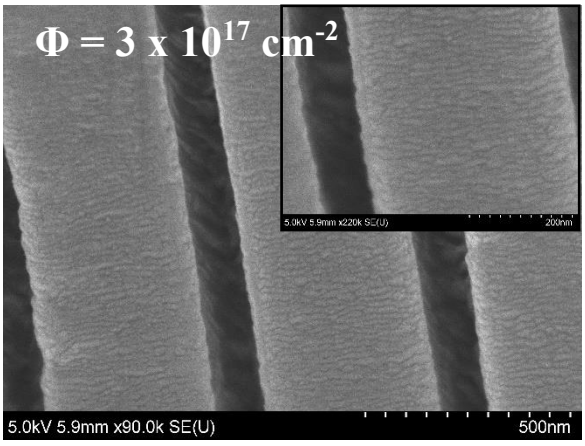

(m)

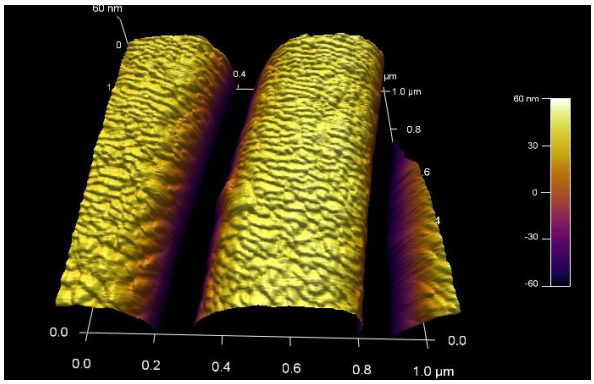

(n)

Figure 5.6 (cont.)

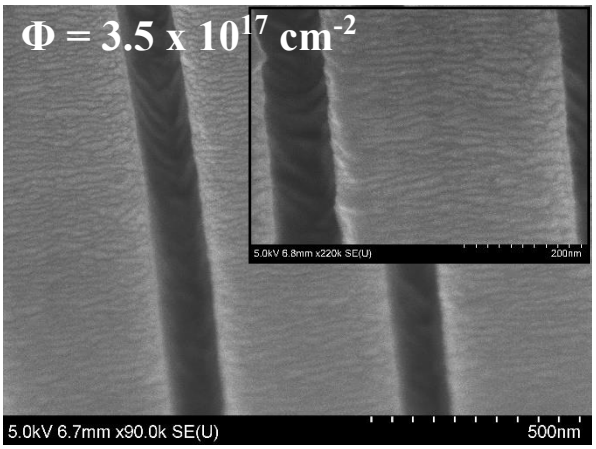

(o)

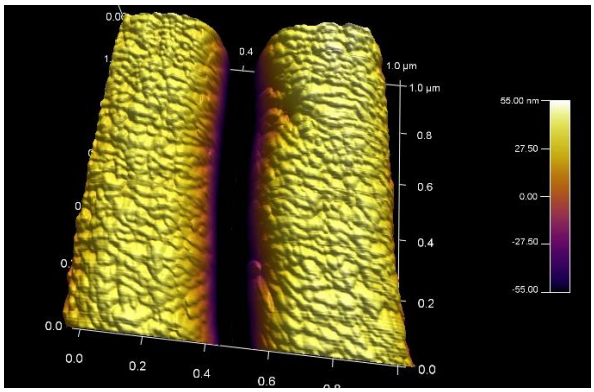

(p)

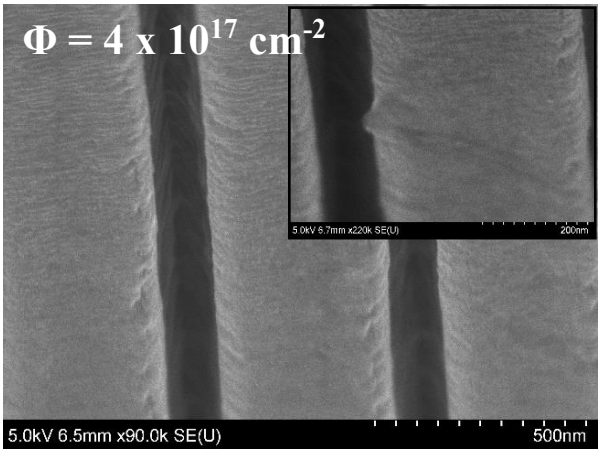

(q)

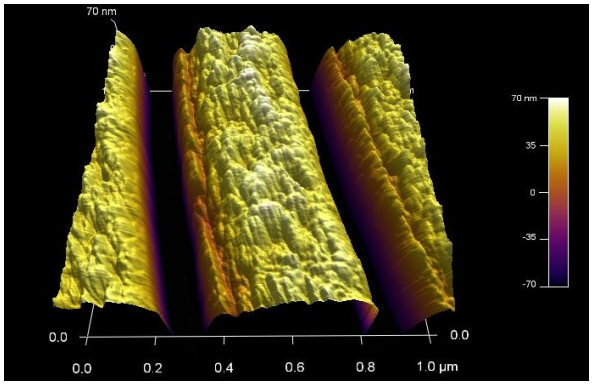

(r)

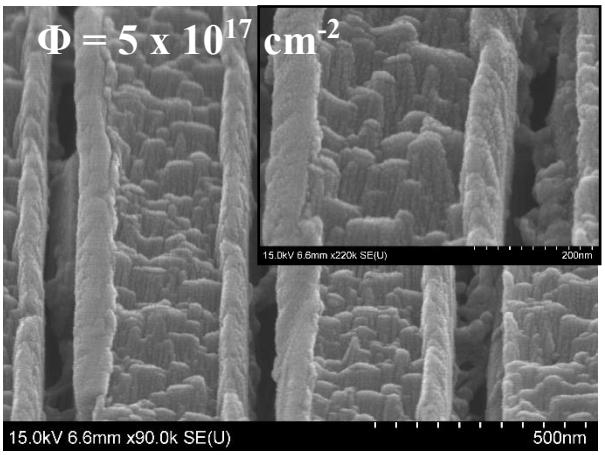

(s)

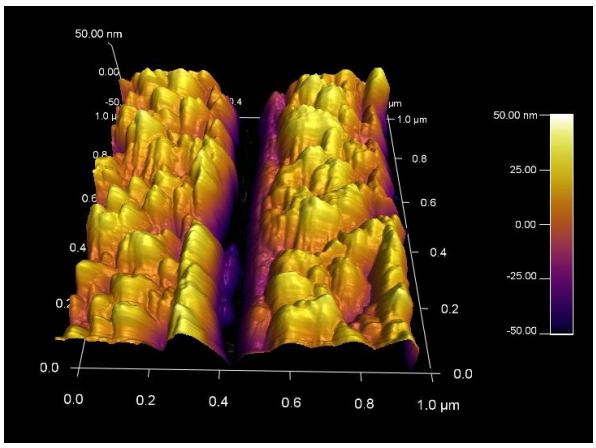

(t)

Figure 5.6 (cont.)

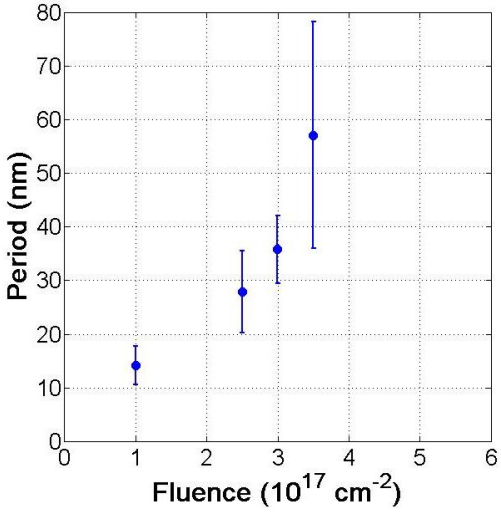

(a)

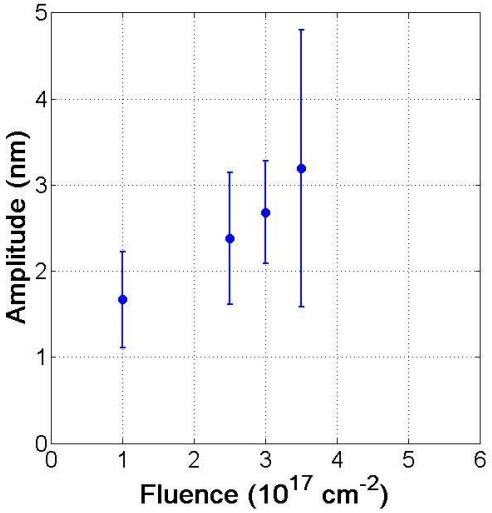

(b)

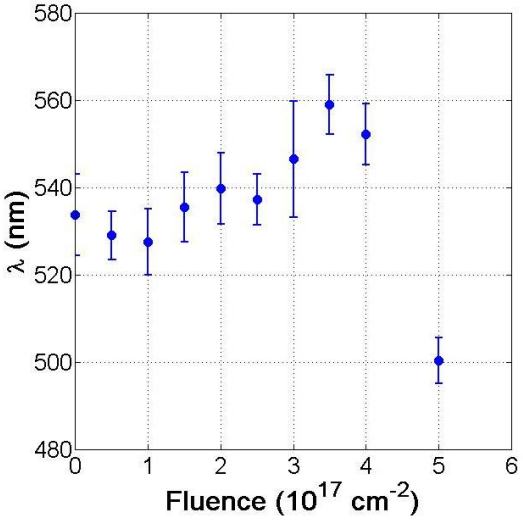

(c)

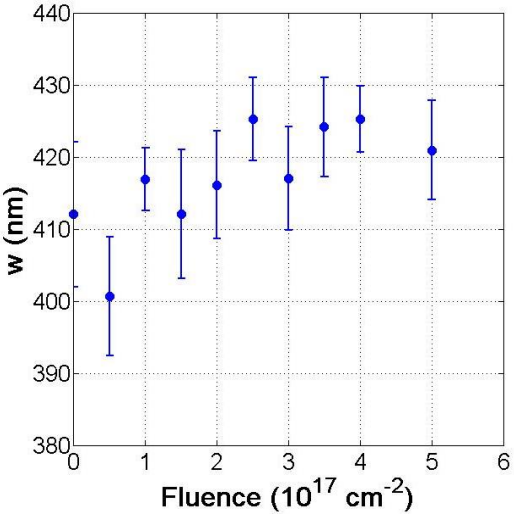

(d)

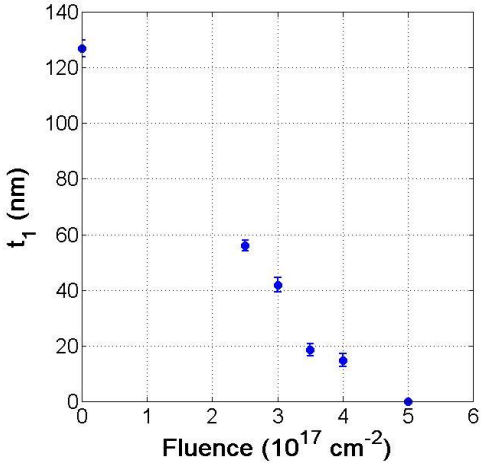

(e)

Figure 5.7 (a) λ, (b) w, (c) t_1, (d) ripple periodicity, and (e) ripple amplitude after Ar^+ irradiation at E = 500 eV, θ = 60°, φ = 0°, and Φ = 5 x 10^{16} – 5 x 10^{17} cm^{-2}.

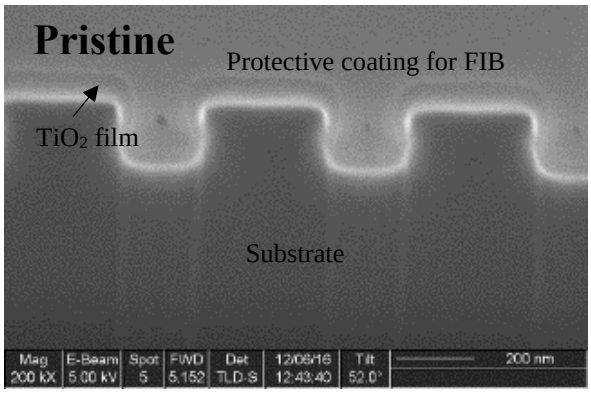

(a)

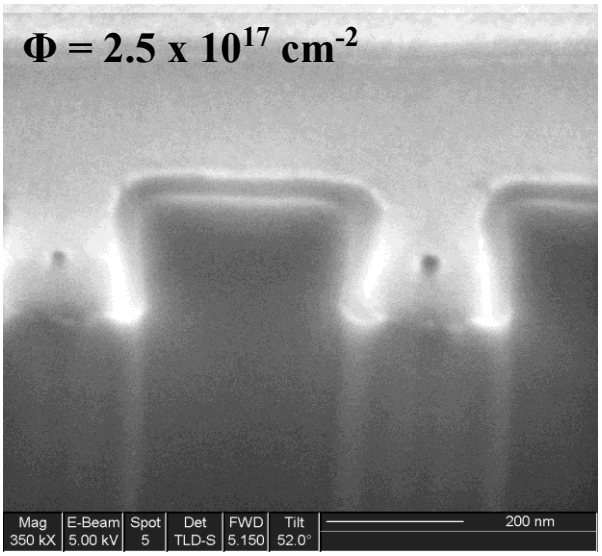

(a)

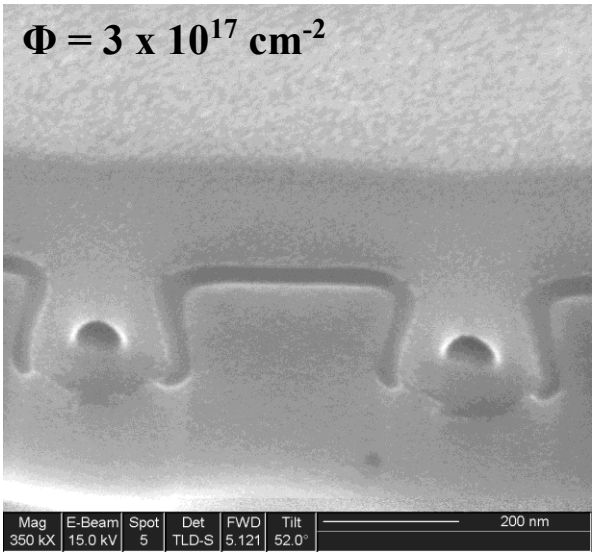

(b)

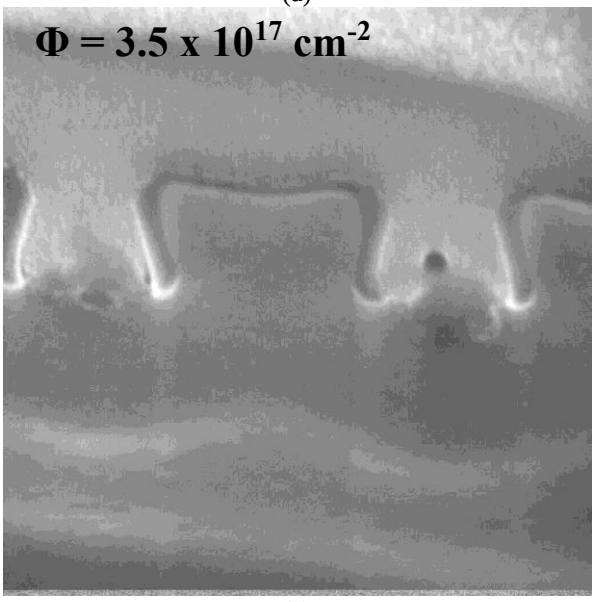

(c)

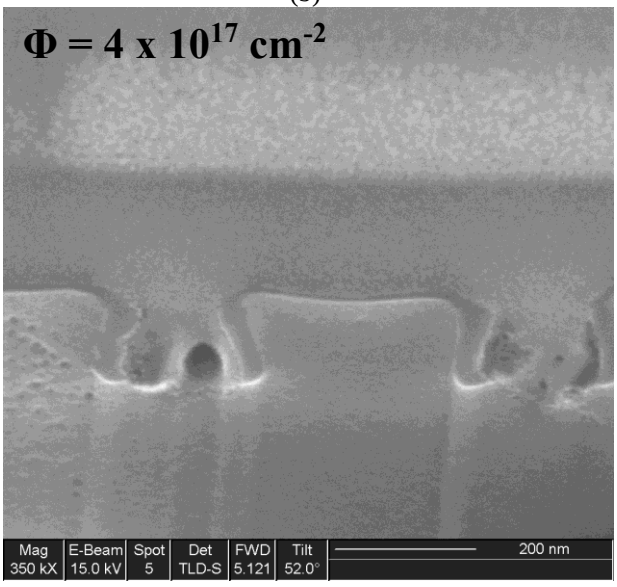

(d)

Figure 5.8 Cross-section SEM micrographs of samples after Ar^+ irradiation at E = 500 eV, θ = 60°, φ = 0°, and Φ = 2.55 x 10^{17} – 4 x 10^{17} cm^{-2}.

5.2 O_2^+ irradiation

Effects of varying incident angle θ, beam orientation φ and fluence Φ are examined in the case of O_2^+ irradiation. First, effect of varying θ will be presented. Their respective SEM micrographs are shown in **Figure 5.9**. The irradiation parameters were E = 500 eV, θ = 20º – 60º, φ = 0º, and Φ = 2.5 x 10^{17} cm^{-2}. A transition from a flat surface to a nanostructured surface with well-defined nanostructures can be clearly seen when θ is increased from 20º to 60º. The grating wavelengths (λ) and width of the ridges (w) are shown in **Figure 5.10**. Same as before, no observable variations in λ exist.

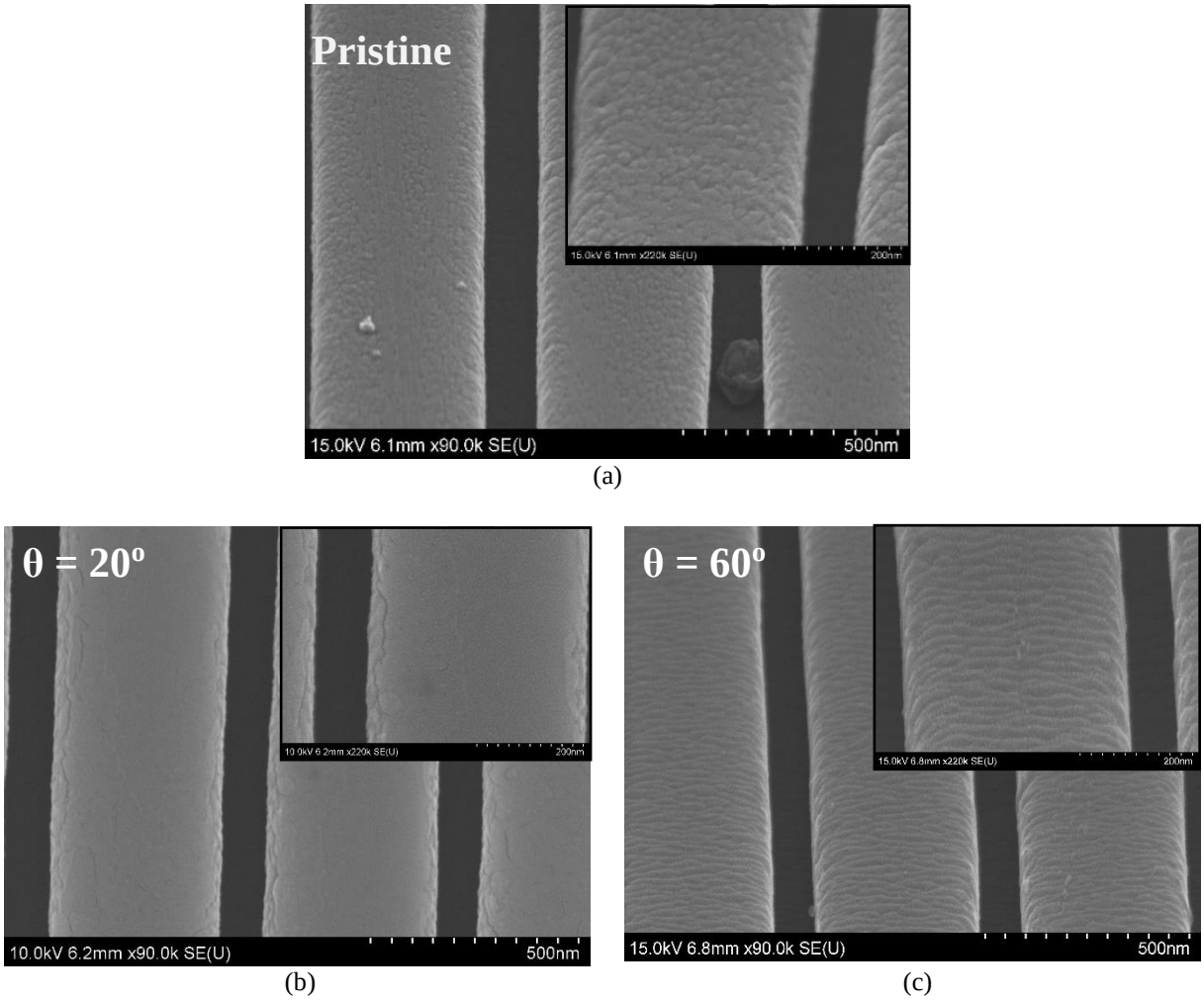

Figure 5.9 SEM micrographs of samples after O_2^+ irradiation at E = 500 eV, θ = 20º – 60º, φ = 0º, and Φ = 2.5 x 10^{17} cm^{-2}. Insets are magnified images of the corresponding samples.

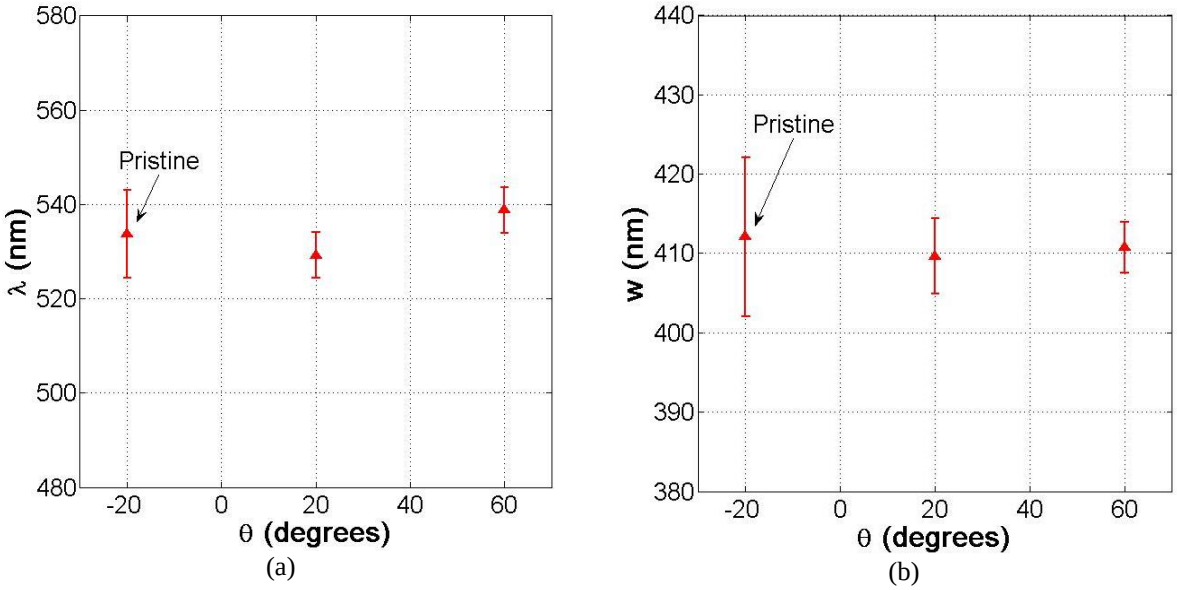

Figure 5.10 (a) λ and (b) w as a function of incident angle relative to the surface normal after O_2^+ irradiation at E = 500 eV, θ = 20° – 60°, φ = 0°, and Φ = 2.5 x 10^{17} cm^{-2}. The data points at θ = -20° refers to the pristine sample before irradiation.

Next, the effect of varying φ is examined. Their respective SEM micrographs are shown in **Figure 5.11**. The irradiation parameters were E = 500 eV, θ = 60°, φ = 0° – 90°, and Φ = 4.0 x 10^{17} cm^{-2}. The white arrows represent the direction of the beam. It is apparent that the ripple wave vector is parallel to the beam direction. The ripple direction changes according to the beam orientation. However, it can also be seen that the surface of the ridges may become slanted towards one side. In the micrographs for φ = 60° and φ = 90° one side of the ridges can be seen to be more blurred than the rest of the surface, implying that area is probably at a different height. AFM line profiles, shown in **Figure 5.12**, might be able to depict the slanted side of the ridges as well, although the changes cannot be very clearly seen. The grating wavelengths (λ) and width of the ridges (w) are shown in **Figure 5.11**. Same as before, no observable variations in λ exist. This is the same for w except there is a decrease at φ = 30°. The reason for the decrease in only this case is unknown.

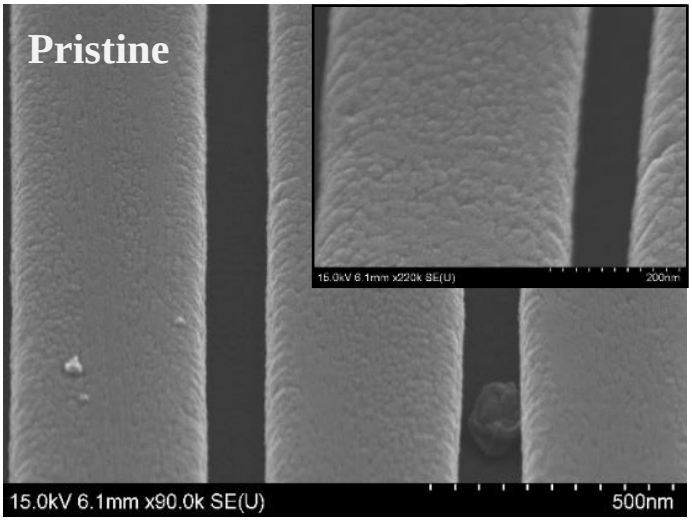

(a)

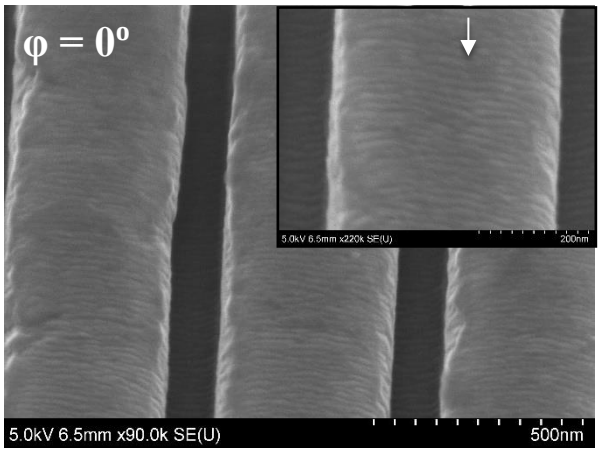

(b)

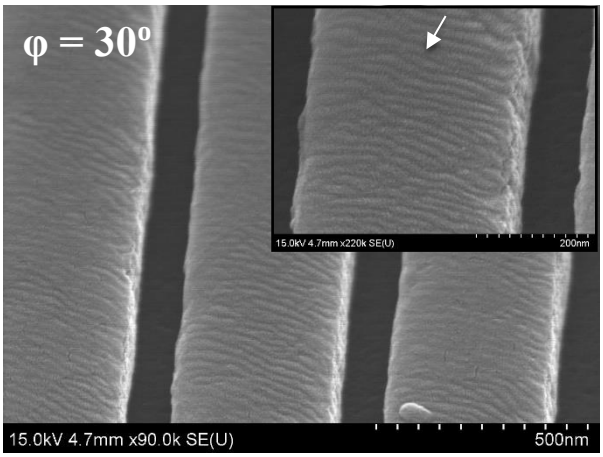

(c)

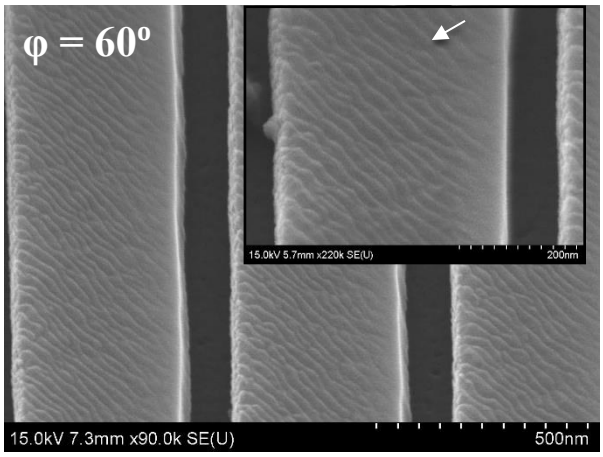

(d)

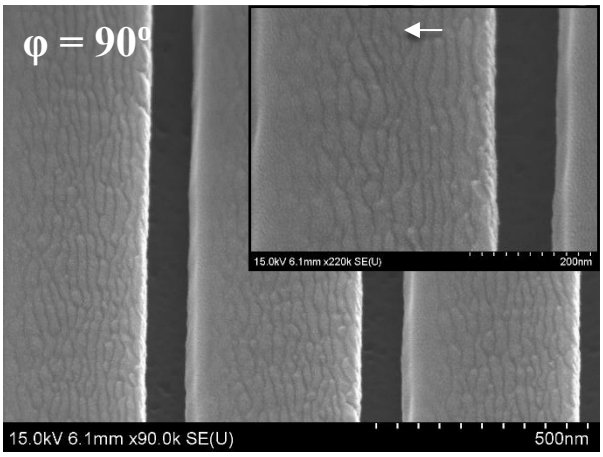

(e)

Figure 5.11 SEM micrographs of samples after O_2^+ irradiation at E = 500 eV, θ = 60°, φ = 0° – 90°, and Φ = 4.0 x 10^{17} cm^{-2}. Insets are magnified images of the corresponding samples. Arrows indicate the direction of the beam incident onto the sample.

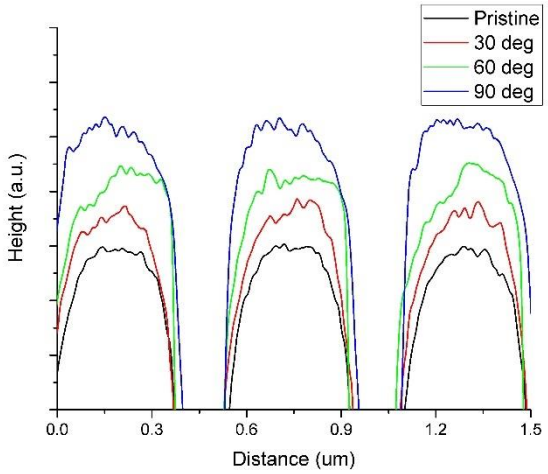

Figure 5.12 AFM line profiles of samples after O_2^+ irradiation at E = 500 eV, θ = 60°, φ = 0° – 90°, and Φ = 4.0 x 10^{17} cm^{-2}.

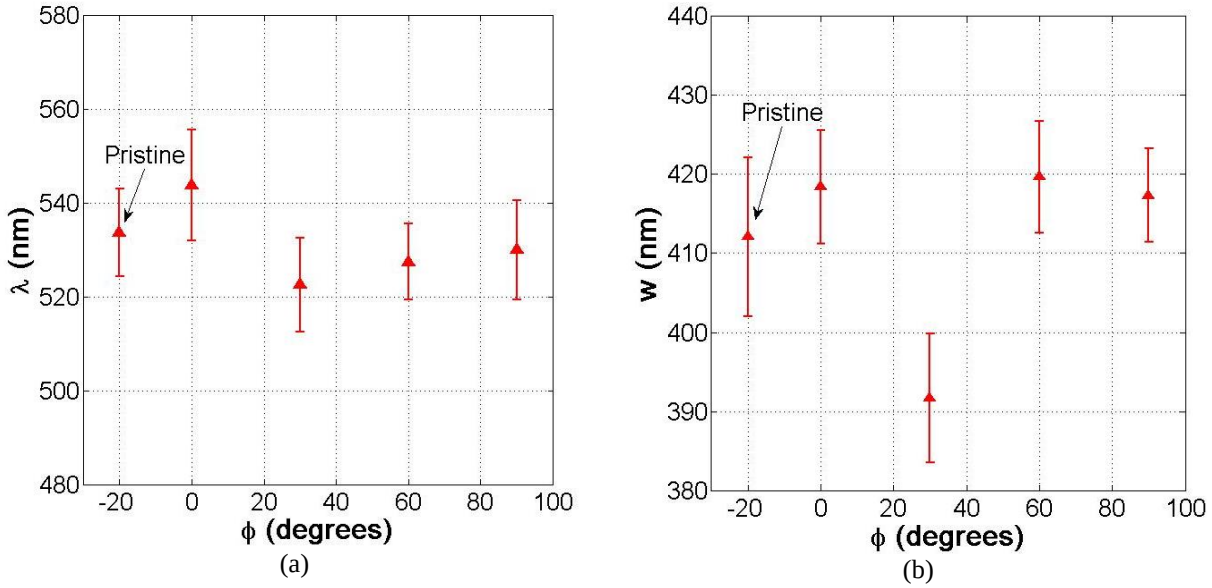

Figure 5.13 (a) λ and (b) w as a function of beam orientation relative to the grating vector after O_2^+ irradiation at E = 500 eV, θ = 60°, φ = 0° – 90°, and Φ = 4.0 x 10^{17} cm^{-2}. The data points at φ = -20° refers to the pristine sample before irradiation.

Last, the effect of varying fluence is examined. Their respective SEM and AFM micrographs are shown in **Figure 5.14**. The irradiation parameters were E = 500 eV, θ = 60°, φ = 0°, and Φ = 2.5 x 10^{17} – 5.0 x 10^{17} cm^{-2}. For O_2^+ irradiation, well-defined ripples also appeared on the surface at all fluences. The periodicity and amplitude of the ripples on some of these samples were estimated using AFM line profiles and plotted against fluence in **Figure 5.15 (a) - (b)**. From the plots both

periodicity and amplitude remained more or less unchanged with fluence. The grating wavelengths (λ), widths of the ridges (w) are plotted in **Figure 5.15 (c) – (d).** Same as before, although there were slight changes in λ and w at certain fluences, there was no noticeable trends of how such changes correlated to the fluence. The 1D rectangular grating shapes also remained unchanged. Several samples are chosen for measurement of film thicknesses on both the ridges and trenches (t_1 and t_3). These results are shown in **Figure 5.15 (e) – (f)**. Their cross-section SEM pictures are shown in **Figure 5.16**. t_1 decreases quite linearly with fluence, but the rate of decrease is apparently slower than in Ar^+ irradiation. Cross-section SEM pictures show the film and gratings has maintained their shapes. Even at a high fluence at $\Phi = 4.0 \times 10^{17}$ cm^{-2}, the film in the trenches still remain. t_3 also decreases quite linearly. The side thickness does not seem to change.

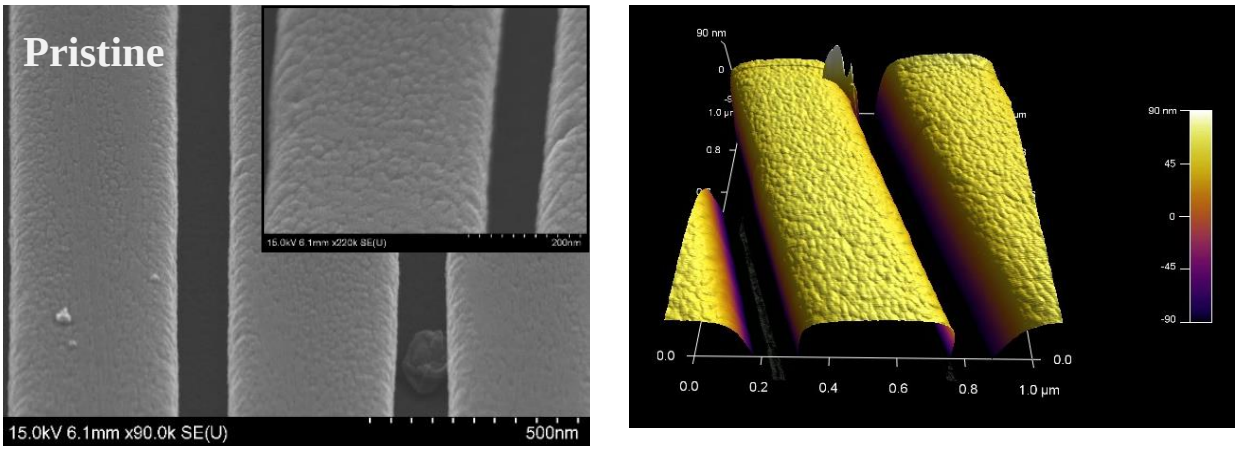

(a) (b)

Figure 5.14 SEM (left) and AFM (right) scans of samples after O_2^+ irradiation at E = 500 eV, θ = 60°, φ = 0°, and Φ = 5 x 10^{16} – 5 x 10^{17} cm^{-2}. Insets are magnified images of the corresponding samples.

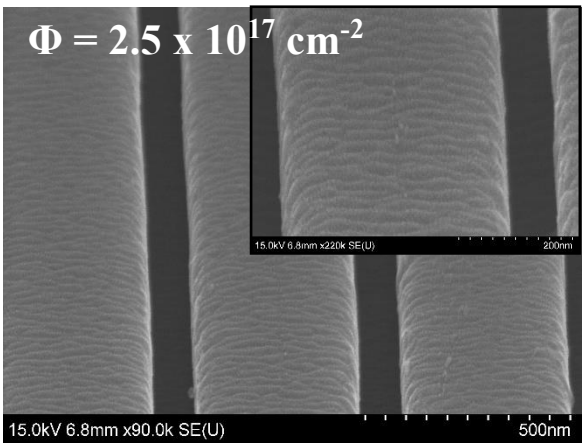

(c)

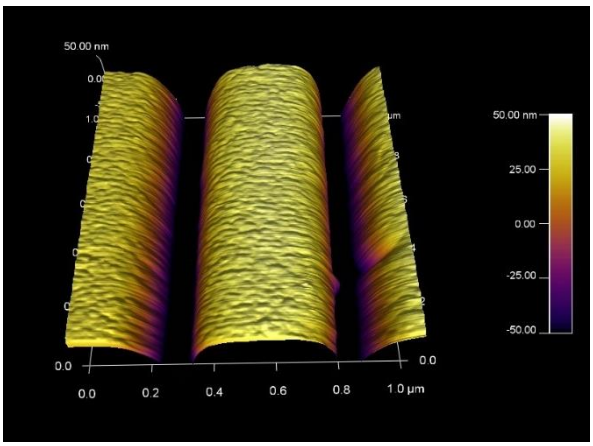

(d)

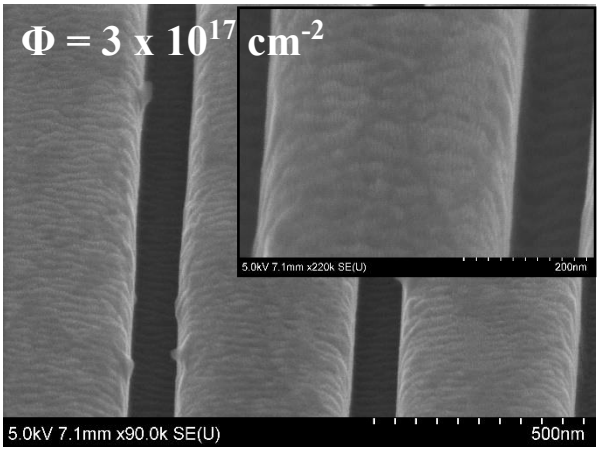

(e)

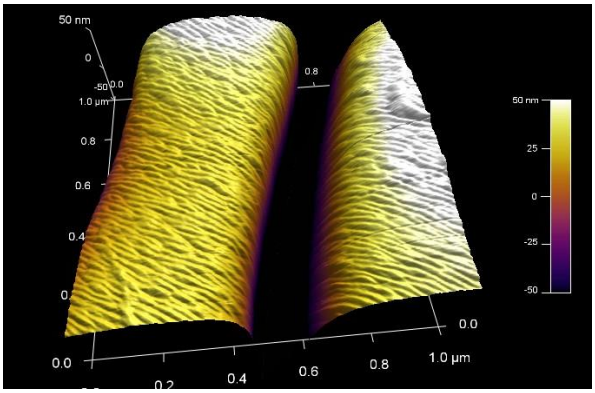

(f)

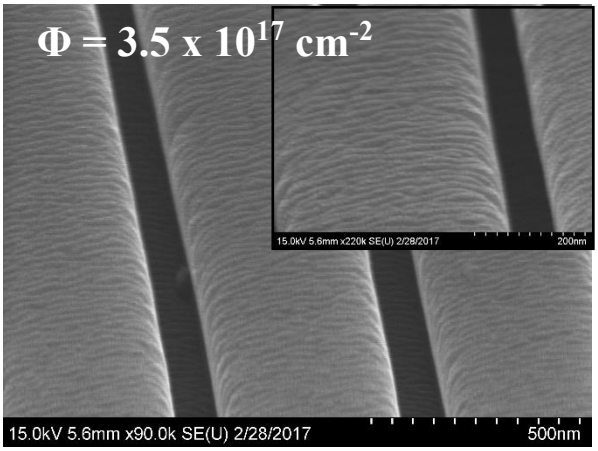

(g)

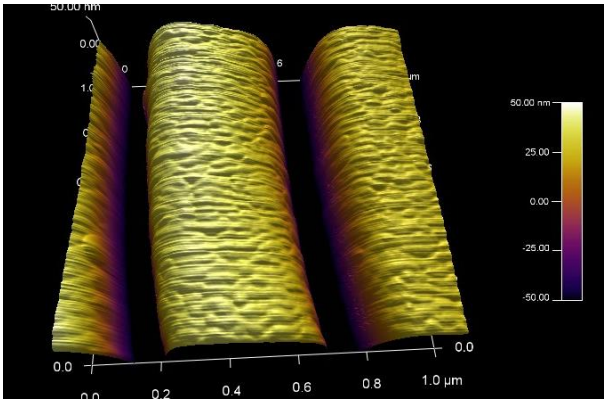

(h)

Figure 5.14 (cont.)

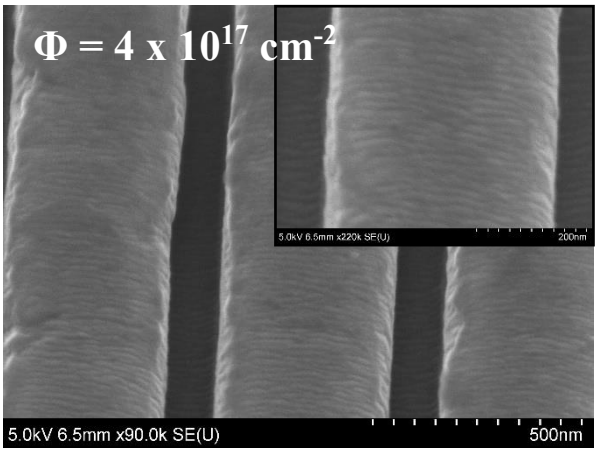

(i)

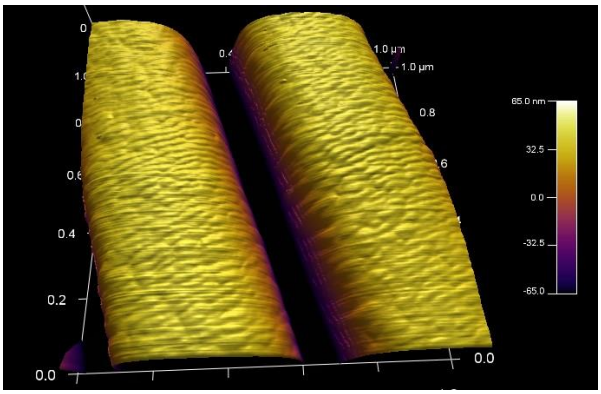

(j)

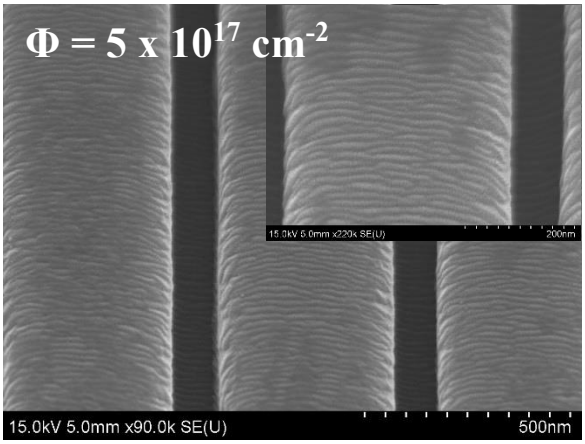

(k)

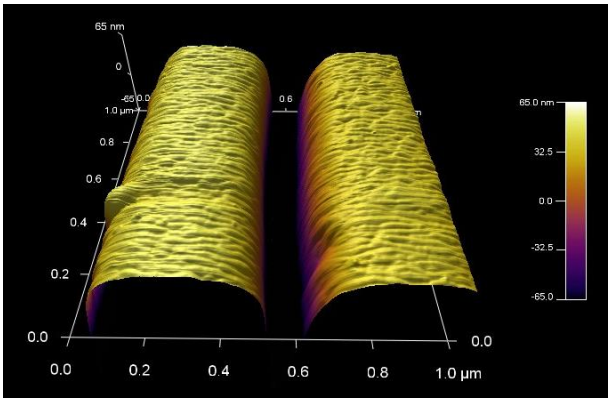

(l)

Figure 5.14 (cont.)

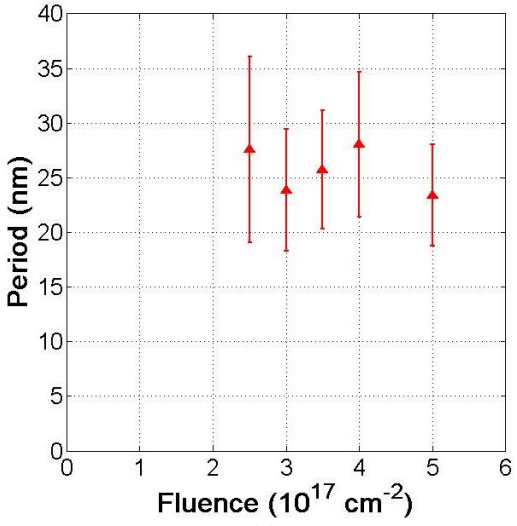

(a)

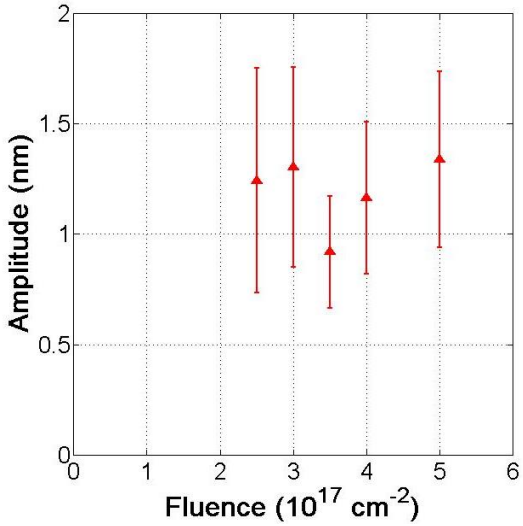

(b)

Figure 5.15 (a) Ripple period, (b) ripple amplitude, (c) λ, (d) w, (e) t_1 and (f) t_3 after O_2^+ irradiation at E = 500 eV, θ = 60°, φ = 0°, and Φ = 2.5 x 10^{16} – 5.0 x 10^{17} cm^{-2}.

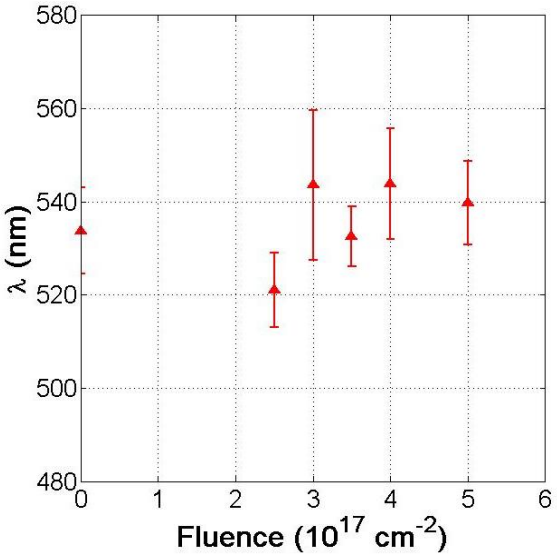

(c)

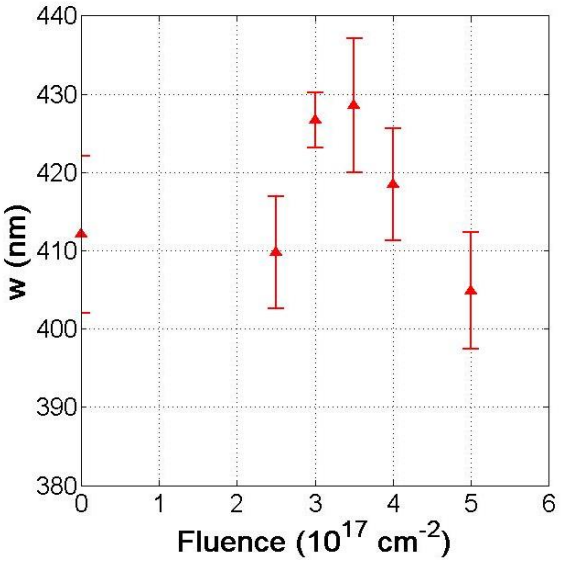

(d)

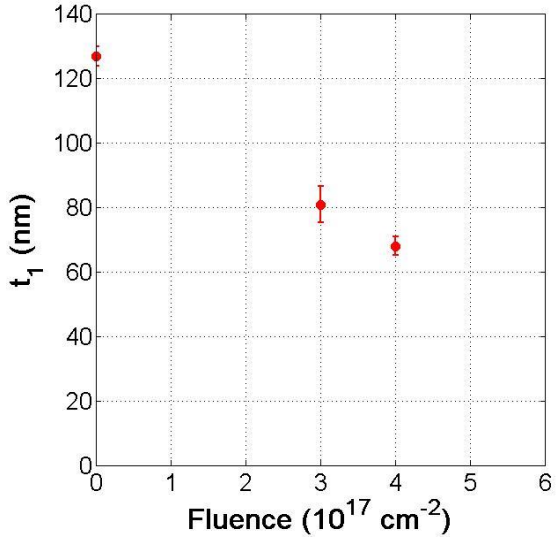

(e)

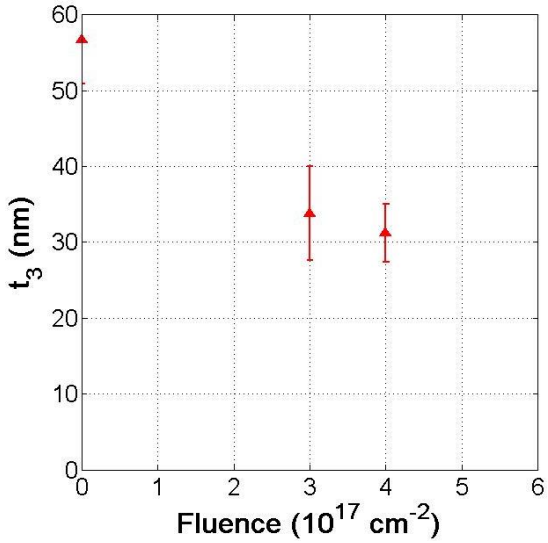

(f)

Figure 5.15 (cont.)

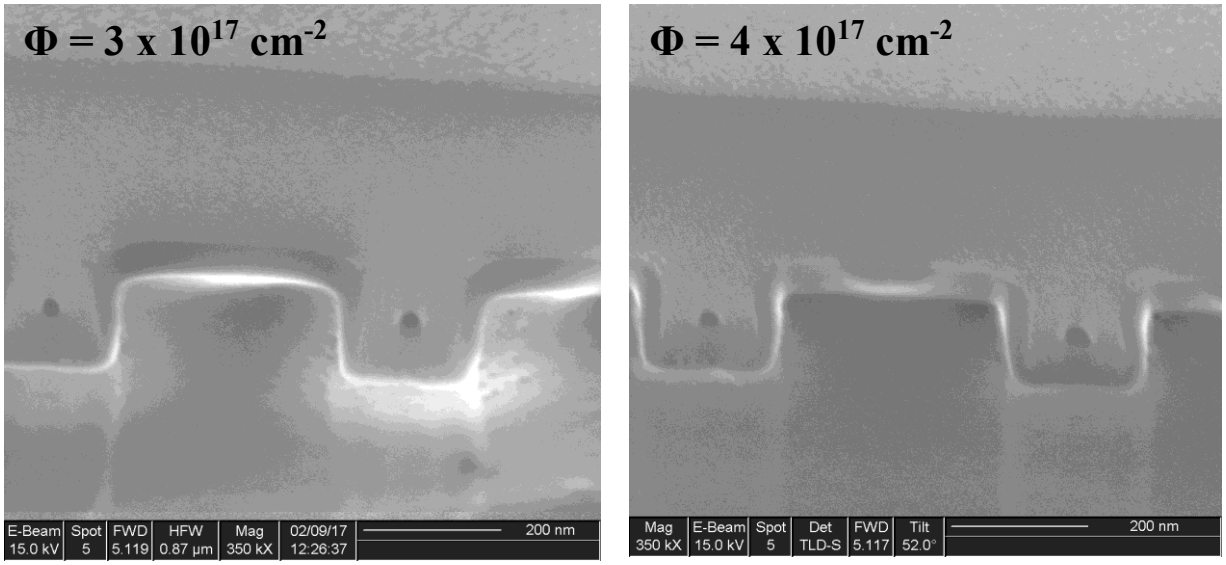

(a) (b)

Figure 5.16 Cross-section SEM micrographs of samples after O_2^+ irradiation at E = 500 eV, θ = 60°, φ = 0°, and Φ = 3 x 10^{17} – 4 x 10^{17} cm^{-2}.

5.3 Discussion and comparison between Ar^+ and O_2^+ irradiation

Several deductions can be made based on the above results. First, the results have clearly indicated a transition from a smoothened surface at normal and small incident angles (θ = 20° in the current experiment) to a roughened nanostructured surface at large angles (θ = 60° in the current experiment). This is in agreement with the theory that a smoothened surface results from small angle incidence irradiation but a nanostructured surface due to induced surface instability at large angles mentioned in **Chapter 2.1**. One exception is when at normal incidence and high fluence (Φ = 1 x 10^{18} cm^{-2}) the surface is smooth at the center of the ridges but slanted and rough on the edges. This phenomenon is surprising, especially since the majority of literature deals with nanopatterning on a flat surface only. Here, however, nanopatterning is performed on a surface with pre-existing large surface features instead. Apparently the edges of the ridges are the cause of such a sharp transition. A possible explanation for this is that when ions approach to the surface, while they are at a normal incidence with respect to the grating surface, they see the edges as a

highly grazing incidence surface instead. While smoothening occurs at normal incidence or small angle irradiation, at a large grazing incidence roughening and appearance of nanostructures occur instead due to a transition from surface stability to instability driven by the induced mass redistribution, as explained in **Chapter 2.1**. At LF the fluence is not high enough to induce any nanostructures or sputter enough materials to erode the edges at all, but at HF the fluence is high enough to induce not only nanostructures, but also sputter away a large amount of materials, and thus eroding the edges so much that they become a slanted surface instead. More experiments will be needed to confirm this hypothesis.

The erosion of edges also leads to an additional factor to consider when performing ion-beam irradiation: the line-edge roughness (LER) of pre-existing structures. LER can be thought as being similar to surface roughness, which is the small statistical fluctuations in surface height, but along one edge of a small feature instead. [120] Even though LER may not be important for PC biosensors, it is also worth paying attention to the effects of irradiation at different conditions to the LER of pre-existing structures in general. For example, in integrated circuit (IC) processing, LER of the transistor gates and other tiny structures on the IC has to be minimized because a high LER can affect the precision of IC processing, for example by causing deviation of dopant distribution and concentration gradient during ion implantation. It can also negatively impact the electronic properties of the transistors, such as variations in current distribution along the gate channels and leakage currents. [121] In this experiment, in addition to the heavy erosion occurred at HF, it is also observed that, when comparing between Ar^+ and O_2^+ irradiations, the edges of the gratings after O_2^+ irradiation seems smoother, as shown in **Figure 5.6** and **Figure 5.14**. Apparently O_2^+ irradiation induces less erosion to the edges, even though it is supposed to be more reactive than Ar^+. This will be explained later in this section.

In addition, the appearance of ripples after large grazing incidence and high fluence irradiation agrees with the literature, but one of the major differences between the results presented here and the literature is that while most literature concerns about nanopatterning of a bulk crystal or films with thickness of the order of microns, here nanopatterning is performed on a very thin film that is ~ 100 nm thick only. From the thickness results, especially with O_2^+ irradiation, ripple patterns can already be created without removing more than ~ 40 nm of the film. This demonstrates the ability of ion irradiation to pattern extremely thin films of even less than 100 nm thick while retaining a sufficient thickness by fine-tuning the irradiation parameters. An even more important difference is that here defined periodic nanostructures have been grown on top of pre-existing larger nanostructures by ion-beam irradiation instead of just flat uniform surfaces. Also, it is mentioned in the above paragraph that two entirely different types of topography exist: a smooth surface at the center and a rough one on the edges, on a ridge that is only ~ 400 nm wide. These demonstrate the ability of ion-beam irradiation to create multi-hierarchical surface topography at a very fine scale while maintaining a relatively simple process compared to conventional wet etching, deposition or other self-assembly processes.

Moreover, the dependence of ripple orientation on beam orientation agrees with the theory by Bradley and Harper that the ripple wave vector is parallel to the beam direction, unless the beam is incident very close to the surface. [53] However, in **Figure 5.11** it can also be seen that the surface of the ridges may become slanted towards one side. Apparently this is also related to the non-homogeneous surface topography, and the presence of edges again seems to play a role in the non-uniform sputtering rate on the surface. However, it is not known if the surface normal of the slanted surface is towards the beam or away from, although the former sounds more reasonable.

Further experiments to align the beam orientation to one specific side of the sample are needed to confirm this.

Both Ar^+ and O_2^+ irradiations are able to create nanostructured ripples on the surface with the appropriate irradiation parameters. However, the changes in surface topography is slightly different between Ar^+ and O_2^+ irradiation. O_2^+ irradiation seems to be able to create more well-defined uniform ripples with relatively less erosion along the edges. However, Ar^+ irradiation is able to create larger ripples. This is clearly shown in **Figure 5.18 (a) – (b)**, which compares the periodicity and amplitude of ripples induced by Ar^+ and O_2^+ ions. In addition, while the periodicity of ripples induced by Ar^+ clearly increases with fluence, in the case of O_2^+ it remained essentially unchanged. In general, Ar^+ ions are able to induce more significant nanopatterns, but at the same time more damage to both the surface and the edges of the pre-existing structures. Three possible factors may cause such differences between Ar^+ and O_2^+ irradiations: mass difference, energy splitting of O_2^+ ions and chemical reactivity. When O_2^+ ions arrive at the surface, they first dissociate into two O^+ ions, each with half of the energy from O_2^+, before interacting with the surface. [ref?] Therefore, Ar^+ ions are more than 2 times heavier than and have double the energy of O^+ ions. The sputter yield of Ar^+ ions is therefore much higher than O_2^+ ions, and thus potentially causing more erosion and wider troughs in the ripples. This effect can also be seen in the effect of increasing fluence on the ripple periodicity in Ar^+ irradiation, in which a higher fluence also leads to more corrosion and thus wider troughs. However, this cannot explain why the ripple periodicity stays the same in O_2^+ irradiation. A possible alternative explanation to this is that since O_2^+ ions are reactive, the surface chemical reaction during the growth of ripples may hinder the erosion such that the width of the trough stays the same over time. More experiments are needed to testify this. In addition, the rate of decrease of film thickness is faster in Ar^+ irradiation. Their comparison

is shown in **Figure 5.18**. This is not surprising because Ar^+, being a heavier species, sputters faster. The rate is linear for both cases, which is also not surprising since sputtering yield does not depend on time, meaning the amount of materials removed from the surface increases linearly with time.

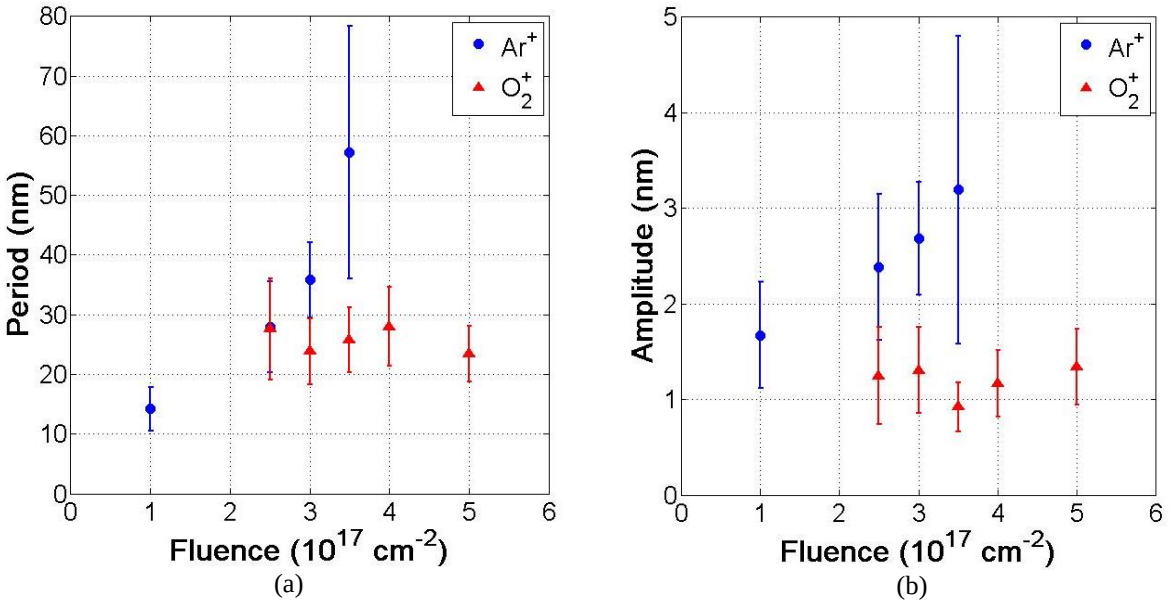

(a) (b)

Figure 5.17 (a) Ripple period and (b) amplitude after Ar^+ or O_2^+ irradiation at E = 500 eV, θ = 60°, φ = 0°, and Φ = 5 x 10^{16} – 5 x 10^{17} cm^{-2}.

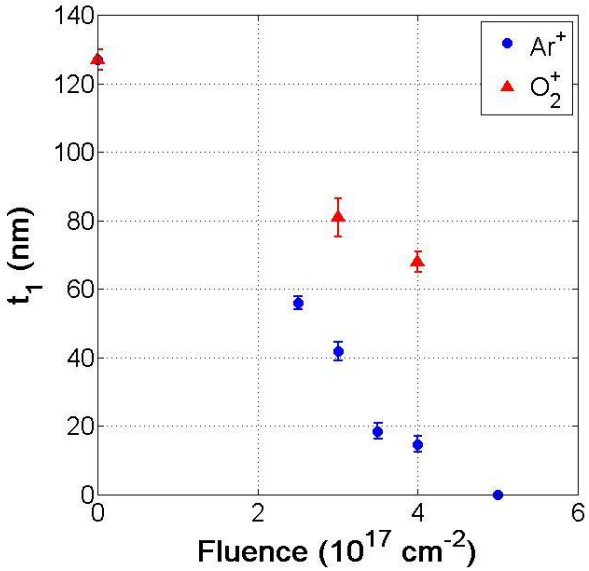

Figure 5.18 Film thickness t_1 after Ar^+ or O_2^+ irradiation at E = 500 eV, θ = 60°, φ = 0°, and Φ = 5 x 10^{16} – 5 x 10^{17} cm^{-2}.

To address the last hypothesis that the increase in surface area due to these nanostructures will be up to the magnitude achieved by GLAD or better, the overall increase in surface area due to these ripple structures is estimated as follow: For the sake of simplifying calculation, it is assumed the ripples have a triangular shape and they exist on the ridges only, so the surface area of each ripple is equal to $A_r = 2w\sqrt{a_r^2 + \left(\frac{\lambda_r}{2}\right)^2}$, where A_r= ripple surface area, a_r = ripple amplitude, and λ_r = ripple period, and w = width of the ridge. Also, the area of the original flat surface of the same region is $A_o = w\lambda_r$. The increase in the surface area then equals $\Delta A = (A_r - A_o)/A_o = \sqrt{\left(\frac{4a_r}{\lambda_r}\right)^2 + 1}$. The error in calculating ΔA, arise from the error propagation of λ_r and a_r as described in **Chapter 4.5**, is then $\sigma_{\Delta A} = \sqrt{\left(\frac{\partial \Delta A}{\partial \lambda_r}\right)^2 \sigma_{\lambda_r}^2 + \left(\frac{\partial \Delta A}{\partial a_r}\right)^2 \sigma_{a_r}^2}$. The surface area increase as a function of increasing fluence is plotted in **Figure 5.19**. From the plot it is observed that there is an overall increase in surface area due to the ripples, but the amount of increase is only 5% or less. Ar^+ irradiation is able to induce slightly larger increase than O_2^+. In addition, the amount of increase in surface area decreases with increasing fluence in the case of Ar^+ irradiation. At first sight this may seem surprising, but this can be explained by observing there is an increase in ripple period but not in amplitude with fluence. However, from the formula for ΔA above, $\Delta A \propto 1/\lambda_r$. This implies if amplitude stays the same, increase in ripple period actually causes a decrease in the amount of increase in surface area. The area increase due to O_2^+ irradiation stays the same over fluence because both the ripple period and amplitude is the same. However, when compared to the area increase due to nanorods grown by GLAD, the increase due to ripples is miniscule. The area increase due to GLAD was found to be ~ 4 times of a flat surface. [100] The nanorods also have a height of ~ 85 nm and diameter and spacing of several tens of nanometers (refer to **Figure 3.1**), which are also much larger than the ripples grown in this experiment. [100] A possible explanation

for the significant difference in surface area increase is that the nanorods are grown by deposition, which can ensure a sufficient amount of materials available for the growth. However, the ripples were induced by surface sputtering instead. There is a limited amount of material for the growth of ripples, which in turn posed constraints to the maximum irradiation time (fluence) before all the materials are removed. This obstacle may be overcome by co-deposition of additional TiO_2 during irradiation. This can be investigated in another experiment since in this case an additional element is involved in the process of ion-surface interactions, which may induce other interesting topographical changes. Nevertheless, on the positive side, the different surface topography due to ion irradiation showed that this technique has a higher controllability than GLAD. For example, GLAD cannot grow nanostructures at only certain areas while keeping other areas smooth unless a mask is used, but irradiation has this ability without using any masks or additional steps (for example, see **Figure 5.1**).

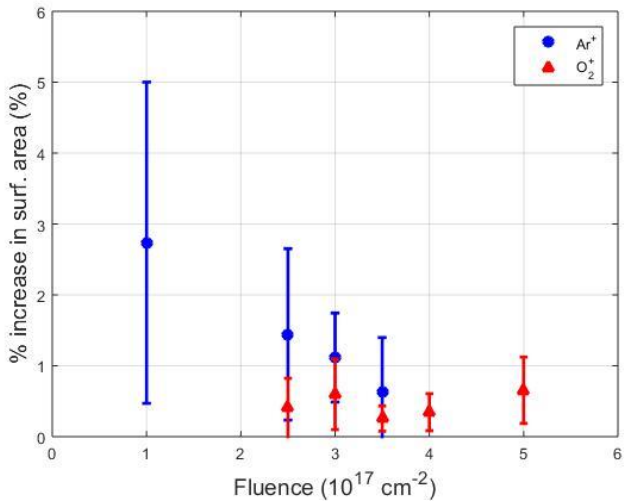

Figure 5.19 Percentage increase in surface area due to ripples induced by Ar^+ or O_2^+ irradiation at E = 500 eV, θ = 60°, φ = 0°, and Φ = 5 x 10^{16} – 5 x 10^{17} cm^{-2}.

The grating shape and size does not change in general after irradiation. One exception is at HF and normal incidence, in which w is increased significantly as shown in **Figure 5.3**. Such widening

could be caused by re-deposition of materials removed from the ridges surface. This re-deposition effect can also be seen in the cross-section SEM images shown in **Figure 5.8** and **Figure 5.16**, in which the sides appear to have thickened, although their w values do not appear to have changed. Re-deposition on the sides may be caused by deposition of materials being sputtered from the trenches at a high fluence. Therefore, it is possible at HF and normal incidence, the re-deposition caused by materials sputtered off from both the ridges and trenches is so much more significant that a lot of materials have been re-deposited and causes w to have a significant increase. A cross-section SEM scan of the samples at HF and more experiments at a similar fluence will be needed in the future to confirm this.

In general, these results have indicated the hypotheses described at the beginning of this chapter is partly true. It is seen that a smooth surface is created at low fluence normal incidence irradiation, and nanosized ripples are created at high fluence large grazing incidence irradiation. Also, the edges of the ridges are influential to the topographical changes, as seen in **Figure 5.1** and **Figure 5.11**. However, no other types of nanostructures such as nanorods, nanocones can be seen. Moreover, the increase in surface area due to irradiation was not able to reach the level achieved by GLAD. These may be due to insufficient fluence and/or energy to induce a greater disturbance to the surface to create larger or a wider variety of structures. However, the film used in this experiment was not thick enough to withstand a high fluence and/or energy without being completely removed.

CHAPTER 6: SURFACE CHEMISTRY CHANGES DUE TO ION IRRADIATION

This chapter covers the surface chemistry changes due to ion-beam irradiation under different parameters. The goal of this chapter is to address the third hypothesis: ion irradiation may induce surface chemistry changes depending on the ion beam parameters and the reactivity of ion species. Ar^+ is hypothesized to induce relatively little chemistry changes compared to O_2^+ since Ar^+ is inert while O_2^+ is reactive. Surface chemistry changes after irradiation is quantified by *ex-situ* XPS. In this chapter, changes due to Ar^+ and O_2^+ irradiation will be discussed separately in their respective subsection. A comparison between them will be made in the end.

6.1 Ar^+ irradiation

Effects of varying energies, incident angle θ and fluence Φ are examined in the case of Ar^+ irradiation. First, effect of varying energies will be presented. The irradiation parameters were E = 250 – 1000 eV, $\theta = 0^o$, $\varphi = 0^o$, and $\Phi = 5 \times 10^{16}$ (LF) and 1×10^{18} (HF) cm^{-2}. **Figure 6.1 (a) – (b)** shows the survey and Ti2p and O1s core regions of the samples irradiated at varying energies. On the survey spectrum of pre-irradiated sample, six main peaks were observed at binding energies of around 285 eV, 460 eV, 530 eV, 568 eV, 978 eV and 1072 eV. The first four peaks were photoelectron peaks corresponding to C 1s, Ti 2p, O 1s and Ti 2s respectively, and the last two were Auger peaks corresponding to O KLL and Ti LMM respectively. After irradiation, in all cases all these peaks still existed, indicating all the elements remained on the surface. In addition, several smaller peaks appeared, and they corresponded to Fe 2p, F 1s, N 1s, Ca 2p and Ar 2p. The contamination issue becomes significant when the energy is below 500 eV. To examine the chemical state of Ti and O, and hence the stoichiometry of TiO_x on the surface, Ti 2p and O 1s

core region scans were shown in **Figure 6.1 (c) – (f).** Since the presence of C 1s peak corresponded to carbon contaminants on the surface only, a C 1s core region will not be presented in this chapter. On the Ti 2p spectrum of pre-irradiated surface, a double peak was seen at 458.6 eV and 464.3 eV, corresponding to Ti $2p_{3/2}$ and Ti $2p_{1/2}$ of Ti^{4+} respectively. On the O 1s spectrum of pre-irradiated surface, a single peak was seen at 530.0 eV, corresponding to O 1s of O^{2-}. In addition, a small shoulder on the left of the main peak was seen. A deconvolution of the spectrum showed that this shoulder corresponded to two additional peaks. A small shoulder of several eVs higher than the main peak usually indicates the presence of hydroxyl (OH^-) groups and physisorbed H_2O. [115,116] Such shoulder usually consists of two peaks, one corresponding to OH^- about 1.6 eV, and the other is physisorbed H_2O groups about 3 eV higher than the main peak. [115,116] After irradiation at E = 500 eV and higher, in the Ti 2p spectrum, a doublet corresponding to Ti^{4+} remains with negligible binding energy shifts (± 0.2 eV). However, a small but non-negligible shoulder appeared on the right of the Ti $2p_{3/2}$ peak. This is characteristic of a reduction of a small amount of Ti^{4+} to Ti^{3+} and even Ti^{2+} oxidation states. A deconvolution of the shoulder also indicated the presence of two additional peaks at 456.8 eV and 455.6 eV. These peaks correspond to Ti^{3+} $2p_{3/2}$ and Ti^{2+} $2p_{3/2}$ and respectively. Since these 2p peaks should be doublets, two additional peaks corresponding to Ti^{3+} $2p_{1/2}$ and Ti^{2+} $2p_{1/2}$ were assigned to the spectrum at a binding energy of ~ 6 eV higher than their corresponding $2p_{3/2}$ peaks respectively. In the O 1s spectrum, the main peak corresponding to O^{2-} remained at the same binding energy. The intensity of the shoulder changed in some cases. From the Ti 2p, O 1s and C 1s core spectra, the relative atomic concentrations of the major elements (carbon, oxygen which is bonded to Ti, physisorbed H_2O and OH^- groups on the surface, and Ti) were calculated and listed in **Table 6.1**. Disregarding the E = 250 eV at HF sample, The Ti/O ratio remained unchanged at around 0.5. The amount of carbon, H_2O and OH^- groups sometimes

becomes higher than pre-irradiation. At E = 250 eV, the amount of contaminants was found to be around 5%. The ratio between reduced states of Ti and overall Ti is also listed in **Table 6.1,** and found to be no more than 0.15.

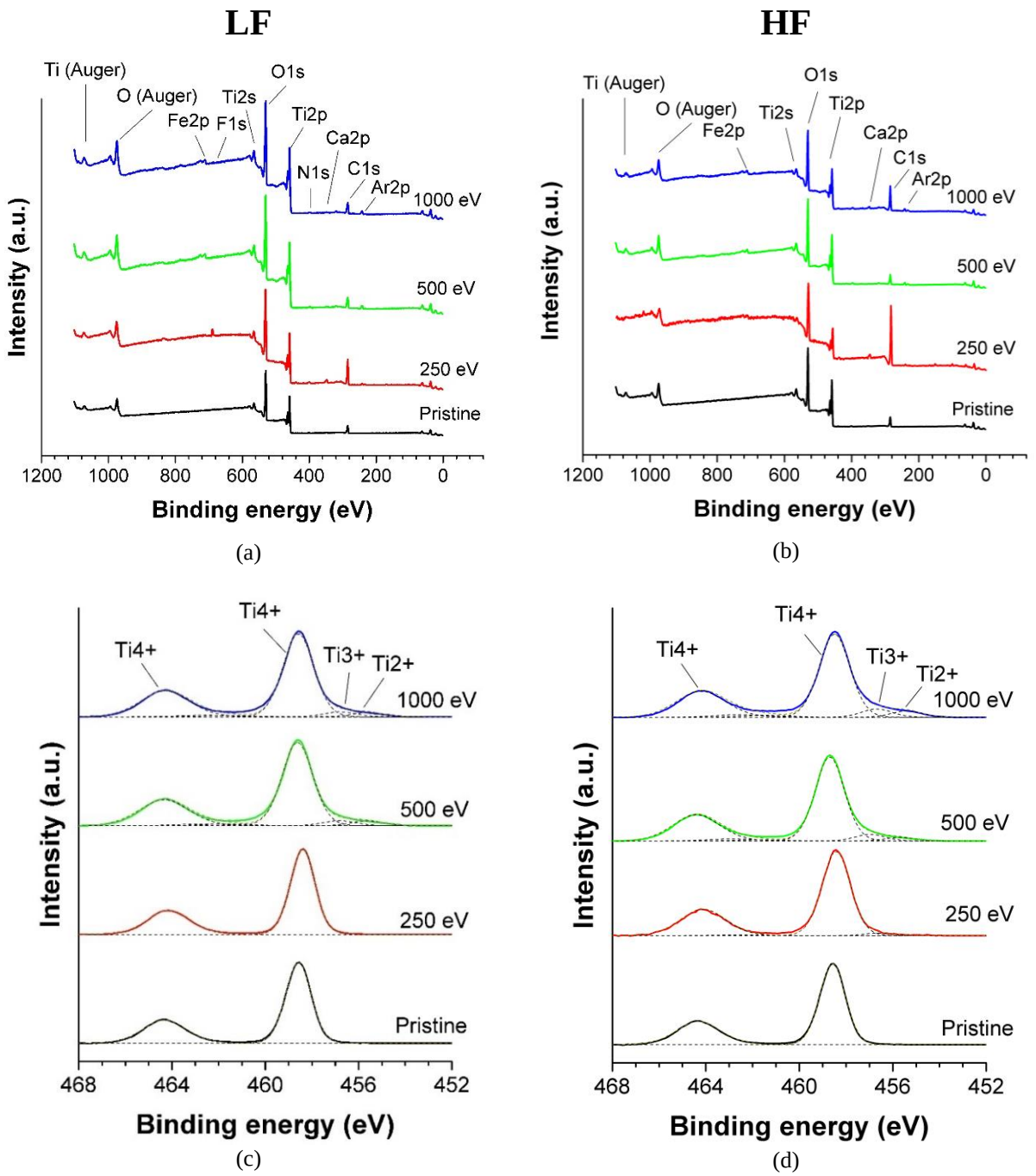

Figure 6.1 XPS survey, Ti 2p and O 1s core scans of samples after Ar^+ irradiation at E = 250 – 1000 eV, θ = 0°, φ = 0°, and Φ = 5 x 10^{16} (LF) and 1 x 10^{18} (HF) cm^{-2}. The values in the legend correspond to E. Spectra on the left and right correspond to LF and HF respectively. The O 1s spectrum of E = 250 eV at HF is not available. All data were acquired using Kratos.

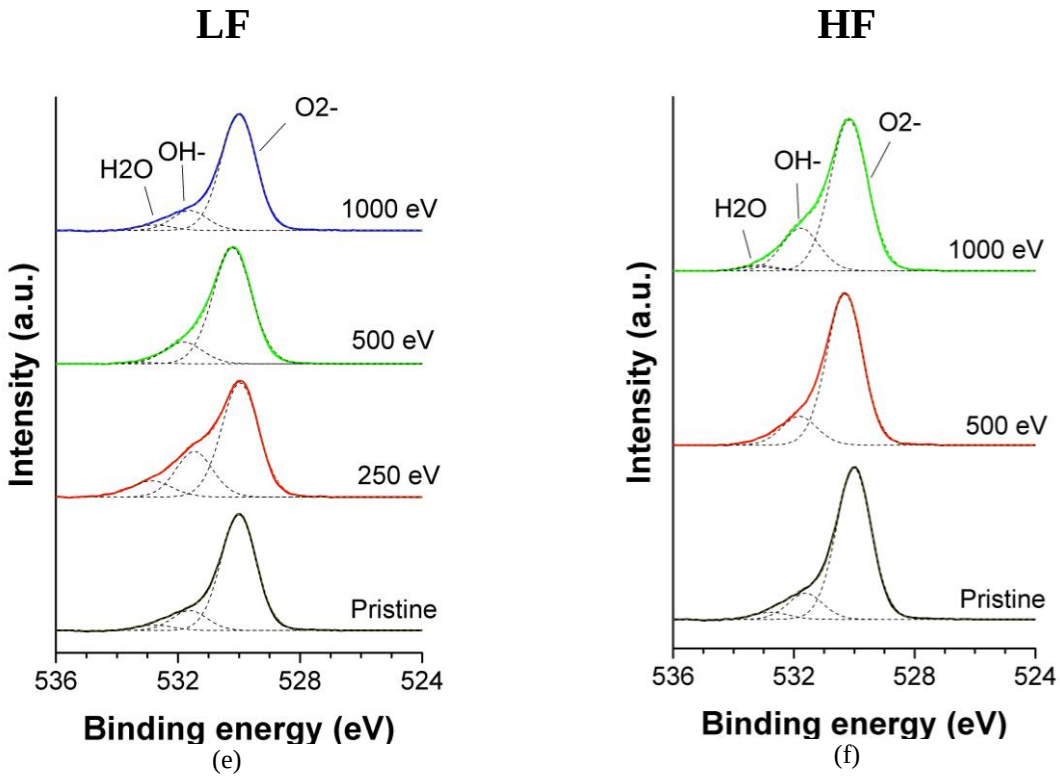

Figure 6.1 (cont.)

Table 6.1 Relative atomic concentration of major elements on the surface after Ar^+ irradiation at E = 250 - 1000 eV, θ = 0°, φ = 0°, and Φ = 5 x 10^{16} (LF) and 1 x 10^{18} (HF) cm^{-2}. The values have an accuracy of ~10%.

Energy (eV), Φ	**Atomic percentage of major elements (%)**				**Ratio**	
	C	Ti	O (O^{2-})	O (H_2O + OH^-)	Ti/O	(Ti^{2+}+Ti^{3+})/Ti
Pristine	27.1	20.9	42.6	9.3	0.49	--
250 eV, LF	39.9	15.4	28.8	16.0	0.53	--
500 eV, LF	21.4	23.1	46.4	9.1	0.50	0.11
1000 eV, LF	21.3	22.9	46.4	9.4	0.49	0.10
250 eV, HF*	67.0	5.06	24.63	Not available	0.21	0.03
500 eV, HF	25.9	21.6	43.1	9.3	0.50	0.11
1000 eV, HF	44.4	14.94	30.79	9.9	0.49	0.15

* Since the O 1s core spectrum was not available, the calculation was based on the survey spectrum instead. Therefore, the atomic concentration of H_2O and OH^- groups was incorporated into the concentration of O^{2-} groups as the O 1s peak in the survey spectrum cannot be deconvoluted. Hence, the Ti/O ratio becomes much lower than others.

Next, the effect of varying incident angle θ is examined. The irradiation parameters were E = 500 eV, θ = 20° – 60°, φ = 0°, and Φ = 2.5 x 10^{17} cm^{-2}. **Figure 6.2** shows the survey, Ti 2p and O 1s core regions of the samples irradiated at varying θ. In the survey spectrum, the main peaks corresponding to C 1s, Ti 2p, O 1s and Ti 2s photoelectron peaks and the O KLL and Ti LMM Auger peaks can still be observed, indicating all the elements remained on the surface. Smaller peaks corresponding to Fe 2p, Ca 2p and Mo 3d can also be observed. In the Ti 2p spectrum the double peak at 458.6 eV and 464.3 eV, corresponding to Ti $2p_{3/2}$ and Ti $2p_{1/2}$ of Ti^{4+} respectively, remained. The binding energies in the case of θ = 60° remained unchanged, but was decreased by around 0.5 eV in the case of θ = 20°. This shift might be due to instrumental and other random variations, since the XPS instrument used for samples irradiated at θ = 20° was different than the rest, and also a slight variation of binding energies of Ti peaks was reported among different researchers. A shoulder corresponding to reduced Ti states was present in the case of θ = 20°, but was absent when θ = 60°. A deconvolution of the shoulder indicated the presence of a small amount of Ti^{3+} and Ti^{2+}. In the O 1s spectrum, a main peak corresponding to O 1s of O^{2-} was still present. Same as in the Ti spectrum, the binding energy was decreased by around 0.5 eV in the case of θ = 20°, but remained unchanged in the case of θ = 60°. A small shoulder on the left of the main peak, corresponding to OH^- and physisorbed H_2O, was still present. The intensity of the shoulder changed in some cases. The relative atomic concentrations of the major elements (carbon, oxygen which is bonded to Ti, physisorbed H_2O and OH^- groups on the surface, and Ti) were calculated and listed in **Table 6.2**. The Ti/O ratio increased slightly after irradiation at θ = 20°, but decreased after irradiation at θ = 60°. The amount of carbon, H_2O and OH^- groups sometimes becomes higher than pre-irradiation. The ratio between reduced states of Ti and overall Ti is also listed in **Table 6.2** and found to be no more than 0.12.

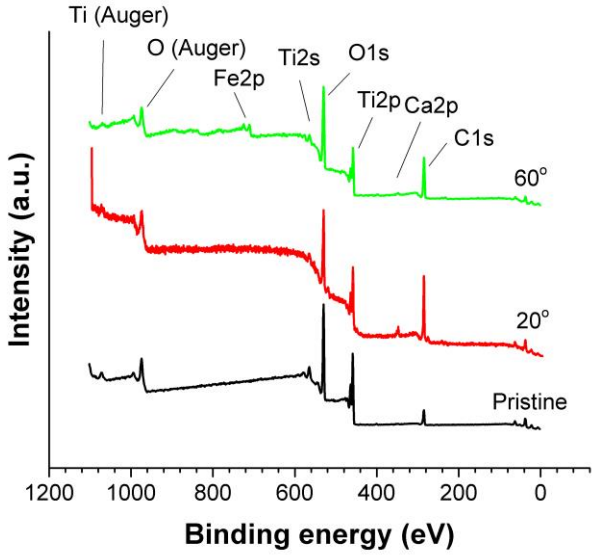

(a)

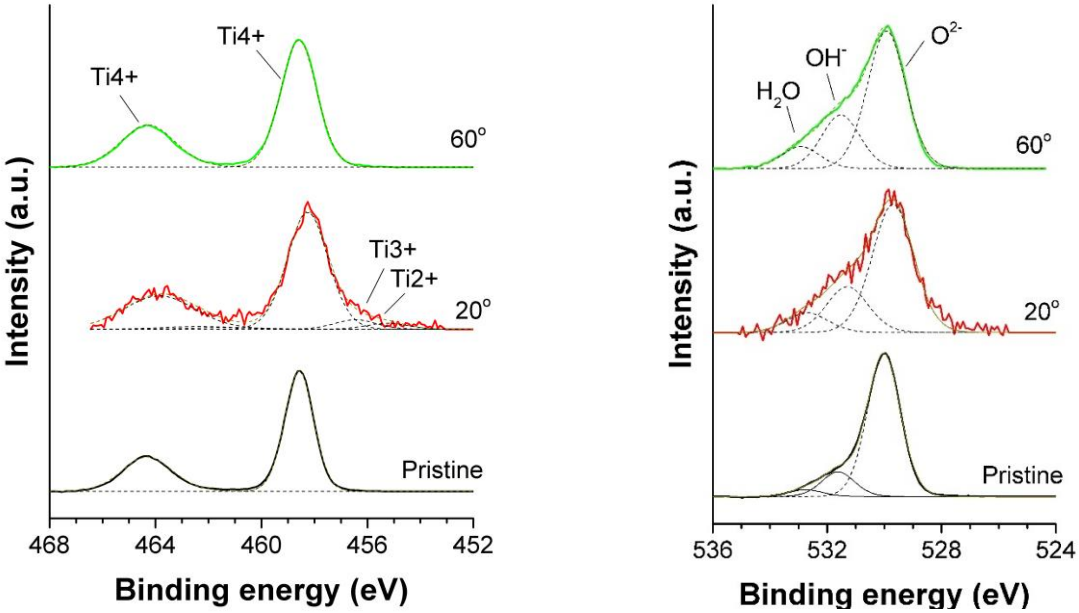

(b) (c)

Figure 6.2 XPS survey, Ti 2p and O 1s core scans of samples after Ar^+ irradiation at E = 500 eV, θ = 20° – 60°, φ = 0°, and Φ = 2.5 x 10^{17} cm^{-2}. The values in the legend correspond to θ. The data for θ = 20° case were acquired using PHI, while the rest were acquired using Kratos.

Table 6.2 Relative atomic concentration of major elements on the surface after Ar^+ irradiation at E = 500 eV, θ = 20º – 60º, φ = 0º, and Φ = 2.5 x 10^{17} cm^{-2}. The values have an accuracy of ~10%.

θ	Atomic percentage of major elements (%)				Ratio	
	C	Ti	O (O^{2-})	O (H_2O + OH^-)	Ti/O	(Ti^{2+}+Ti^{3+})/Ti
Pristine	27.1	20.9	42.6	9.3	0.49	--
20º	52.6	12.2	23.3	11.9	0.53	0.12
60º	52.1	10.1	24.4	13.4	0.42	--

Last, the effect of varying fluence is examined. The irradiation parameters were E = 500 eV, θ = 60º, φ = 0º, and Φ = 0.5 x 10^{17} – 5.0 x 10^{17} cm^{-2}. **Figure 6.3** shows the survey, Ti2p and O1s core regions of the samples irradiated at varying fluence. In the survey spectrum, the main peaks corresponding to C 1s, Ti 2p, O 1s and Ti 2s photoelectron peaks and the O KLL and Ti LMM Auger peaks can still be observed, indicating all the elements remained on the surface. An exception is the disappearance of Ti peak at Φ = 5 x 10^{17} cm^{-2}. This indicates a complete removal of the TiO_2 film. Negligible contamination was observed this time. In the Ti 2p spectrum the double peak at 458.6 eV and 464.3 eV, corresponding to Ti $2p_{3/2}$ and Ti $2p_{1/2}$ of Ti^{4+} respectively, remained. The binding energies were negligibly shifted (± 0.2 eV). A tiny shoulder corresponding to reduced Ti states was present in some cases only. A deconvolution of the shoulder indicated the presence of a tiny amount of Ti^{3+} and Ti^{2+}. The deconvolution was not shown for irradiated samples. In the O 1s spectrum, a main peak corresponding to O 1s of O^{2-} was still present. The binding energy shifts were also negligible (± 0.2 eV). A small shoulder on the left of the main peak, corresponding to OH^- and physisorbed H_2O, was still present. The intensity of the shoulder changed in some cases. The relative atomic concentrations of the major elements (carbon, oxygen which is bonded to Ti, physisorbed H_2O and OH^- groups on the surface, and Ti) were calculated

and listed in **Table 6.3**. The Ti/O ratio decreased slightly after Ar^+ irradiation at certain fluences. The amount of carbon, H_2O and OH^- groups sometimes becomes higher than pre-irradiation. The ratio between reduced states of Ti and overall Ti is also listed in **Table 6.3** and found to be ≤ 0.05.

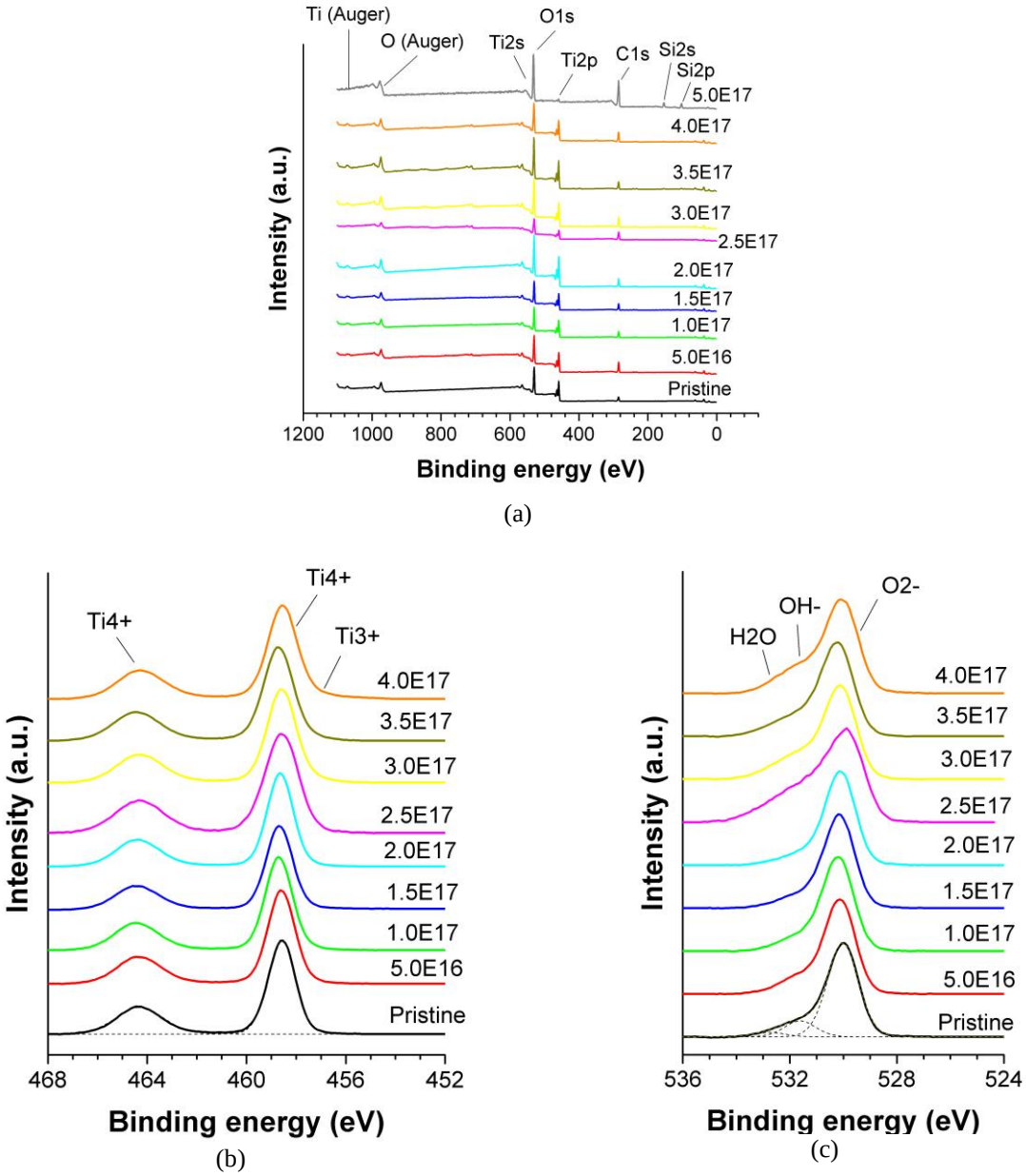

Figure 6.3 XPS survey, Ti 2p and O 1s core scans of samples after Ar^+ irradiation at E = 500 eV, θ = 60°, φ = 0°, and Φ = 5 x 10^{16} – 5 x 10^{17} cm^{-2}. The values in the legend correspond to Φ. A core scan of the sample irradiated at Φ = 5 x 10^{17} cm^{-2} with Ar^+ was not performed due to the nonexistence of Ti peak in the survey scan. All the data were acquired using Kratos.

Table 6.3 Relative atomic concentration of major elements on the surface after Ar^+ irradiation at E = 500 eV, θ = 60°, φ = 0°, and Φ = 5 x 10^{16} – 4 x 10^{17} cm^{-2}. The data for Φ = 5 x 10^{17} cm^{-2} is omitted here due to the nonexistence of the oxide film, and hence no reason to compare them with the rest. The values have an accuracy of ~10%.

Φ ($10^{17}$$cm^{-2}$)	**Atomic percentage of major elements (%)**				**Ratio**	
	C	Ti	O (O^{2-})	O (H_2O + OH^-)	Ti/O	(Ti^{2+}+Ti^{3+})/Ti
Pristine	27.1	20.9	42.6	9.3	0.49	--
0.5	39.7	16.4	36.4	7.5	0.45	0.01
1.0	33.1	19.0	41.2	6.7	0.46	0.02
1.5	34.5	18.7	40.4	6.4	0.46	0.01
2.0	27.9	20.9	44.9	6.4	0.46	0.01
2.5	52.1	10.1	24.4	13.4	0.42	--
3.0	46.1	12.1	26.6	15.2	0.45	--
3.5	29.4	17.9	41.0	11.7	0.44	0.02
4.0	42.7	14.5	32.1	10.7	0.45	0.05

6.2 O_2^+ irradiation

Effects of varying incident angle θ, beam orientation φ and fluence Φ are examined in the case of O_2^+ irradiation. First, effect of varying θ will be presented. The irradiation parameters were E = 500 eV, θ = 20° – 60°, φ = 0°, and Φ = 2.5 x 10^{17} cm^{-2}. **Figure 6.4** shows the survey, Ti2p and O1s core regions of the samples irradiated at varying θ. In the survey spectrum, the main peaks corresponding to C 1s, Ti 2p, O 1s and Ti 2s photoelectron peaks and the O KLL and Ti LMM Auger peaks can still be observed, indicating all the elements remained on the surface. Smaller peaks corresponding to Fe 2p, Ca 2p and Mo 3d can also be observed. In the Ti 2p spectrum the double peak at 458.6 eV and 464.3 eV, corresponding to Ti $2p_{3/2}$ and Ti $2p_{1/2}$ of Ti^{4+} respectively, remained. The binding energies in the case of θ = 60° remained unchanged, but was decreased by

around 0.5 eV in the case of $\theta = 20^{o}$. This shift is essentially the same as in the case of Ar^{+} irradiation with the same parameters. A shoulder corresponding to reduced Ti states was present in the case of $\theta = 20^{o}$, but was absent when $\theta = 60^{o}$. A deconvolution of the shoulder indicated the presence of Ti^{3+}. In the O 1s spectrum, a main peak corresponding to O 1s of O^{2-} was still present. Same as in the Ti spectrum, the binding energy was decreased by around 0.5 eV in the case of $\theta = 20^{o}$, but remained unchanged in the case of $\theta = 60^{o}$. A small shoulder on the left of the main peak, corresponding to OH^{-} and physisorbed H_2O, was still present. The intensity of the shoulder changed in some cases. The relative atomic concentrations of the major elements (carbon, oxygen which is bonded to Ti, physisorbed H_2O and OH^{-} groups on the surface, and Ti) were calculated and listed in **Table 6.4**. The Ti/O ratio increased slightly after irradiation at $\theta = 20^{o}$, but decreased after irradiation at $\theta = 60^{o}$. The amount of carbon, H_2O and OH^{-} groups sometimes becomes higher than pre-irradiation. The ratio between reduced states of Ti and overall Ti is also listed in **Table 6.4** and found to be no more than 0.05.

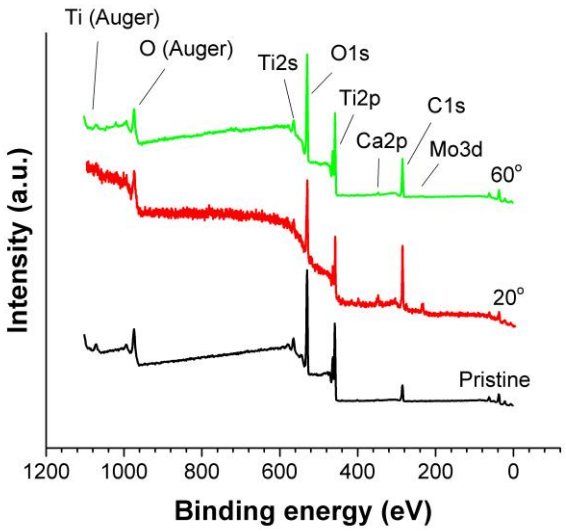

(a)

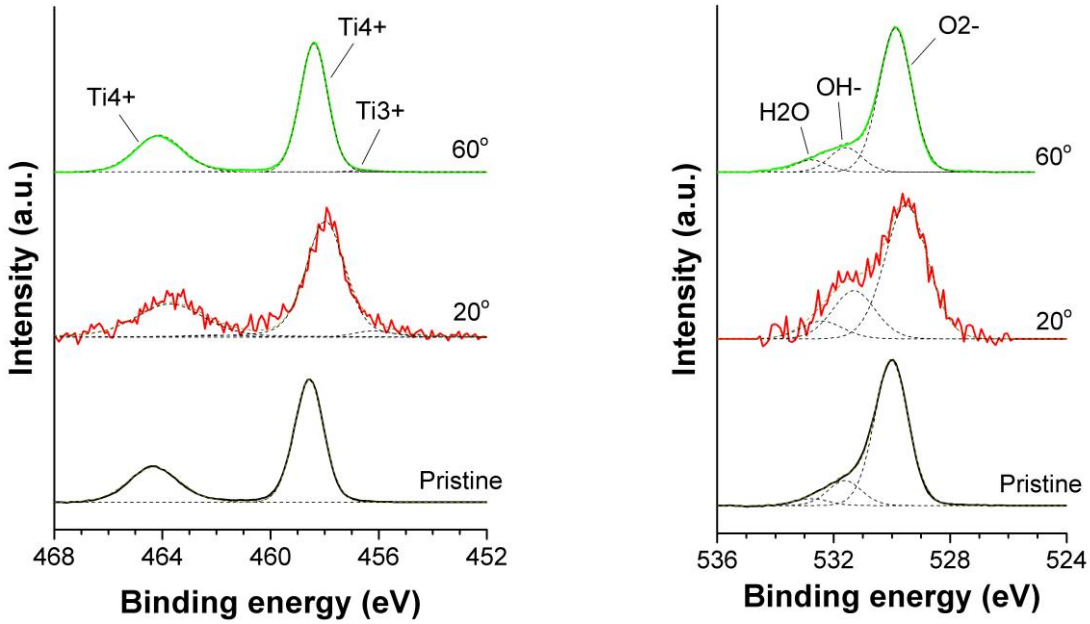

(b) (c)

Figure 6.4 XPS survey, Ti 2p and O 1s core scans of samples after O_2^+ irradiation at E = 500 eV, θ = 20° – 60°, φ = 0°, and Φ = 2.5 x 10^{17} cm^{-2}. The values in the legend correspond to θ. Spectra on the left and right correspond to Ar^+ and O_2^+ irradiation respectively. The data for θ = 20° case were acquired using PHI, while the rest were acquired using Kratos.

Table 6.4 Relative atomic concentration of major elements on the surface after O_2^+ irradiation at E = 500 eV, θ = 20º – 60º, φ = 0º, and Φ = 2.5 x 10^{17} cm^{-2}. The values have an accuracy of ~10%.

θ	Atomic percentage of major elements (%)				Ratio	
	C	Ti	O (O^{2-})	O (H_2O + OH^-)	Ti/O	(Ti^{2+}+Ti^{3+})/Ti
Pristine	27.1	20.9	42.6	9.3	0.49	--
20º	56.7	11.1	21.7	10.6	0.51	0.05
60º	41.7	15.6	33.94	8.7	0.46	0.01

Next, the effect of varying φ is examined. The irradiation parameters were E = 500 eV, θ = 60º, φ = 0º – 90º, and Φ = 4.0 x 10^{17} cm^{-2}. **Figure 6.5** shows the survey, Ti2p and O1s core regions of the samples irradiated at varying φ. In the survey spectrum, the main peaks corresponding to C 1s, Ti 2p, O 1s and Ti 2s photoelectron peaks and the O KLL and Ti LMM Auger peaks can still be observed, indicating all the elements remained on the surface. A smaller peak corresponding to Fe 2p from contaminants can also be observed. In the Ti 2p spectrum the double peak at 458.6 eV and 464.3 eV, corresponding to Ti $2p_{3/2}$ and Ti $2p_{1/2}$ of Ti^{4+} respectively, remained. The binding energies were negligibly shifted (± 0.2 eV) A tiny shoulder corresponding to reduced Ti states was present in some cases only. A deconvolution of the shoulder indicated the presence of a tiny amount of Ti^{3+}. In the O 1s spectrum, a main peak corresponding to O 1s of O^{2-} was still present. The binding energy shifts were also negligible (± 0.2 eV). A small shoulder on the left of the main peak, corresponding to OH^- and physisorbed H_2O, was still present. The intensity of the shoulder changed in some cases. The relative atomic concentrations of the major elements (carbon, oxygen which is bonded to Ti, physisorbed H_2O and OH^- groups on the surface, and Ti) were calculated and listed in **Table 6.5**. The Ti/O ratio decreased slightly after irradiation, and the decrease seemed to be slightly larger at larger φ. The amount of carbon, H_2O and OH^- groups sometimes becomes

higher than pre-irradiation. The ratio between reduced states of Ti and overall Ti is also listed in **Table 6.5** and found to be ≤ 0.01.

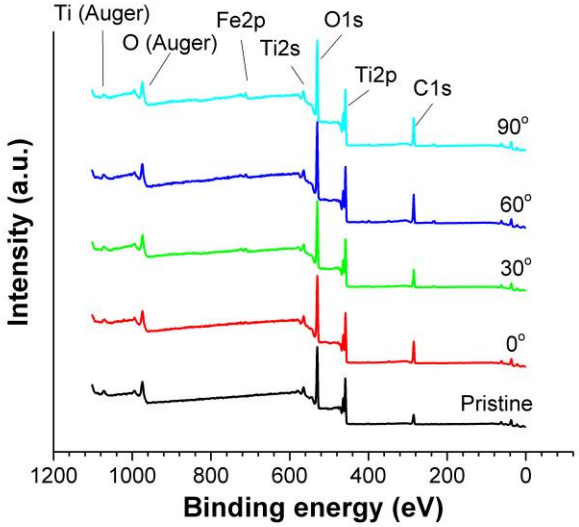

(a)

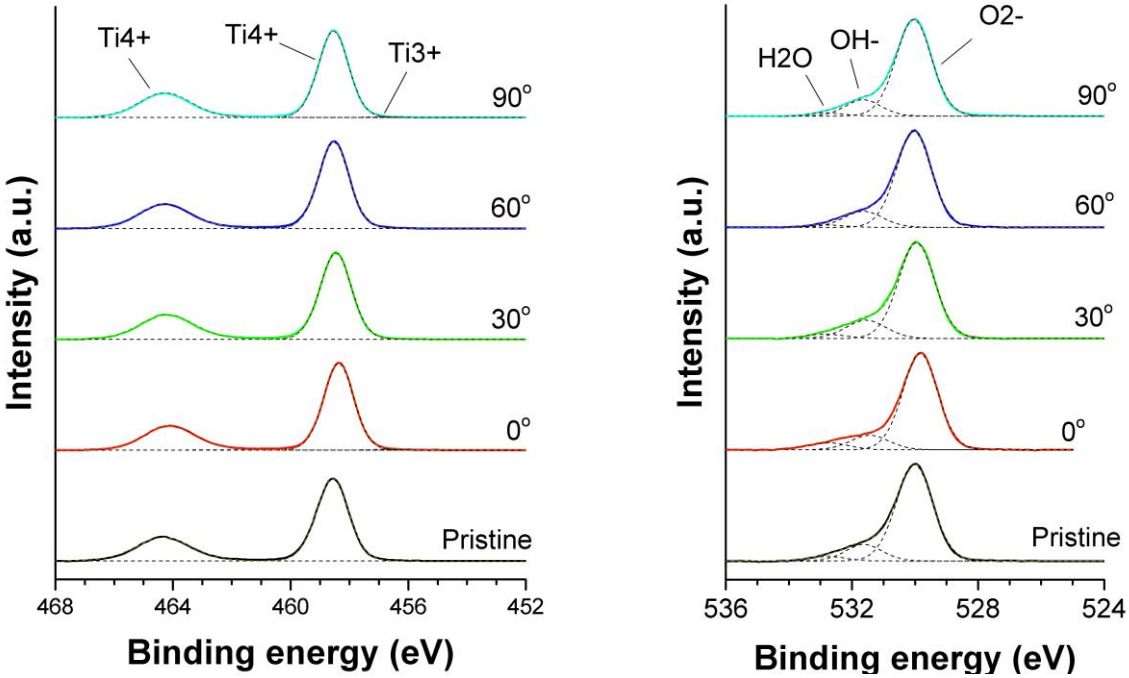

(b) (c)

Figure 6.5 XPS survey, Ti 2p and O 1s core scans of samples after O_2^+ irradiation at E = 500 eV, θ = 60°, φ = 0° – 90°, and Φ = 4.0 x 10^{17} cm^{-2}. The values in the legend correspond to φ.

Table 6.5 Relative atomic concentration of major elements on the surface after O_2^+ irradiation at E = 500 eV, θ = 60º, φ = 0º – 90º, and Φ = 4.0 x 10^{17} cm^{-2}. The values have an accuracy of ~10%.

φ, species	**Atomic percentage of major elements (%)**				**Ratio**	
	C	Ti	O (O^{2-})	O (H_2O + OH^-)	Ti/O	(Ti^{2+}+Ti^{3+})/Ti
Pristine	27.1	20.9	42.6	9.34	0.49	--
0º	40.94	16.4	34.19	8.5	0.48	0.01
30º	32.83	17.59	39.29	10.3	0.45	--
60º	42.54	15.38	34.71	7.4	0.44	--
90º	41.01	15.59	36.04	7.4	0.43	< 0.01

Last, the effect of varying fluence is examined. The irradiation parameters were E = 500 eV, θ = 60º, φ = 0º, and Φ = 2.5 x 10^{17} – 5.0 x 10^{17} cm^{-2}. **Figure 6.6** shows the survey, Ti2p and O1s core regions of the samples irradiated at varying fluence. In general, similar trends are observed compared to the previous section. In the survey spectrum, the main peaks corresponding to C 1s, Ti 2p, O 1s and Ti 2s photoelectron peaks and the O KLL and Ti LMM Auger peaks can still be observed, indicating all the elements remained on the surface. Negligible contamination except organic compounds was observed. In the Ti 2p spectrum the double peak at 458.6 eV and 464.3 eV, corresponding to Ti $2p_{3/2}$ and Ti $2p_{1/2}$ of Ti^{4+} respectively, remained. The binding energies were negligibly shifted (± 0.2 eV). A tiny shoulder corresponding to reduced Ti states was present in some cases only. A deconvolution of the shoulder indicated the presence of a tiny amount of Ti^{3+} and Ti^{2+}. In the O 1s spectrum, a main peak corresponding to O 1s of O^{2-} was still present. The binding energy shifts were also negligible (± 0.2 eV). A small shoulder on the left of the main peak, corresponding to OH^- and physisorbed H_2O, was still present. The intensity of the shoulder changed in some cases. The relative atomic concentrations of the major elements (carbon, oxygen which is bonded to Ti, physisorbed H_2O and OH^- groups on the surface, and Ti) were calculated

and listed in **Table 6.6**. The Ti/O ratio remained essentially unchanged. The amount of carbon, H_2O and OH^- groups sometimes becomes higher than pre-irradiation. The ratio between reduced states of Ti and overall Ti is also listed in **Table 6.6** and found to be ≤ 0.01.

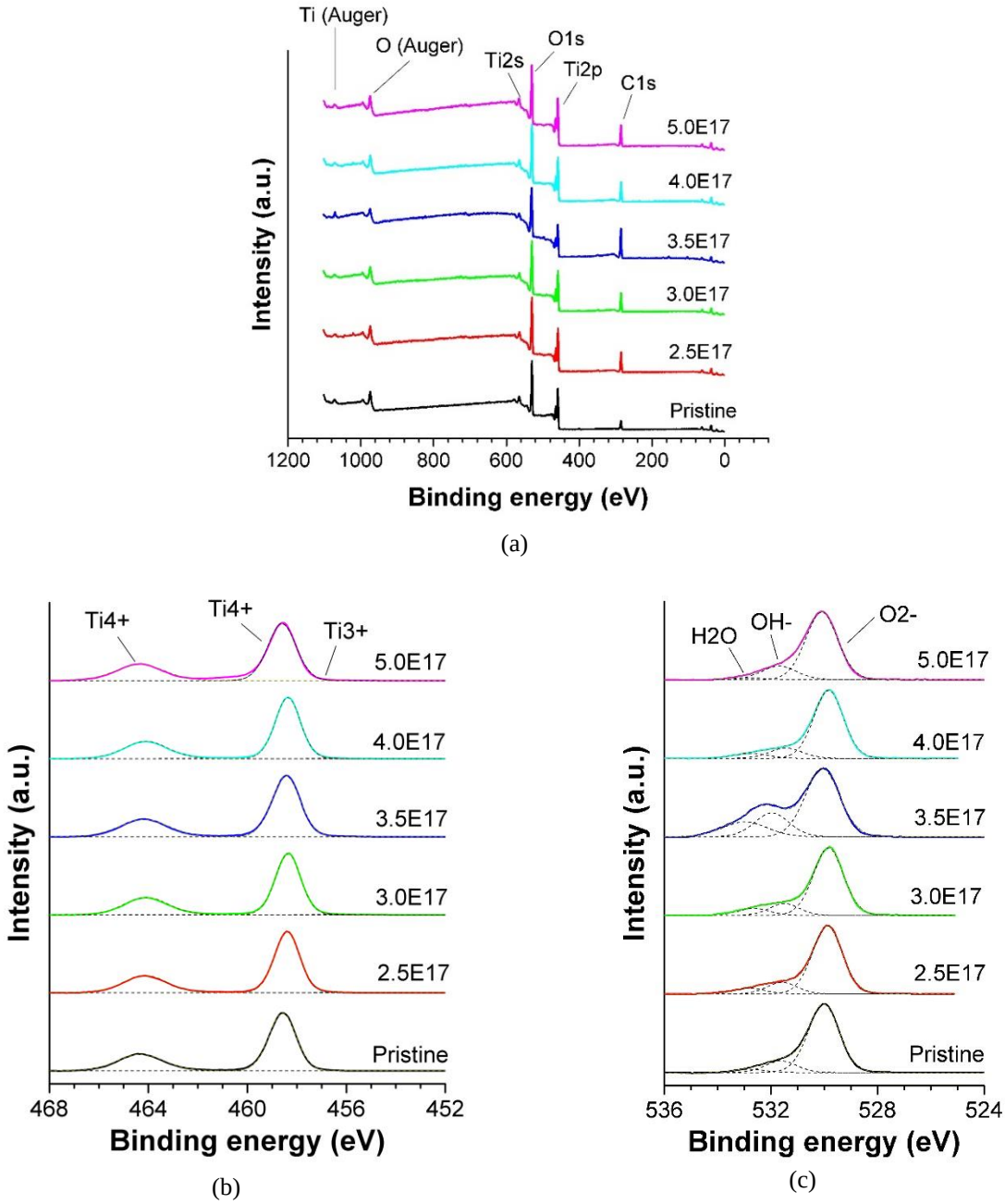

Figure 6.6 XPS survey, Ti 2p and O 1s core scans of samples after O_2^+ irradiation at E = 500 eV, θ = 60°, φ = 0°, and Φ = 5 x 10^{16} – 5 x 10^{17} cm^{-2}. The values in the legend correspond to Φ. A core scan of the sample irradiated at Φ = 5 x 10^{17} cm^{-2} with Ar^+ was not performed due to the nonexistence of Ti peak in the survey scan. All the data were acquired using Kratos.

Table 6.6 Relative atomic concentration of major elements on the surface after O_2^+ irradiation at E = 500 eV, θ = 60°, φ = 0°, and Φ = 2.5 x 10^{17} – 5 x 10^{17} cm^{-2}. The values have an accuracy of ~10%.

Φ ($10^{17}$$cm^{-2}$)	**Atomic percentage of major elements**				**Ratio**	
	C	Ti	O (O^{2-})	O (H_2O + OH^-)	Ti/O	(Ti^{2+}+Ti^{3+})/Ti
Pristine	27.1	20.9	42.6	9.3	0.49	--
2.5	41.7	15.6	33.94	8.7	0.46	0.01
3.0	42.88	15.2	32.73	9.2	0.46	0.01
3.5	54.54	10.1	21.64	13.7	0.47	--
4.0	40.94	16.4	34.19	8.5	0.48	0.01
5.0	40.28	16.29	34.49	9.0	0.47	--

6.3 Discussion and comparison between Ar^+ and O_2^+ irradiation

Several deductions can be made based on the results presented in this chapter. Overall speaking, the changes in surface chemistry due to irradiation under the parameters described in this chapter can be considered minimal. There are slight variations between intensities of certain shoulders and appearance of extra photoelectron peaks, but these do not show any clear correlation to any irradiation parameters. For example, elements such as iron, molybdenum, calcium and so on sometimes appear after irradiation. These elements are probably just contaminants deposited on or implanted into the samples during irradiation due to several reasons including sputtering of sample stage, materials from the grid in the ion gun, and so on. Also, the intensity of the shoulder next to O 1s peak changed in some cases, but no significant trend can be deduced from the changes. Such changes are probably just due to randomly varying amount of physisorbed water and hydroxyl groups from surface contaminants. The concentration of carbon contaminants also varies in

different cases of irradiations, but again it does not indicate any clear correlation to the irradiation parameters. The Ti/O ratio remains essentially unchanged at 0.50 in most cases, after accounting the ~10% error from the software calculation, indicating the surface remains stoichiometric after irradiation. In some cases, the ratio decreases slightly, the lowest being 0.42. This may indicate the surface might be slightly oxygen-enriched, although some of the lower values occur in Ar^+ irradiation. By looking at the ratios and correlating to the irradiation parameters, the decrease does not seem to have any correlation to any of the parameters. The ratio between reduced states of Ti and overall Ti is found to be close to zero in most cases, further indicating all Ti essentially remained in its initial Ti^{4+} state.

Therefore, it seems that ion-beam irradiated surfaces can grow nanopatterns while their surface chemistry remains unchanged. However, this disproves the hypothesis described in the beginning of this chapter. This also contradicts with several literature which finds that Ar^+ and other ions can cause a significant reduction of Ti and even create different compounds on the surface, as mentioned in **Chapter 2.1**. The hypothesis to explain this discrepancy is that the surface undergoes chemical reaction with compounds in the atmosphere such as O_2 and H_2O after the irradiated samples are removed from vacuum, causing the chemically altered surface to revert to its original chemical state. Therefore, *in-situ* XPS characterization was performed on four samples and will be discussed below. The purpose is to eliminate the possible alteration of surface chemistry by the atmosphere. The in-situ data were also compared with ex-situ ones taken after the samples were exposed to the atmosphere for several days.

The first sample was irradiated with Ar^+ at E = 500 eV, $\theta = 60^o$, $\varphi = 0^o$, and $\Phi = 5.0 \times 10^{16}$ cm^{-2}. The Ti 2p and O 1s core spectra are shown in **Figure 6.7**. After irradiation, even though the fluence

is low, a clear shoulder can be seen on the right of the main Ti $2p_{3/2}$ peak, indicating a reduction of certain Ti^{4+} ions due to Ar^+ sputtering. A deconvolution of the shoulder indicates that both Ti^{3+} and Ti^{2+} states exist. The $(Ti^{2+}+Ti^{3+})/Ti$ ratio is found to be 0.26. This agrees with the literature that Ar^+ irradiation reduces Ti^{4+} to lower oxidation states. However, such reduction was restored upon prolonged exposure to the atmosphere, indicated by the disappearance of the shoulder. This agrees with the hypothesis that the surface chemistry is altered by Ar^+ irradiation, but is reversed upon exposure to the atmosphere. The O 1s spectrum shows a decrease in of OH groups and physisorbed H_2O after irradiation, but their concentration increases slightly after exposure to air.

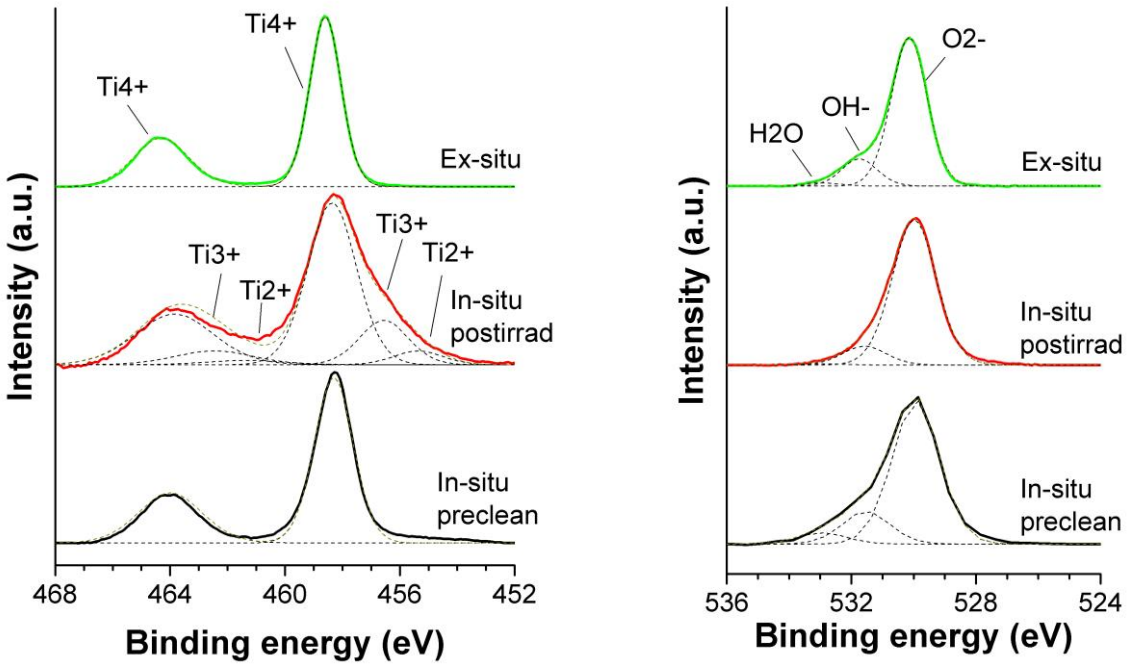

(a) (b)

Figure 6.7 *In-situ* XPS Ti 2p and O 1s core spectra of the sample after Ar^+ irradiation at E = 500 eV, θ = 60°, φ = 0°, and Φ = 5.0 x 10^{16} cm^{-2}. *Ex-situ* results were also included for comparison. The *in-situ* data were acquired in IGNIS, while the *ex-situ* data were acquired in Kratos.

The second sample was irradiated with Ar^+ at E = 500 eV, θ = 60°, φ = 0°, and Φ = 3.0 x 10^{17} cm^{-2}. The Ti 2p and O 1s core spectra are shown in **Figure 6.8**. After irradiation, a clear shoulder can

be seen as well on the right of the main Ti $2p_{3/2}$ peak, indicating a reduction of certain Ti^{4+} ions due to Ar^+ sputtering. A deconvolution of the shoulder indicates that both Ti^{3+} and Ti^{2+} states exist. The $(Ti^{2+}+Ti^{3+})/Ti$ ratio is found to be 0.11. The ratio was lower than the previous case at $\Phi = 5.0 \times 10^{16}$ cm^{-2}, even though the fluence has been increased by almost an order of magnitude. Such reduction is again seen to be restored upon prolonged exposure to the atmosphere, indicated by the disappearance of the shoulder. This also supports with the hypothesis that the surface chemistry is altered by Ar^+ irradiation, but is reversed upon exposure to the atmosphere. The O 1s spectrum shows a decrease in of OH groups and physisorbed H_2O after irradiation, but their concentration increases when exposed to air.

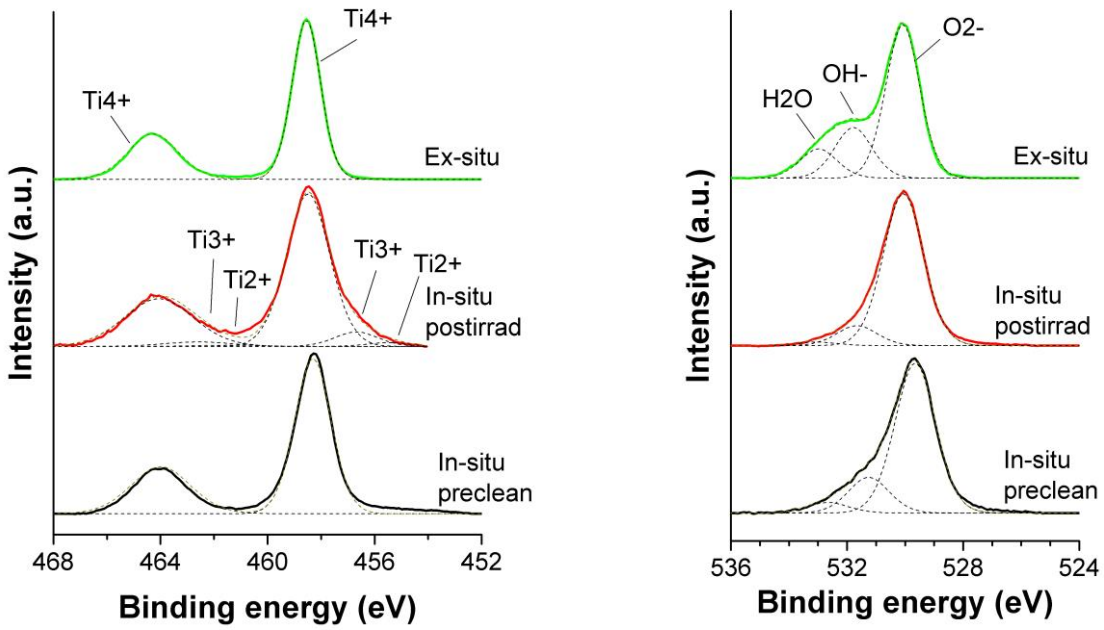

(a) (b)

Figure 6.8 *In-situ* XPS Ti 2p and O 1s core spectra of the sample after Ar^+ irradiation at E = 500 eV, $\theta = 60^o$, $\varphi = 0^o$, and $\Phi = 3.0 \times 10^{17}$ cm^{-2}. *Ex-situ* results were also included for comparison. The *in-situ* data were acquired in IGNIS, while the *ex-situ* data were acquired in Kratos.

The third sample was irradiated with Ar^+ at E = 500 eV, $\theta = 0^o$, $\varphi = 0^o$, and $\Phi = 1.0 \times 10^{18}$ cm^{-2}. The Ti 2p and O 1s core spectra are shown in **Figure 6.9**. The Ti 2p spectrum no longer has two

distinct peaks, but only one large broad peak instead. The shape of such a broad peak somewhat resembles that of Ti_2O_3, which has a broad complex spectrum shown in **Figure 6.10.** [122] Even though the literature claims the sample used to be pure Ti_2O_3, such a complex spectrum probably contains multiple Ti states in addition to Ti^{3+}. A deconvolution of the peak indicates there still exists Ti^{4+} states, although its concentration has decreased significantly. There also exists Ti^{2+} states. The $(Ti^{2+}+Ti^{3+})/Ti$ ratio is found to be almost 0.7. However, the deconvolution is not able to fit the entire peak this time. The peak positions have also shifted by a significant amount, at least ± 0.5 eV. This may indicate additional chemical changes has happened to the surface. This Ti 2p peak is more complex than before, even more complex than the spectra obtained by many other researchers who also performed Ar^+ irradiations on TiO_2. Further experiments at a high fluence and more characterization methods will be needed to determine the surface composition more accurately. After exposure to air, two distinct peaks can be seen again, indicating such reduction is restored. There is a small shoulder characteristic of Ti^{3+} and Ti^{2+}, indicating the surface is not able to restore to its initial chemical state. It is unsure if this restoration will continue further until only Ti^{4+} remains if the sample is allowed to stay in atmosphere for an even longer time, or the reduction is so great it cannot be restored anymore. The O 1s spectrum shows a decrease in of OH groups and physisorbed H_2O after irradiation. Their concentration remains similar after exposure to air.

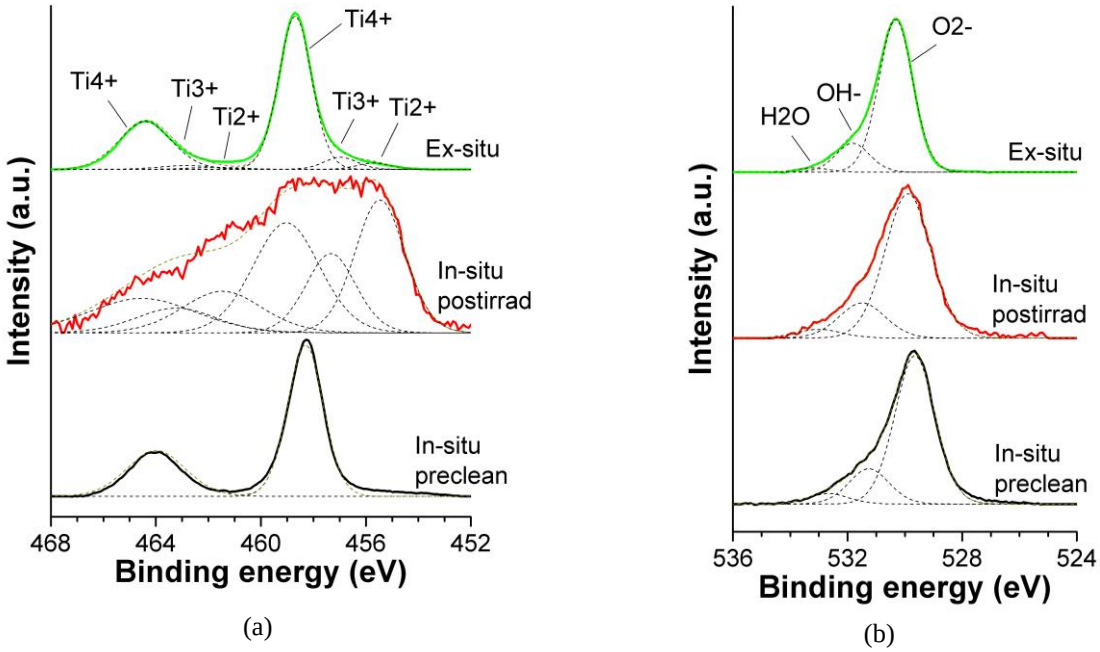

(a) (b)

Figure 6.9 *In-situ* XPS Ti 2p and O 1s core spectra of the sample after Ar^+ irradiation at E = 500 eV, θ = 0º, φ = 0º, and Φ = 1.0 x 10^{18} cm^{-2}. *Ex-situ* results were also included for comparison. The *in-situ* data were acquired in IGNIS, while the *ex-situ* data were acquired in Kratos.

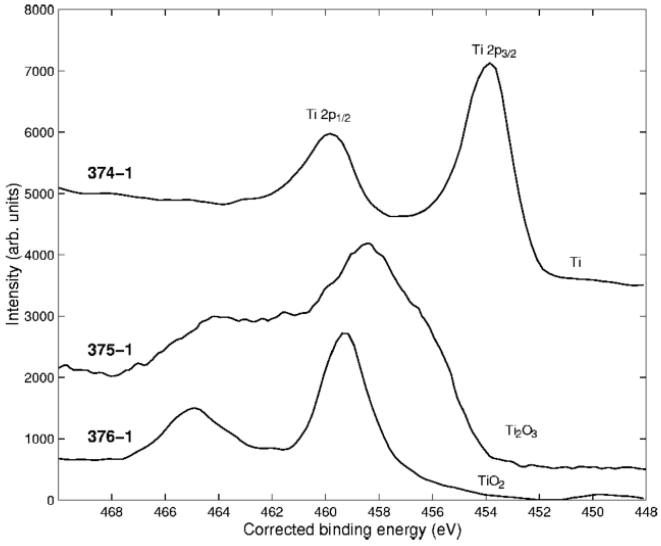

Figure 6.10 Ti_2O_3 Ti 2p spectrum from [122]

The final sample was irradiated with O_2^+ at E = 500 eV, θ = 60º, φ = 0º, and Φ = 4.0 x 10^{17} cm^{-2}. A cleaning step by Ar^+ irradiation at 1000 eV at normal incidence is performed prior to O_2^+

irradiation. This cleaning step lasted for ~ 20 sec, equivalent to a fluence of ~ 3 x 10^{15} cm^{-2}. This is to remove carbon contaminants on the surface before the irradiation. The Ti 2p and O 1s core spectra are shown in **Figure 6.11**. After cleaning, there is a clear shoulder on the right of the main Ti $2p_{3/2}$ peak. This implies Ti^{4+} can be easily reduced to lower oxidation states even when the fluence is very low. However, such reduction is reverted after O_2^+ irradiation, as shown by the absence of the shoulder. A very important implication from this is that the evolution of surface topography is independent of any surface chemistry changes. It is possible to create nanostructures without altering the surface chemistry at all. However, in the case of TiO_2, this is achieved not by using inert ions like Ar^+, but by using reactive O_2^+ ions. This is quite counter-intuitive, but may be explained as follow: Ar^+ sputtering of TiO_2 is known to preferentially sputter oxygen, causing the surface to become oxygen-deficient, and thus TiO_2 to be reduced to Ti_2O_3 or even TiO. [41,83,92] While O_2^+ should preferentially sputter oxygen too, it also replaces the removed oxygen atoms. The replacement rate seems to balance out the sputter rate of oxygen, so that the surface remains to remain entirely TiO_2. This hypothesis might be further supported by the reversibility of the reduced Ti states due to Ar^+ irradiation after the sample is exposed to the atmosphere containing oxygen for sufficient time. The reversibility has also been seen in other literature. [123] There are no noticeable chemistry changes after the sample is exposed to air, which is obvious since the surface chemistry has already been the same as before irradiation. Note that there appears to be a shoulder on the right of the Ti^{4+} $2p_{3/2}$ peak of the *ex-situ* sample. This shoulder has never been seen in other samples, so it is uncertain if this represents any chemistry changes or just measurement errors. The O 1s spectrum shows a decrease in of OH groups and physisorbed H_2O after irradiation, but their concentration increases when exposed to air.

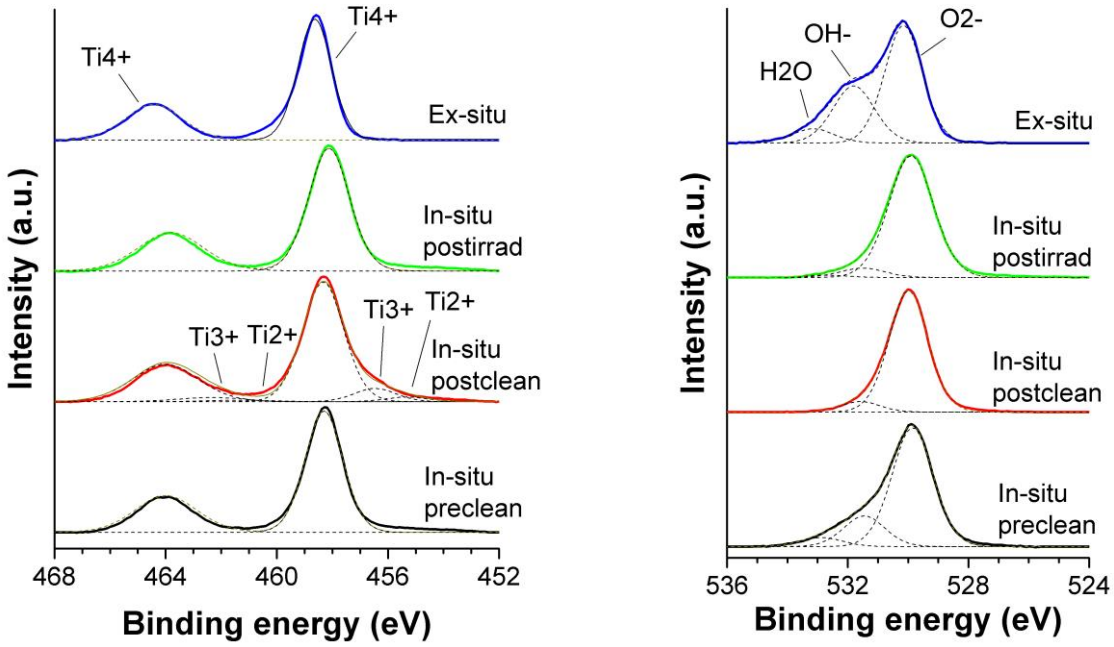

(a) (b)

Figure 6.11 *In-situ* XPS Ti 2p and O 1s core spectra of the sample after O_2^+ irradiation at E = 500 eV, θ = 60°, φ = 0°, and Φ = 4.0 x 10^{17} cm^{-2}. *Ex-situ* results were also included for comparison. The *in-situ* data were acquired in IGNIS, while the *ex-situ* data were acquired in Kratos.

In conclusion, the evolution of surface topography and growth of nanostructures have happened independent of surface chemistry. For TiO_2 this can be achieved by O_2^+ irradiation. Although Ar^+ irradiation reduces TiO_2 to its reduced states, such reduction is reversible and is restored upon prolonged exposure to atmosphere. Therefore, the hypothesis described in the beginning of this chapter should be modified as follow: Ar^+ ions, even though inert, modifies TiO_2 to its reduced compounds Ti_2O_3 and TiO through preferential sputtering of oxygen, and these compounds is unstable and will revert to TiO_2 upon exposure to atmosphere. O_2^+ ions, even though reactive, does not modify the surface chemistry due to continuous replacement of preferentially sputtered oxygen during irradiation.

CHAPTER 7: OPTICAL RESPONSE CHANGES AFTER ION IRRADIATION

This chapter covers the optical response changes due to ion-beam irradiation under different parameters. The goal of this chapter is to address the fourth hypothesis: ion irradiation may cause changes in the optical response of the PC, due to potential modification of the surface topography and film properties. As already illustrated in **Chapter 5**, significant changes in the surface topography and film thickness have occurred due to irradiation. Therefore, this chapter aims to examine the changes in the optical responses and attempt to correlate them to the topography. Optical response changes after irradiation is quantified by measuring the transmission spectrum. In this chapter, changes due to Ar^+ and O_2^+ irradiation will be discussed separately in their respective subsection. A comparison between them will be made in the end.

7.1 Ar^+ irradiation

Effects of varying energies, incident angle θ and fluence Φ are examined in the case of Ar^+ irradiation. First, effect of varying energies will be presented. **Figure 7.1** shows the transmission spectra of the samples irradiated at varying energies. The main aspects of interest here is the PWV position, the shape and width of the peak, and the peak intensity. For the pristine sample, a strong and sharp peak appears at 861 nm. The peak appears to be asymmetric with a broad tail towards the higher wavelength. After irradiation, at Φ = LF there was a slight blue shift when $E \geq 500$ eV. The shift at E = 1000 eV was slightly larger than at E = 500 eV. The peaks at both energies still maintained its original shape. At E = 250 eV, the peak was red-shifted by a little. On the other hand, at Φ = HF a major blue shift and peak broadening can be seen in all cases, although the peaks

were still fairly distinguishable. At E ≥ 500 eV the peaks became much weaker, and they lost the broad tail.

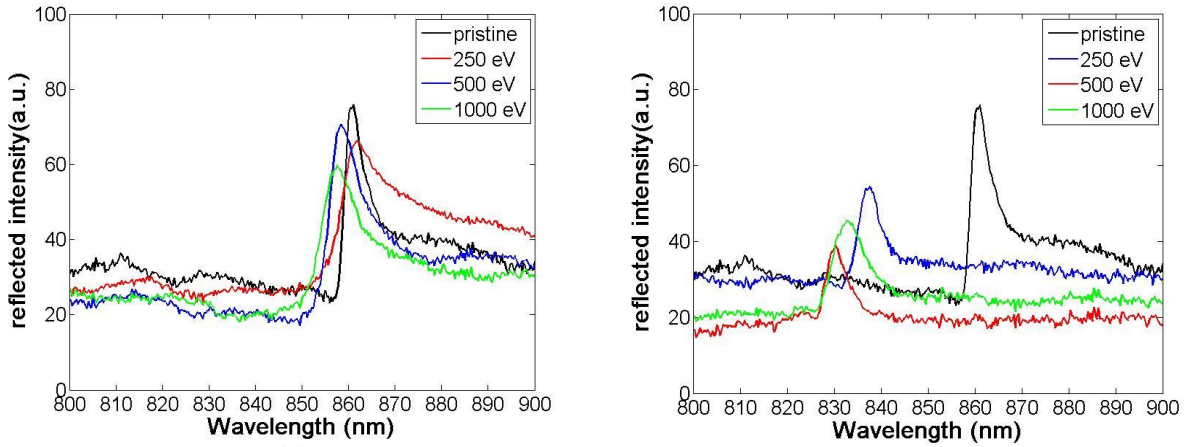

Figure 7.1 Transmission spectra of samples after Ar^+ irradiation at E = 250 – 1000 eV, θ = 0°, φ = 0°, and Φ = (a) 5 x 10^{16} cm^{-2} (LF) and (b) 1 x 10^{18} cm^{-2} (HF). A TM polarized white light was used to illuminate the surface.

Next, effects of varying incident angle θ will be presented. **Figure 7.2** shows the transmission spectra of the samples irradiated at varying θ. In the case of Ar^+ irradiation, a significant blue shift can be seen, the shift being higher with increasing incident angle. The peak became wider and its intensity decreased. At θ = 60° the shape of the peak became more symmetric.

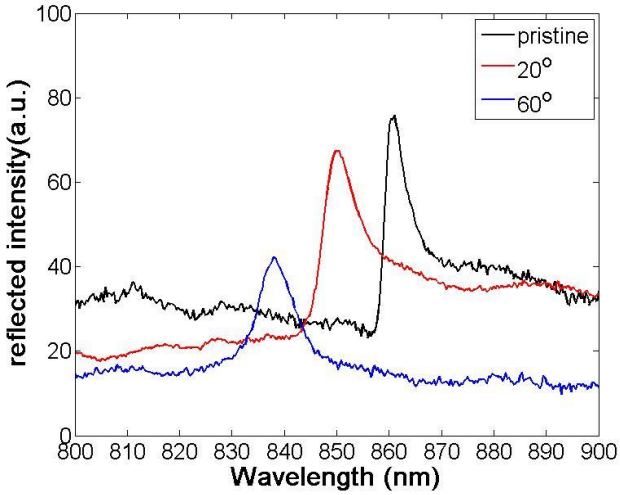

Figure 7.2 Transmission spectra of samples after (a) Ar^+, (b) O_2^+ irradiation at E = 500 eV, θ = 0° – 60°, φ = 0°, and Φ = 2.5 x 10^{17} cm^{-2}. A TM polarized white light was used to illuminate the surface.

Last, effects of varying fluence will be presented. **Figure 7.3** shows the transmission spectra of the samples irradiated at varying fluence. Same as before, a blue shift can be seen in all irradiated cases. The magnitude of the shift generally increased with increasing fluence. Especially when $\Phi \geq 2.5 \times 10^{17}$ cm^{-2} the irradiated samples showed a much weaker, broader and more symmetric peak. The peak becomes even weaker when $\Phi = 3.0 \times 10^{17}$ cm^{-2}, and disappeared when $\Phi \geq 3.5 \times 10^{17}$ cm^{-2}. The film thicknesses at $\Phi = 3.0 \times 10^{17}$ cm^{-2} and $\Phi = 3.5 \times 10^{17}$ cm^{-2} were found to be 42 ± 2.6 nm and 19 ± 2.2 nm respectively. The transition from a sharp, narrow, asymmetric peak to a weak, broad, symmetric peak appears to begin somewhere between $\Phi = 2.0$ - 2.5×10^{17} cm^{-2}. The film thicknesses at $\Phi = 2.0 \times 10^{17}$ cm^{-2} and $\Phi = 2.5 \times 10^{17}$ cm^{-2} were found to be nm and 56 ± 2.0 nm respectively.

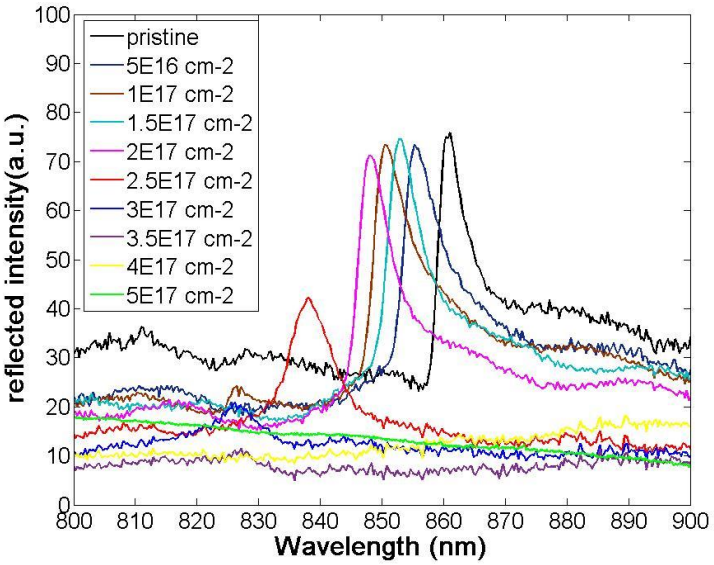

Figure 7.3 Transmission spectra of samples after (a) Ar^+, (b) O_2^+ irradiation at E = 500 eV, $\theta = 60^o$, $\varphi = 0^o$, and $\Phi = 5 \times 10^{16} – 5 \times 10^{17}$ cm^{-2}. A TM polarized white light was used to illuminate the surface. Measurement of the sample irradiated at $\Phi = 5 \times 10^{17}$ cm^{-2} with Ar^+ was not performed due to the nonexistence of TiO_2 film.

7.2 O_2^+ irradiation

Figure 7.4 shows the transmission spectra of the irradiated samples. In the case of O_2^+ irradiation, a blue shift can also be seen in the case of $\theta = 60^o$ but not $\theta = 20^o$, and the magnitude of the shift is much less than in Ar^+ irradiation. The peak retained its original shape and width, even though nanostructures appeared at $\theta = 60^o$.

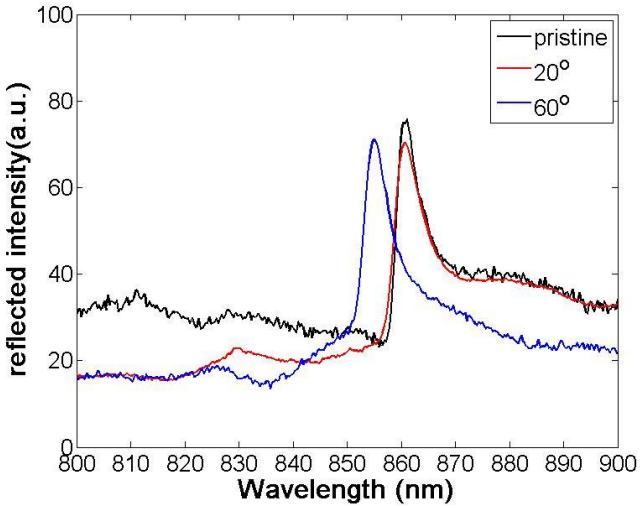

Figure 7.4 Transmission spectra of samples after O_2^+ irradiation at E = 500 eV, $\theta = 0^o - 60^o$, $\varphi = 0^o$, and $\Phi = 2.5 \times 10^{17}$ cm^{-2}. A TM polarized white light was used to illuminate the surface.

Figure 7.5 shows the transmission spectra of the samples irradiated at varying φ. Same as before, a blue shift can be seen in all irradiated cases. Surprisingly however, the blue shift seems to be the most in the case of $\varphi = 30^o$. The shift is very similar between $\varphi = 0^o$ and $\varphi = 90^o$. Moreover, in the case of $\varphi = 30^o$ an additional weaker resonant peak appeared at 891.6 nm. This is surprising since no other sample has shown an additional resonance.

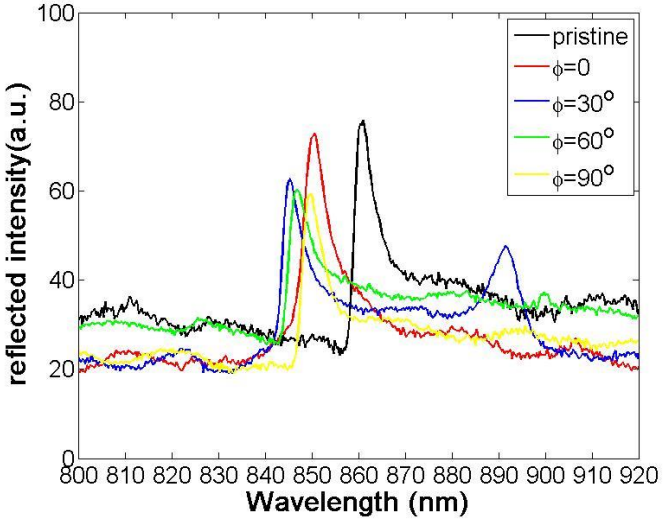

Figure 7.5 Transmission spectra of samples after O_2^+ irradiation at E = 500 eV, θ = 60°, φ = 0° – 90°, and Φ = 4.0 x 10^{17} cm^{-2}. A TM polarized white light was used to illuminate the surface.

Figure 7.6 shows the transmission spectra of the samples irradiated at varying fluence. Same as before, a blue shift can be seen in all irradiated cases. The magnitude of the shift generally increased with increasing fluence, same as in the case of Ar^+ irradiation. However, in the case of O_2^+ irradiation, the blue shift is much smaller, and the resonant peaks are able to retain its original shape, width and intensity even at the highest fluence.

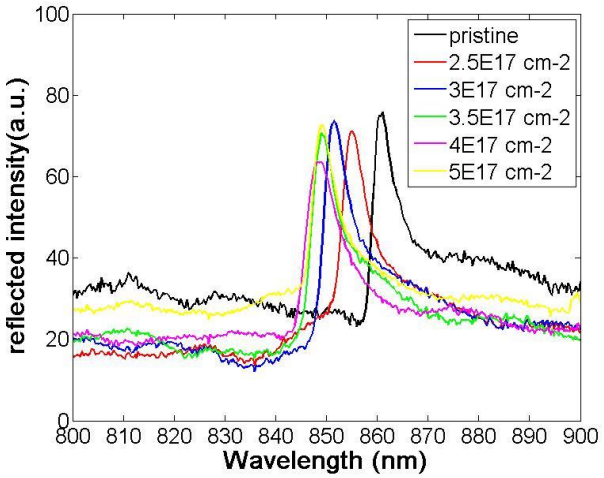

Figure 7.6 Transmission spectra of samples after (a) Ar^+, (b) O_2^+ irradiation at E = 500 eV, θ = 60°, φ = 0°, and Φ = 5 x 10^{16} – 5 x 10^{17} cm^{-2}. A TM polarized white light was used to illuminate the surface. Measurement of the sample irradiated at Φ = 5 x 10^{17} cm^{-2} with Ar^+ was not performed due to the nonexistence of TiO_2 film.

7.3 Comparison between Ar^+ and O_2^+ irradiaton

Before analyzing the results, it is necessary to explain the principle behind the observed PWV shift. The PWV position shifts when there is a change in the thickness of the film. For example, a blue shift (a shift to a lower wavelength) will occur if the thickness of the film decreases, most likely due to sputtering in the case of this research, whereas a red shift (a shift to a higher wavelength) will occur if the thickness of the film increases or additional substance, e.g. target proteins, is deposited onto the surface. This is also the working principle of label-free PC biosensors.

It is now possible to explain the PWV shifts observed in different cases of irradiation. At low fluence, little blue shift is observed, indicating the film was barely sputtered at all. There is one case in which the peak was red-shifted by a little. This is when the ion energy is at 250 eV. A possible explanation is that the sputtering was little compared to the significant amount of contaminants deposited onto the surface due to the low energy, as mentioned in **Chapter 6**, and hence the contamination layer may have actually increased the film thickness more than the decrease due to sputtering. At high fluence, a significant blue shift is observed, the magnitude of the shift generally increasing with increasing fluence. This indicates a considerable amount of the film was removed, and the dependency is expected since the amount of TiO_2 sputtered should increase with irradiation time. In few cases the dependency is the opposite (e.g. O_2^+ irradiation at $\Phi = 3.5 \times 10^{17} – 5.0 \times 10^{17}$ cm^{-2}, their respective spectra shown in **Figure 7.6**.) This might just be due to experimental error during irradiation, since it is observed that the ion flux often fluctuates during the experiment, which causes the actual fluence to deviate from the theoretical fluence. Especially for Ar^+ irradiation, the peak becomes much broader and weaker and eventually disappears when above a critical fluence ($\Phi = 2.5 \times 10^{17}$ cm^{-2} at $\theta = 60^o$) The broadening and

weakening of the peak may be caused by several reasons. One possibility can be the film becomes amorphous and becomes less effective in reflecting lights. Future experiments on determining the crystal phase before and after irradiation is needed to confirm this hypothesis. Another possibility may be the removal of films in the trenches causing the sample to be less effective in reflecting lights. This could explain why the peaks of Ar^+ irradiated samples above the critical fluence, at which the film in the trenches have been removed, change their shapes, while O_2^+ irradiated ones do not. The disappearance of the peak implies the film becomes too thin to be able to confine and reflect any resonant waves. It is also observed that the blue shift is greater for Ar^+ irradiation than O_2^+ irradiation, which is obvious since the sputtering rate by Ar^+ is much higher than by O_2^+, as already shown in **Figure 5.18** in **Chapter 5**. The peaks also retain a much better shape and intensity even at a high fluence in the case of O_2^+ irradiation. Moreover, the blue shift is greater at a larger incident angle, indicating sputtering rate of TiO_2 is higher at a larger angle.

The most interesting observation is the PWV shifts happened after irradiation at varying φ shown in **Figure 7.5**. The PWV shift at $\varphi = 30^o$, $\varphi = 60^o$ and $\varphi = 90^o$ are all lower than at $\varphi = 0^o$, with $\varphi = 30^o$ one being largest and $\varphi = 90^o$ being closest to the $\varphi = 0^o$ one. For $\varphi = 60^o$ and $\varphi = 90^o$ samples, they were irradiated at the same time, and hence the major error due to fluence fluctuations between experiments has already been taken out. This could imply there is a dependence of the sputtering rate on the ion beam orientation on such non-flat surface with ridges and trenches and sharp edges. The rate seems larger when the beam is neither parallel nor perpendicular to the grating vector, and is the largest when φ is close to 30^o. Especially in the case of $\varphi = 30^o$, an additional resonance at a higher wavelength is observed. Looking back at its SEM image in **Figure 5.11 (b)**, there does not seem to have any changes to the grating shape, although w has decreased by almost 20 nm. As the optical properties of photonic crystal depends on the grating shape and

size, a decrease in w may be related to the additional resonance, although it is not certain how they are related. More irradiations at orientations close to $\varphi = 30^{o}$ will be needed to confirm the presence of two resonances is real and not due to error.

In general, these results have supported the hypothesis described in the beginning of this chapter. The PWV position is dependent on the irradiation parameters, primarily in the way of depending on the change of film thickness resulted from varying irradiation parameters. It is unclear if the nanostructures, such as periodic ripples, also affects the PWV positions since the theory of photonic crystals does not account for small nanostructures on the surface. However, it is reasonable to guess that these ripples do not have any effect at all, because its periodicity is at least two orders of magnitude smaller than the PWV wavelength.

Although different PWV shifts are observed under different irradiation parameters, in terms of applications as label-free biosensors, these shifts should not be a problem, as long as the peaks are sharp enough to be distinguishable from the background signal. This is because the relative PWV shift, instead of the absolute PWV, is the indicator when performing target analyte adsorptions onto the sensor surface. Moreover, additional layers of TiO_2 can be deposited onto the surface before, during or after irradiations to ensure the post-irradiated samples have a sufficiently thick film. The additional resonant peak created at $\varphi = 30^{o}$ is very surprising if real, and can be of use in other biosensors, for example fluorescent biosensors in which more than one excitation wavelength may be used to excite more than one type of fluorescent dyes to image different target analytes. Furthermore, it may also be useful in optical filters to filter more than one wavelength and possibly many other optical applications.

CHAPTER 8: PROTEIN ADHESION TESTS

This chapter covers the effects of surface topography and chemistry changes due to ion irradiation on the amount of protein adsorbed. The goal of this chapter is to address the final hypothesis stated in **Chapter 3**: the induced nanostructures are capable of providing additional surface area, and hence increasing the amount of protein adsorbed on the surface and thus improving sensor sensitivity up to the magnitude achieved by GLAD (4 times as stated in **Chapter 3.1**). As already illustrated in **Chapter 5**, there is clearly an increase in surface area due to ripples induced by irradiation. Therefore, this chapter aims to examine how such increase can correlate to the amount of proteins adsorbed. Several samples with well-defined nanoripples are chosen for this experiment. The amount of adsorbed proteins is measured by measuring the PWV shift in the transmission spectra before and after adsorption. XPS is also performed to verify the presence of these proteins and functional linkers by observing the presence of N 1s and Si 2p peaks.

8.1 Samples used

The samples used for biological testing are listed in **Table 8.1**. Several irradiation parameters are fixed: E = 500 eV, $\theta = 60^{o}$, and $\phi = 0^{o}$. For convenience, a short name is given to each sample so that they can be referred to more easily in the following sections. In addition, the sample names listed in **Table 8.1** will be followed by a name describing the type of biological testing. The naming convention is described in **Table 8.2**. For example, a chemisorption protein adhesion test on a sample irradiated with Ar^{+} at E = 500 eV, $\theta = 60^{o}$, $\phi = 0^{o}$, and fluence = 1.0×10^{17} cm^{-2} will have a name Ar_1_biotin.

Table 8.1 Naming conventions and irradiation parameters of samples used for protein adhesion tests. The fixed parameters are E = 500 eV, $\theta = 60^{o}$, and $\phi = 0^{o}$.

Sample name	Ion species	Fluence (cm^{-2})
C	Control, no irradiations	
Ar_1	Ar^{+}	1.0×10^{17}
Ar_2.5	Ar^{+}	2.5×10^{17}
O2_2.5	O_2^{+}	2.5×10^{17}
O2_4	O_2^{+}	4.0×10^{17}

Table 8.2 Naming conventions for biological tests. X refers to samples listed in **Table 8.1**.

Sample	Adsorption type	Adsorption target
X_cBSA	Chemisorption	PVA-GA-BSA
X_biotin	Chemisorption	APTES-PEG-biotin-SVA & APTES-mPEG-SVA
X_pBSA	Physisorption	BSA
X_V12	Physisorption	Vitamin B12

8.2 XPS results

Figure 8.1 shows the XPS survey scans of samples listed in **Table 8.1** after undergoing the biological tests listed in **Table 8.2**. From the survey spectra N 1s peaks can be clearly observed in all cases, implying the presence of proteins on the surfaces. In addition, in the spectra for biotin adsorption in F (a), Si 2p can be observed as well. The presence of Si 2p is due to the presence of APTES. For pBSA and V12 adsorption, a sharp Na 1s peak and and some small peaks in the lower binding energy region were present. These peaks were due to the presence of PBS, the solvent

used for the proteins that contains sodium, potassium and phosphate salts. The atomic percentages of nitrogen were listed in **Table 8.3** to estimate the relative amount of proteins based on nitrogen content across samples and adsorption tests. Silicon percentage for biotin-adsorbed samples were also listed to estimate the relative amount of APTES. In the same table, the theoretical number of nitrogen atoms per adsorbed molecule is also listed as a comparison to the measured nitrogen content. Such comparison will be performed in the discussion section at the end of this chapter. When comparing across the different adsorption procedures, the surface nitrogen content due to pBSA was significantly larger than the rest of the adsorption tests in general. The nitrogen percentage due to V12 adsorprtion was the smallest, although it was close to that due to biotin chemisorption. On the other hand, when comparing across different samples, results varied among different adhesion tests. In biotin adhesion, sample Ar_2.5 had the most nitrogen on the surface by percentage. All irradiated samples had a slightly higher nitrogen percentage than the control sample. In pBSA adsorption, sample Ar_1 had the most nitrogen on the surface. Sample O2_2.5 had a particularly low nitrogen percentage. In V12 adsorption, sample O2_4 had the most nitrogen on the surface. All irradiated samples had a slightly higher nitrogen percentage than the control sample as well.

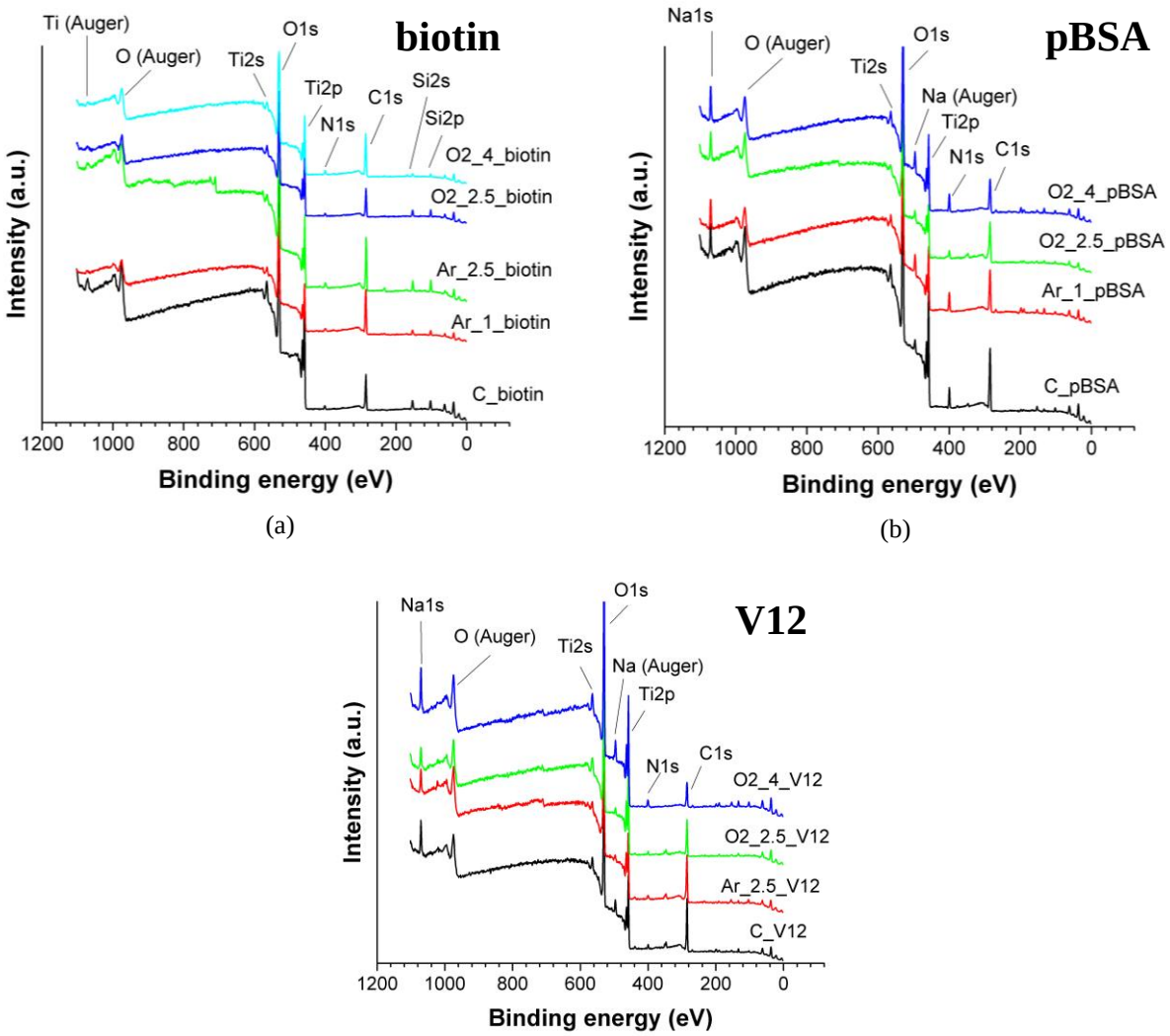

Figure 8.1 XPS survey spectra of samples listed in **Table 8.1** after undergoing the protein adhesion tests listed in **Table 8.2**.

Table 8.3 Nitrogen and silicon atomic percentages on sample surfaces after protein adhesion tests.

Adsorption type	Sample	Atomic percentage (%)		# of N atoms per adsorbed molecule
		N	Si	
Chemisorption (biotin)	C_biotin	1.32	9.53	2-6*
	Ar_1_biotin	2.13	2.93	2-6*
	Ar_2.5_biotin	3.08	6.39	2-6*
	O2_2.5_biotin	2.08	6.97	2-6*
	O2_4_biotin	2.44	2.57	2-6*
Physisorption (pBSA)	C_pBSA	5.32	--	>580**
	Ar_1_pBSA	8.22	--	>580**
	O2_2.5_pBSA	2.87	--	>580**
	O2_4_pBSA	7.47	--	>580**
Physisorption (V12)	C_V12	1.35	--	14
	Ar_2.5_ V12	2.16	--	14
	O2_2.5_ V12	1.56	--	14
	O2_4_ V12	3.50	--	14

* The exact number depends on if the adsorbed molecule is APTES-PEG-SVA-biotin (6 N atoms/molecule) or APTES-mPEG-SVA (2 N atoms/molecule) The ratio of adsorbed amount between them is not determined since the number of N atoms per molecule is considerably smaller than others.
** The exact formula for BSA is not available, but it is known each BSA has about 583 amino acids, and each amino acid has at least one N atom. Therefore, each BSA molecule should have at least 580 N atoms.

8.3 PWV shift

First, a PWV shift was measured before and after O_2 plasma cleaning using a pristine test sample to examine any changes due to possible film sputtering by the plasma. No observable PWV shift was seen, so it is assumed O_2 plasma cleaning did not have any effect on the film thickness. Next, **Table 8.4** shows the PWV shifts of samples listed in **Table 8.1** after undergoing the biological tests listed in **Table 8.2**. A positive shift means the presence of adsorbed proteins. Comparing across the different adsorption procedures, the shifts due to cBSA was significantly larger than the rest of the adsorption tests in general. This is followed by pBSA and V12. Biotin adsorprtion caused the smallest shift. On the other hand, when comparing across different samples, again

results varied among different adhesion tests. In cBSA adsorption, control sample showed a significantly larger PWV shift than others, indicating a higher quantity of BSA chemisorbed on the surface. Sample O2_2.5 showed the smallest shift. In biotin adhesion, sample Ar_1 and O2_4 showed a larger shift than the control sample, while the other two samples showed negative shifts. In pBSA adsorption, only sample O2_4 showed a larger shift than the control sample. Sample Ar_2.5 showed a negative shift. In V12 adsorption, only sample O2_4 showed a slightly larger shift than the control sample. Sample Ar_2.5 showed a negative shift. In cases where a negative shift was observed, the reason is unknown.

Table 8.4 PWV shifts after protein adhesion tests.

Adsorption type	Sample	ΔPWV (nm)
Chemisorption (cBSA)	C_cBSA	+13.3
	Ar_2.5_cBSA	+10.9
	O2_2.5_cBSA	+2.5
Chemisorption (biotin)	C_biotin	+0.6
	Ar_1_biotin	+2.3
	Ar_2.5_biotin	-3.2
	O2_2.5_biotin	-0.6
	O2_4_biotin	+1.6
Physisorption (pBSA)	C_pBSA	+2.2
	Ar_1_pBSA	+0.0
	Ar_2.5_pBSA	-4.5
	O2_2.5_pBSA	+0.9
	O2_4_pBSA	+2.6
Physisorption (V12)	C_V12	+1.5
	Ar_2.5_ V12	-3.8
	O2_2.5_ V12	+1.3
	O2_4_ V12	+1.9

8.4 Discussion

In general, XPS data showed the presence of nitrogen elements on all samples, even in those samples showing zero or negative PWV shifts. Since XPS should be more surface sensitive and not affected by the material and optical properties of the film, it is reasonable to assume based on XPS data that proteins were successfully adsorbed onto all sample surfaces.

When comparing the amount of adsorbed molecules in terms of nitrogen content on the surface across different biological tests, the nitrogen content on pBSA samples seem to be the largest, even though the difference between tests is not very significant, given the error in quantification of atomic percentages can be as high as 10%. To make sense of the nitrogen content, one may try to relate this to how much nitrogen atom each test molecule theoretically has. From **Table 8.3**, it is clear that BSA molecules have the largest number of nitrogen atoms per molecule, while APTES-PEG-biotin and V12 have similar number of nitrogen atoms per molecule. Therefore, this is clearly one explanation of the difference of nitrogen percentage on sample surfaces among different protein adhesion tests.

When comparing the amount of adsorbed molecules in terms of PWV shifts across different biological tests instead, it is clear that chemisorption of BSA causes the largest PWV shift. This is probably due to the fact that the molecules, both the linkers and targets, used in cBSA test are the largest among all the tests. For the linkers, PVA is a bulky polymer with a molecular weight of around 25000 g/mol, while APTES is a much smaller and simpler molecule with much lighter molecular weight of 221.37 g/mol. On the other hand, for the targets, BSA is also a large globular molecule with a molecular weight of 66.5 kDa (1 Da = 1 g/mol), while both biotin and vitamin

B12 are much smaller molecules with molecular weights of 244.31 g/mol and 1355.37 g/mol. These may imply that PVA and BSA form thicker adsorption layers on the samples due to their sizes, leading to a larger PWV shift than seen in other biological tests. It is also possible that the surface favors the adsorption of PVA over other molecules, but since there is little literature comparing the affinity of PVA on TiO_2 with other molecules, more experiments will be needed to testify this.

To compare the PWV shift and nitrogen content across different samples instead, and to examine the hypothesis described at the beginning of this chapter, an examination of their relation to the surface topography is performed. Specifically, these two quantities are correlated to the increase in surface area as well as the spacing of the ripples. The increase in surface area directly affects the amount of available sites for adsorption, while the spacing of the ripples may affect how well the adsorbed molecules' can utilize the additional surface area and whether the molecules sit in between ripples or simply at the top of the structures. Both the PWV shift and atomic percentages of nitrogen are plotted against the percentage increase in surface area due to irradiation-induced nanostructures in **Figure 8.2**. These quantities are also plotted against ripple period in the same figure. In general, no clear trend can be observed. In cases of biotin chemisorption and V12 physisorption, XPS results indicates that the nitrogen content on all irradiated surfaces might be higher than the control surface. There is no clear trend of its dependence on either the ripple periodicity or surface area, however. On the other hand, In the case of pBSA adsorption, the data points seem to be randomly distributed. It is not possible to observe any trends of both PWV shift and surface nitrogen content as functions of either ripple periodicity or increase in surface area. Moreover, the trends shown from XPS and transmission results do not match with each other. It is thus difficult to determine the true changes in the amount of protein adsorbed on the surfaces.

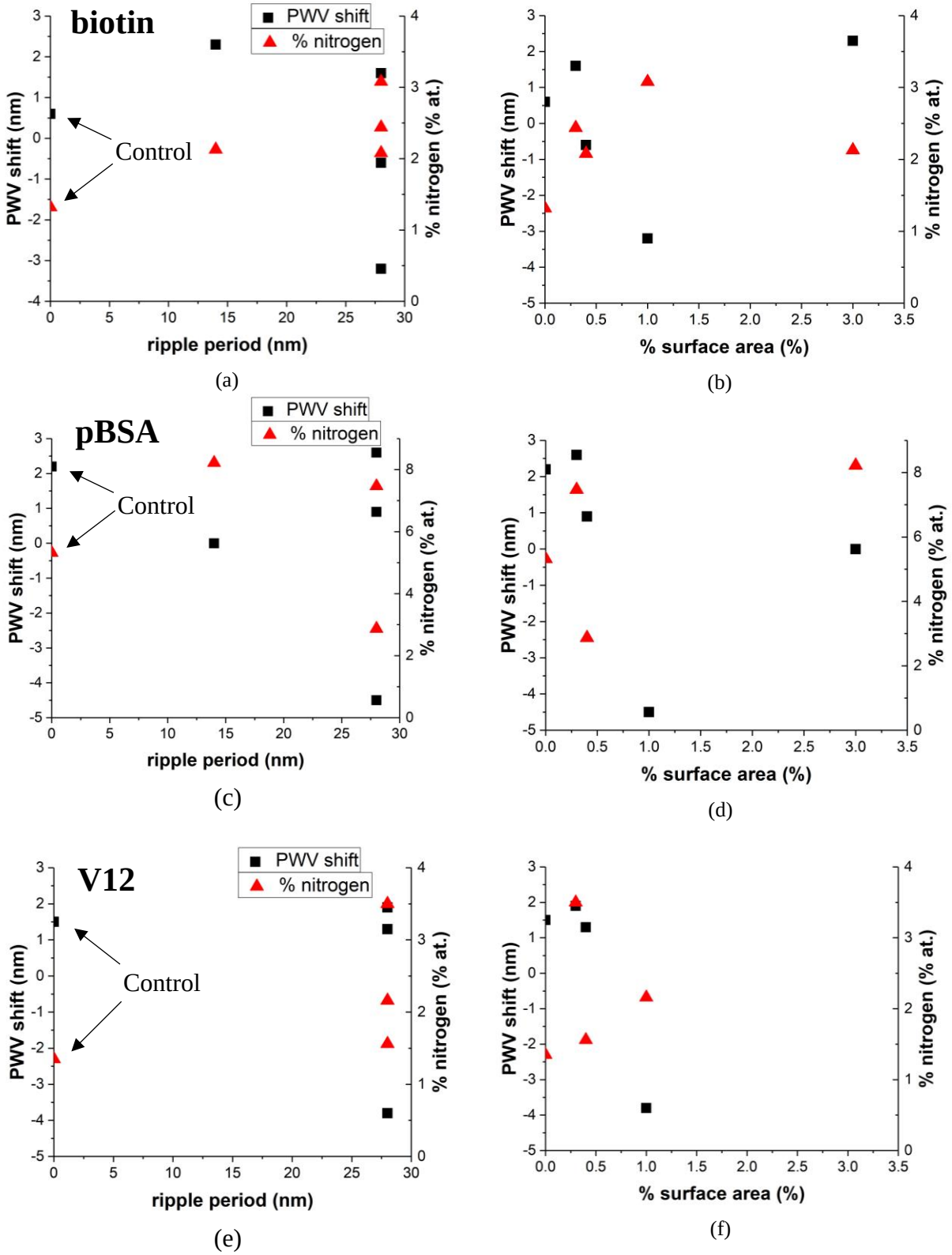

Figure 8.2 PWV shift and amount of nitrogen on surfaces after protein adhesion tests as a function of ripple period and increase in surface area. Data points at ripple period = 0 nm in (a), (c), (e) represent protein adhesion on control samples.

To summarize, it is not able to deduce if the hypothesis addressed at the beginning of this chapter is true or not. Both XPS and transmission results showed no clear trends of the amount of proteins adsorbed on surfaces as functions of separation of nanostructures and increase in surface area due to these structures. In cases of biotin chemisorption and V12 physisorption, it is observed the nitrogen percentage on irradiated surfaces is slightly higher than non-irradiated surfaces, but the PWV shifts showed no clear dependence. In the case of BSA physisorption, it is not able to draw any conclusions of whether irradiated surfaces caused an increase in the amount of adsorbed proteins, due to a relatively random distribution of data points for both PWV shift and surface nitrogen atomic percentages. Moreover, the trends shown from XPS and transmission results do not match with each other. Therefore, these experiments need to be repeated in the future to average out the data and hopefully observe more insightful trends. More samples with different ripple periodicity and surface area will also be needed.

CHAPTER 9: CONCLUSIONS & FUTURE WORK

9.1 Conclusions

A systematic study of the effect of ion-beam irradiation on the surface topography, chemistry and optical transmission property of titanium dioxide (TiO_2) thin film coated on a non-flat polymer-based photonic crystal biosensor with one-dimensional rectangular diffraction gratings, with the goal to improve the biosensor sensitivity up to the magnitude achieved by growing nanorods by glancing angle deposition (GLAD) (~4x) increase in the amount of proteins adsorbed onto the sensor), was performed. In this study, five ion-beam parameters, i.e. ion species, energy (E), incident angle (θ), ion beam orientation (φ) relative to the diffraction gratings, and fluence (Φ), were varied.

It was found that ion-beam irradiation was able to induce topographical changes and growth of nanostructured ripples while keeping the surface chemistry unchanged. The topographical changes depended on the irradiation conditions, as well as the position on the surface. It was observed that Ar^+ irradiation at normal incidence at a high fluence of 1×10^{18} cm^{-2} results in the edges of the ridges of the diffraction gratings having an entirely different topography from the center of those ridges. Roughening and random nanostructures appeared along the edges, while smoothening occurred at the center surface. This phenomenon is surprising, especially since the majority of literature deals with nanopatterning on a flat surface only. Here, however, nanopatterning is performed on a surface with pre-existing large surface features instead. Apparently the edges of the ridges are the cause of such a sharp transition. At 60^o incidence angle ripple formation was observed on the ridges. Ar^+ irradiation was able to create ripple with a larger periodicity, while

O_2^+ irradiation was able to create more ordered and well-defined ripples at a lower fluence. When the ion beam is incident at 60^o and oriented at an oblique angle relative to the edges of the gratings, the direction of ripples changed according to the beam orientation, with its wave vector remaining parallel to the beam orientation. The surface of the ridges also became slanted with its surface normal facing towards the ion beam. This indicates sputtering may be faster along the side of the ridges closer to the ion beam. The changes in topography were able to increase the surface area by only a few percent, much less than that achieved by GLAD (~4x). Despite the topographical changes, either the surface chemistry remained unchanged, as in the case of O_2^+ irradiation, or the oxidation state of TiO_2 was temporarily reduced, and then reverted back to the original state upon exposure to the atmosphere for a sufficient amount of time, as in the case of Ar^+ irradiation.

In addition, it was found that irradiation caused a blue-shift in optical resonant peak wavelength, probably due to a decrease in film thickness by sputtering. Nevertheless, the peaks remained sharp and intense enough to be distinguishable from the background signal in most cases, implying the sensor's ability to detect peak wavelength changes, and thus act as a label-free biosensor to detect changes in target molecule adsorption based on the peak wavelength changes, is not affected. It was further found that an additional resonant peak was present when irradiation was carried out at $\varphi = 30^o$. It might be related to the surface of the gratings being slanted towards one direction after irradiation. Further experiments in varying the beam orientation at a finer scale will be needed to examine the relationship between the topography and the appearance of extra resonant peaks. This result is surprising, and the reason for this phenomenon was unclear.

The study to relate the presence of nanostructures to sensitivity of the biosensor, i.e. to relate the increase in surface area due to nanostructures to the amount of proteins adsorbed onto the surface,

was inconclusive. Proteins of different sizes and different adsorption mechanisms were used, but there was no clear trends of the amount of proteins adsorbed on surfaces as functions of separation of nanostructures and increase in surface area due to these structures. Moreover, the trends shown from XPS and optical transmission results, two techniques to determine the amount of target proteins present on the surface, did not match with each other. These experiments need to be repeated in the future to average out the data and hopefully observe more insightful trends. More samples with different ripple periodicity and surface area will also be needed.

9.2 Future directions

Based on the results of changes in surface topography, chemistry, optical transmission property, and the amount of target proteins adsorbed onto the sensor surface, several directions for future work has been proposed. First, the thickness of film should be increased so that a broader range of irradiation parameters can be used. The goal is to prolong the duration of irradiation with more energetic ions to induce larger nanostructures. The increase in film thickness can be achieved by sputter deposition before, during and after irradiation. In particular, investigation into deposition of TiO_2 during irradiation may be the most interesting, because the interaction between the deposition and ion irradiation fluxes has the potential to not only ensure a good quality of the deposited film, but also a good quality of the interface between the original and newly deposited film. This co-deposition might even induce nanostructured films under certain conditions.

Second, it is worth investigating in the reason for the appearance of an extra resonant peak when irradiation was carried out with the ion beam orientation is at an oblique angle relative to the diffraction grating wave vector. The additional resonant peak might of use in other applications of

biosensors, for example fluorescent biosensors in which more than one excitation wavelength may be used to excite more than one type of fluorescent dyes to image different target analytes. Furthermore, it may also be useful in optical filters to filter more than one wavelength and possibly many other optical applications. Therefore, it will be interesting to conduct further irradiation experiments with an oblique beam orientation relative to the gratings and examine more closely not only the changes in surface topography, but also the material property of the film, such as the crystallinity and thickness.

Lastly, since the protein adhesion test was inconclusive in whether the induced nanostructures have an impact in the amount of target proteins adsorbed on the surface, it is important to repeat these experiments to obtain more statistically significant results and hopefully observe some insightful trends. Alternative detection techniques, such as the use of a different optical excitation source or other common techniques such as Bradford protein assay, may be needed to compliment the techniques used in this study. More samples with different ripple periodicity and surface area will also be needed.

REFERENCES

[1] S. Andreescu and O. A. Sadik, “Trends and challenges in biochemical sensors for clinical and environmental monitoring,” *Pure Appl. Chem.*, vol. 76 (4), pp. 861-878, 2004.

[2] A. F. Collings and F. Caruso, “Biosensors: recent advances,” *Rep. Prog. Phys.*, vol. 60, pp. 1397-1445, 1997.

[3] C.-S. Huang, S. George, M. Lu, V. Chaudhery, R. Tan, R.C. Zangar, and B.T. Cunningham, Anal. Chem. **83**, 1425 (2011).

[4] Brian Cunningham (2013), "[Illinois] ECE 416: Biosensors," https://nanohub.org/resources/16705.

[5] S. Johnson and T.F. Krauss, Expert Review of Medical Devices **14**, 177 (2017).

[6] X. Guo, J. Biophoton. **5**, 483 (2012).

[7] J.D. Joannopoulos, S.G. Johnson, J.N. Winn, and R.D. Meade, *Photonic Crystals: Molding the Flow of Light*, 2nd ed. (Princeton University Press, 2008).

[8] D. Rosenblatt, A. Sharon, and A.A. Friesem, IEEE Journal of Quantum Electronics **33**, 2038 (1997).

[9] V. Chaudhery, S. George, M. Lu, A. Pokhriyal, and B. T. Cunningham, Sensors **13**, 5561 (2013).

[10] A.K. Kodali, M. Schulmerich, J. Ip, G. Yen, B.T. Cunningham, and R. Bhargava, Anal. Chem. **82**, 5697 (2010).

[11] N. Ganesh, P.C. Mathias, W. Zhang, and B.T. Cunningham, Journal of Applied Physics **103**, 083104 (2008).

[12] N. Ganesh, I.D. Block, P.C. Mathias, W. Zhang, E. Chow, V. Malyarchuk, and B.T. Cunningham, Opt. Express, OE **16**, 21626 (2008).

[13] P.C. Mathias, S.I. Jones, H.-Y. Wu, F. Yang, N. Ganesh, D.O. Gonzalez, G. Bollero, L.O. Vodkin, and B.T. Cunningham, Anal. Chem. 82, 6854 (2010).

[14] P.C. Mathias, N. Ganesh, and B.T. Cunningham, Anal. Chem. 80, 9013 (2008).

[15] F. Frascella, S. Ricciardi, P. Rivolo, V. Moi, F. Giorgis, E. Descrovi, F. Michelotti, P. Munzert, N. Danz, L. Napione, M. Alvaro, and F. Bussolino, Sensors **13**, 2011 (2013).

[16] A.D. Smith, B.T. Cunningham, E. Chow, J. a. N.T. Soares, N. Ganesh, P.C. Mathias, V. Malyarchuk, and W. Zhang, Nature Nanotechnology **2**, 515 (2007).

[17] P. Alivisatos, Nat. Biotechnol. **22**, 47 (2004).

[18] S.M. Shamah and B.T. Cunningham, Analyst **136**, 1090 (2011).

[19] S. Kaja, J.D. Hilgenberg, J.L. Collins, A.A. Shah, D. Wawro, S. Zimmerman, R. Magnusson, and P. Koulen, J. Biomed. Opt. **17**, 081412 (2012).

[20] H. Shafiee, E.A. Lidstone, M. Jahangir, F. Inci, E. Hanhauser, T.J. Henrich, D.R. Kuritzkes, B.T. Cunningham, and U. Demirci, Scientific Reports **4**, 4116 (2014).

[21] D. Zecca, A. Qualtieri, G. Magno, M. Grande, V. Petruzzelli, B. Prieto-Simon, A. D'Orazio, M.D. Vittorio, N.H. Voelcker, and T. Stomeo, IEEE Photonics Journal **6**, 1 (2014).

[22] A. Fujishima and K. Honda, Nature **238**, 37 (1972).

[23] K. Hashimoto, H. Irie, and A. Fujishima, Jpn. J. Appl. Phys., Part 1 **44**, 8269 (2005).

[24] B. O'Regan and M. Gratzel, Nature **353**, 737 (1991).

[25] Z. Zhao, B. K. Tay, and G. Yu, Appl. Optics **43**, 1281 (2004).

[26] T. Alasaarela, T. Saastamoinen, J. Hiltunen, A. Säynätjoki, A. Tervonen, P. Stenberg, M. Kuittinen, and S. Honkanen, Appl. Opt., AO **49**, 4321 (2010).

[27] 1 S. Mondal, A. Kumar, K.S.R.K. Rao, and V. Venkataraman, AIP Conference Proceedings 1731, 080017 (2016).

[28] D. Tiwari, K. Mullaney, S. Korposh, S.W. James, S.-W. Lee, and R.P. Tatam, Sensors and Actuators B: Chemical **242**, 645 (2017).

[29] A.J. Haider, A.A. Najim, and M.A.H. Muhi, Optics Communications **370**, 263 (2016).

[30] D.M. Brunette, P. Tengvall, M. Textor, and P. Thomsen, *Titanium in Medicine*, 1st ed. (Springer-Verlag Berlin Heidelberg, 2001).

[31] L. K. Adams, D. Y. Lyon, and P. J. J. Alvarez, Water Res. **40,** 3527 (2006).

[32] H. A. Jeng and J. Swanson, J. Environ. Sci. Health, Part A: Toxic/Hazard. Subst. Environ. Eng. **41**, 2699 (2006).

[33] M. D. Newman, M. Stotland, and J. I. Ellis, J. Am. Acad. Dermatol. **61**, 685 (2009).

[34] L. Mikkelsen, M. Sheykhzade, K. Jensen, A. Saber, N. Jacobsen, U. Vogel, H. Wallin, S. Loft, and P. Moller, Part. Fibre Toxicol. **8**, 32 (2011).

[35] S.-J. Bao, C.M. Li, J.-F. Zang, X.-Q. Cui, Y. Qiao, and J. Guo, Adv. Funct. Mater. **18**, 591 (2008).

[36] K.-S. Mun, S.D. Alvarez, W.-Y. Choi, and M.J. Sailor, ACS Nano **4**, 2070 (2010).

[37] S. Liu and A. Chen, Langmuir **21**, 8409 (2005).

[38] T. Paunesku, T. Rajh, G. Wiederrecht, J. Maser, S. Vogt, N. Stojićević, M. Protić, B. Lai, J. Oryhon, M. Thurnauer, and G. Woloschak, Nat Mater **2**, 343 (2003).

[39] K. T. Thurn, T. Paunesku, A. Wu, E. M. B. Brown, B. Lai, S. Vogt, J. Maser, M. Aslam, V. Dravid, R. Bergan, and G. E. Woloschak, Small **5**, 1318 (2009).

[40] X. Zhang, F. Wang, B. Liu, E. Y. Kelly, M. R. Servos, and J. Liu, Langmuir **30**, 839 (2014).

[41] M. Nastasi, J. W. Mayer, and J. K. Hirvonen, *Ion-Solid Interacctions: Fundamentals and Applications,* 1st ed. (Cambridge University Press, GB, 1996), ISBN 0521 37376.

[42] L. A. Giannuzzi, B. I. Prenitzer, and B. W. Kempshall, in *Introduction to Focused Ion Beams*, edited by L. A. Giannuzzi and F. A. Stevie (Springer, NY, USA, 2005), Chap. 2, p. 13, ISBN 0-387-23116-1.

[43] P. Sigmund, Phys. Rev. **184**, 383 (1969).

[44] W. Moller (2003), Lecture on Fundamentals of Ion-Surface Interaction, Technical University of Dresden. https://www.hzdr.de/db/Cms?pOid=37977

[45] L. Bruchhaus, P. Mazarov, L. Bischoff, J. Gierak, A. D. Wieck, and H. Hövel, Appl. Phys. Rev. **4**, 011302 (2017).

[46] D. B. Graves, IEEE Transactions on Plasma Science **22,** 31 (1994).

[47] K. Vad, A. Csik, and G. Langer, Spectroscopy Europe **21**, 13 (2009).

[48] H. Oechsner, Int. J. Mass Spectrom. Ion Process. **143**, 271 (1995).

[49] Z.W. Kowalski, Vacuum **63**, 603 (2001).

[50] H. Zreiqat, S.M. Valenzuela, B.B. Nissan, R. Roest, C. Knabe, R.J. Radlanski, H. Renz, and P.J. Evans, Biomaterials 26, 7579 (2005).

[51] J. D. Halley, and D. A. Winkler, Complexity **14**, 10 (2008).

[52] P. Sigmund, J. Mater. Sci. **8**, 1545 (1973).

[53] R. M. Bradley and J. M. E. Harper, J. Vac. Sci. Technol. A **6,** 2390 (1988).

[54] C. S. Madi, E. Anzenberg, K. F. Ludwig Jr., and M. J. Aziz, Phys. Rev. Lett. **106**, 066101 (2011).

[55] G. Ozaydin, K. F. Ludwig Jr., H. Zhou, L. Zhou, and R. L. Headrick, J. Appl. Phys. **103**, 033512 (2008).

[56] G. Carter, V. Vishnyakov, Phys. Rev. B **54**, 17647 (1996).

[57] R. Cuerno and A. L. Barabási, Phys. Rev. Lett. **74**, 4746 (1995).

[58] S. Facsko, T. Bobek, A. Stahl, H. Kurz, and T. Dekorsy, Phys. Rev. B **69**, 153412 (2004).

[59] Makeev, M.A.; Cuerno, R.; Barab´asi, A.L. Nucl. Inst. Meth. Phys. Res. B 2002, 197, 185-227.

[60] Muñoz-García, J.; Castro, M.; Cuerno, R. Phys. Rev. Lett. 2006, 96, 086101.

[61] E. Chason, W. Chan, and M. Bharathi, Phys. Rev. B: Condens. Matter **74**, 224103 (2006).

[62] A. Hartmann, R. Kree, and T. Yasseri, J. Phys. Condens. Matter **21** 224015 (2009).

[63] Z. Yang, M. Lively, and J. P. Allain, Nucl. Instr. Meth. Phys. Res. B **307**, 189 (2013).

[64] A. Keller and S. Facsko, Materials **3**, 4811 (2010).

[65] S. A. Mollick and D. Ghose, J. Appl. Phys. **106,** 044309 (2009).

[66] B. Ziberi, F. Frost, T. Höche, and B. Rauschenbach, Vacuum **81**, 155 (2006).

[67] U. Valbusa, C. Boragno, and F. Buatier de Mongeot, J. Phys.: Condens. Matter **14**, (2002).

[68] R. Gago, L. Vázquez, O. Plantevin, J. A. Sánchez-García, M. Varela, M. C. Ballesteros, J. M. Albella, and T. H. Metzger, Phys. Rev. B **73**, 155414 (2006).

[69] J. Zhou, S. Facsko, M. Lu, and W. Möller, J. Appl. Phys. **109**, 104315 (2011).

[70] H. Hofsäss, K. Zhang, A. Pape, O. Bobes, and M. Brötzmann, Appl. Phys. A **111**, 653 (2013).

[71] D. Ghose, J. Phys.: Condens. Matter **21**, 224001 (2009).

[72] P. Karmakar, and D. Ghose, Surf. Sci. **554**. 101 (2004).

[73] I.P. Jain and G. Agarwal, Surface Science Reports **66**, 77 (2011).

[74] R.G. Elliman, S.T. Johnson, A.P. Pogany, and J.S. Williams, Nuclear Instruments and Methods in Physics Research Section B: Beam Interactions with Materials and Atoms **7**–**8**, 310 (1985).

[75] H.X. Qian, W. Zhou, Y.Q. Fu, B.K.A. Ngoi, and G.C. Lim, Applied Surface Science **240**, 140 (2005).

[76] Y. Ohtsuka, M. Matsuura, N. Chida, M. Yoshinari, T. Sumii, and T. Dérand, Surface and Coatings Technology **65**, 224 (1994).

[77] S. Kha, I. Ahmed, N. Khalid, M. Mehmood, A. Waheed, and M. Malik, Mater. Sci. Semiconductor Processing **39**, 530 (2015).

[78] P. Goudeau, M. George, and C. Coupeau, Appl. Phys. Lett. **84**, 894 (2004).

[79] M. A. Bodea, J. D. Pedarnig, K. Siraj, D. Bäuerle, W. Lang, C. Hasenfuss, L. Palmetshofer, K. Haselgrübler, R. Kolarova, and P. Bauer, J. Phys.: Conference Series **234**, 012005 (2010).

[80] M. Stepanova and S. K. Dew, J. Phys.: Condens. Matter **21**, 224014 (2009).

[81] O. El-Atwani, S. Ortoleva, A. Cimaroli, and J. P. Allain, Nanoscale Research Letters **6**, 403 (2011).

[82] Y. Kim, C. H. Yoon, K. J. Kim, and Y. Lee, J. Vac. Sci. Technol., A **25**, 1219 (2007).

[83] V. Solanki, S. Majumder, I. Mishra, P. Dash, C. Singh, D. Kanjilal, and S. Varma, J. Appl. Phys, **115**, 124306 (2014).

[84] X. D. Zheng, F. Ren, G. X. Cai, M. Q. Hong, H. H. Xiao, W. Wu, Y. C. Liu, W. Q. Li, J. J. Ying, and C. Z. Jiang, J. Appl. Phys. **115**, 184306 (2014).

[85] X. Zheng, S. Shen, F. Ren, G. Cai, Z. Xing, Y. Liu, D. Liu, G. Zhang, X. Xiao, W. Wu, and C. Jiang, Int. J. Hydrogen Energy **40**, 5034 (2015).

[86] S.-R. Kim and M.K. Parvez, Journal of Materials Research **26**, 1012 (2011).

[87] J.-Y. Zheng, S.-H. Bao, Y. Guo, and P. Jin, ACS Appl. Mater. Interfaces **6**, 1351 (2014).

[88] M. Takeuchi, Y. Onozaki, Y. Matsumura, H. Uchida, and T. Kuji, Nucl. Instr. Meth. Phys. Res. B **206**, 259 (2003).

[89] R. Wang, K. Hashimoto, A. Fujishima, M. Chikuni, E. Kojima, A. Kitamura, M. Shimohigoshi, and T. Watanabe, Nature **388**, 431 (1997).

[90] S. Hashimoto and A. Tanaka, Surf. Interface Anal. **34**, 262 (2002).

[91] I. Bertóti, R. Kelly, M. Mohai, and A. Tóth, Surf. Interface Anal. **19**, 291 (1992).

[92] M. Wolff, J. W. Schultze, and H.-H. Strehblow, Surf. Interface Anal. **17**, 726 (1991).

[93] S. Majumder, I. Mishra, U. Subudhi, and S. Varma, Appl. Phys. Lett. **103**, 063103 (2013).

[94] A. A. Vertegal, R. W. Siegel, and J. S. Dordick, Langmuir **20**, 6800 (2004).

[95] M. Lundqvist, I. Sethson, B.-H. Jonsson, Langmuir **20**, 10639 (2004).

[96] P. Roach, D. Farrar, and C. C. Perry, J. Am. Chem. Soc. **128**, 3939 (2006).

[97] M.B. Hovgaard, K. Rechendorff, J. Chevallier, M. Foss, and F. Besenbacher, Journal of Physical Chemistry B **112,** 8241 (2008).

[98] T.J. Webster, L.S. Schadler, R.W. Siegel, R. Bizios, Tissue Engineering **7**, 291 (2001).

[99] L. Luong-Van, I. Rodriguez, H. Y. Low, N. Elmouelhi, B. Lowenhaupt, S. Natarajan, C. T. Lim, R. Prajapati, M. Vyakarnam, and K. Cooper, J. Mater. Res. **28**, 165 (2013).

[100] W. Zhang, N. Ganesh, I. D. Block, and B. T. Cunningham, Sens. Actuators, B **131**, 279 (2008).

[101] P. E. Scopelliti, A. Borgonovo, M. Indrieri, L. Giorgetti, G. Bongiorno, R. Carbone, A. Podesta, and P. Milani, PLoS ONE **5**, 1 (2010).

[102] P. Thevenot, W. Hu, and L. Tang, Curr Top Med Chem **8**, 270 (2008).

[103] M.C.L. Martins, B.D. Ratner, and M.A. Barbosa, J. Biomed. Mater. Res. **67A**, 158 (2003).

[104] L. Liu and H. Elwing, J. Biomed. Mater. Res. **30**, 535 (1996).

[105] W.-J. Kim, S. Kim, B.S. Lee, A. Kim, C.S. Ah, C. Huh, G.Y. Sung, and W.S. Yun, Langmuir **25**, 11692 (2009).

[106] P. K. Chu, Thin Solid Films, **93,** 528 (2013).

[107] M.H. Fathi and A. Doostmohammadi, Journal of Materials Processing Technology **209**, 1385 (2009).

[108] X. Liu, P. K. Chu, and C. Ding. Mater. Sci. Eng. R-Rep. **70**, 275 (2010).

[109] K. S. Siow, L. Britcher, S. Kumar, and H. J. Griesser. Plasma Process. Polym. **3**, 392 (2006).

[110] B. T. Cunningham, B. Lin, J. Qiu, P. Li, J. Pepper, and B. Hugh, Sens. Actuators, B **85**, 219 (2002).

[111] P. West, and N. Starostina, Microscopy Today **11**, 20 (2003).

[112] R. Nyholm, N. Mårtensson, A. Lebugle, and U. Axelsson, J. Phys. F: Metal Phys. **11**, 1727 (1981).

[113] M. Zhang, J. Peh, P. J. Hergenrother, and B. T. Cunningham, J. Am. Chem. Soc., 136 (2014), 5840-5043.

[114] Z. Zhang, S. R. Park, A. Pertsinidis, and A. Revyakin, Bio-protocol **6**, 1-12 (2016).

[115] J. Pouilleau, D. Devilliers, H. Groult, and P. Marcus, J. Mater. Sci. **32**, 5645 (1997).

[116] P. Babelon, A. S. Dequiedt, H. Mostéfa-Sba, S. Bourgeois, P. Subillot, and M. Sacilotti, Thin Solid Films **322**, 63 (1998).

[117] I. Bertóti, R. Kelly, M. Mohai, and A. Tóth, Surf. Interface Anal. **19**, 291 (1992).

[118] A.O.T. Patrocínio, E.B. Paniago, R.M. Paniago, and N.Y.M. Iha, Applied Surface Science **254**, 1874 (2008).

[119] X.-G. Hou and A.-D. Liu, Radiation Physics and Chemistry **77**, 345 (2008).

[120] C.A. Mack, *Field Guide to Optical Lithography* (SPIE Press, 2006).

[121] B.D. Bunday, M. Bishop, D.W. McCormack, Jr., J.S. Villarrubia, A.E. Vladar, R. Dixson, T.V. Vorburger, N.G. Orji, and J.A. Allgair, in edited by R.M. Silver (Proc. SPIE 5375, Metrology, Inspection, and Process Control for Microlithography XVIII, 2004), p. 515.

[122] R. L. Kurtz, and V. E. Henrich, Surf. Sci. Spectra **5**, 179 (1998).

[123] R.-D. Sun, A. Nakajima, A. Fujishima, T. Watanabe, and K. Hashimoto, J. Phys. Chem. B **105**, 1984 (2001).